Paleoceanography and Paleoclimatology

RESEARCH ARTICLE
10.1029/2025PA005360

Antarctic Response to Orbital Forcing During the Intensification of Extensive Bipolar Glaciation (1.75–3.30 Ma) From Relative Paleomagnetic Intensity Stratigraphy of the Dove Basin, Scotia Sea

Brendan Reilly[1], Lisa Tauxe[2], Ian Bailey[3], Stefanie Brachfeld[4], Kelly Fenton-Samuels[1,5], Robert G. Hatfield[6], Sidney Hemming[1,5], Claire E. Jasper[1,5], Suzanne O'Connell[7], Maureen E. Raymo[1,5], Joseph Stoner[8], Jonathan Warnock[9], and Trevor Williams[10]

[1]Lamont-Doherty Earth Observatory, Columbia University, Palisades, NY, USA, [2]Scripps Institution of Oceanography, University of California San Diego, La Jolla, CA, USA, [3]Department of Earth and Environmental Sciences, Camborne School of Mines, University of Exeter, Cornwall, UK, [4]Department of Earth and Environmental Studies, Montclair State University, Upper Montclair, NJ, USA, [5]Department of Earth and Environmental Sciences, Columbia University, New York, NY, USA, [6]Department of Geological Sciences, University of Florida, Gainesville, FL, USA, [7]Department of Earth and Environmental Sciences, Wesleyan University, Middletown, CT, USA, [8]College of Earth, Ocean, and Atmospheric Sciences, Oregon State University, Corvallis, OR, USA, [9]Department of Geoscience, Indiana University of Pennsylvania, Indiana, PA, USA, [10]International Ocean Discovery Program, Texas &M University, College Station, TX, USA

Abstract The sediments of "Iceberg Alley," north of the Weddell Sea Embayment of Antarctica, are a key archive of Antarctic Ice Sheet and Southern Ocean history but are challenging to date at orbital timescales due to lack of foraminifera. We present a relative paleomagnetic intensity (RPI) chronology for sediments deposited across the Pliocene-Pleistocene Transition (3.14–1.75 Ma) at Dove Basin, International Ocean Discovery Program (IODP) Sites U1536 and U1537. Leveraging the well-defined magnetizations of these deep-sea contourite deposits, for the first time we correlate a Dove Basin RPI proxy to a North Atlantic RPI template that is intercalibrated with benthic $\delta^{18}O$ and lithologic signals that record the history of Northern Hemisphere glaciation intensification (iNHG) from ~2.7 Ma. Our new RPI chronology demonstrates a close relationship between sedimentation rates and physical lithology, with high accumulation occurring at times of high biogenic silica concentrations. This relationship is found at both long periods that reflect the amplitude modulation of orbital forcing and at glacial-interglacial timescales. Moreover, the chronology indicates a transition in the pacing of lithologic variability during iNHG from having greater precession-paced variations than benthic $\delta^{18}O$ prior to 2.8 Ma and obliquity-paced variations after 2.6 Ma that are nearly identical to benthic $\delta^{18}O$. A clear and persistent influence of precession, especially during extreme early Pleistocene interglacial intervals (high biogenic silica and high accumulation rates) nevertheless persisted during times of high variance in both precession and obliquity forcing—most notable during Marine Isotope Stages 87, 89, and 91.

Key Points:

- A 1.75–3.14 Ma highly resolved Dove Basin relative paleomagnetic intensity (RPI) chronology allows study of Milankovitch-scale signals
- Accumulation rates vary with lithology and long-period amplitude modulation of orbital variations
- A transition in the pacing of lithologic changes occurred ~2.6 Ma during southward expansion of N. Hemisphere marine terminating margins

Supporting Information:

Supporting Information may be found in the online version of this article.

Correspondence to:

B. Reilly,
breilly@ldeo.columbia.edu

Citation:

Reilly, B., Tauxe, L., Bailey, I., Brachfeld, S., Fenton-Samuels, K., Hatfield, R. G., et al. (2026). Antarctic response to orbital forcing during the intensification of extensive bipolar glaciation (1.75–3.30 Ma) from relative paleomagnetic intensity stratigraphy of the Dove Basin, Scotia Sea. *Paleoceanography and Paleoclimatology*, *41*, e2025PA005360. https://doi.org/10.1029/2025PA005360

Received 29 OCT 2025
Accepted 29 JAN 2026

Author Contributions:

Conceptualization: Brendan Reilly, Lisa Tauxe, Ian Bailey, Stefanie Brachfeld, Sidney Hemming, Suzanne O'Connell, Maureen E. Raymo, Trevor Williams
Data curation: Brendan Reilly
Formal analysis: Brendan Reilly
Funding acquisition: Brendan Reilly, Lisa Tauxe, Ian Bailey, Stefanie Brachfeld, Sidney Hemming, Suzanne O'Connell, Jonathan Warnock, Trevor Williams
Investigation: Brendan Reilly, Lisa Tauxe, Stefanie Brachfeld
Methodology: Brendan Reilly, Joseph Stoner
Project administration: Brendan Reilly, Trevor Williams
Resources: Lisa Tauxe, Joseph Stoner
Supervision: Lisa Tauxe
Writing – original draft: Brendan Reilly

1. Introduction

The late Pliocene and Pleistocene are characterized by several significant long-term changes in the amplitude and pacing of glacial-interglacial cycles defined by the stacked benthic $\delta^{18}O$ record (e.g., Lisiecki & Raymo, 2005), such as the initiation of expanded bipolar glaciation (Bailey et al., 2013; Jansen et al., 2000; Shackleton et al., 1984) and mid-Pleistocene Transition (Clark et al., 2006; Lisiecki & Raymo, 2007; Pisias & Moore, 1981). While our understanding of the drivers of these long-term changes is incomplete, it is clear from records of benthic $\delta^{18}O$ and sea level that they are accompanied and forced, either directly or through feedback mechanisms, by significant changes in polar ice sheets. Thus, stratigraphic records with orbital-scale or higher resolution chronologies that capture past cryosphere variability are essential to our understanding of Earth's climate evolution.

International Ocean Discovery Program (IODP) Expedition 382 drilled contourite deposits in the Scotia Sea at Sites U1536-U1537 (Dove Basin) and U1538 (Pirie Basin) (Figure 1), north of the Weddell Sea Embayment in a region sensitive to Antarctic Ice Sheet and Southern Ocean dynamics named "Iceberg Alley" (Anderson & Andrews, 1999; Weber et al., 2021a). Using an untuned geomagnetic reversal age model and physical property stacks at Sites U1536 and U1537, Reilly et al. (2021) documented that the lithostratigraphy of the Dove Basin,

Writing – review & editing:
Brendan Reilly, Lisa Tauxe, Ian Bailey, Stefanie Brachfeld, Kelly Fenton-Samuels, Robert G. Hatfield, Sidney Hemming, Claire E. Jasper, Suzanne O'Connell, Maureen E. Raymo, Joseph Stoner, Jonathan Warnock, Trevor Williams

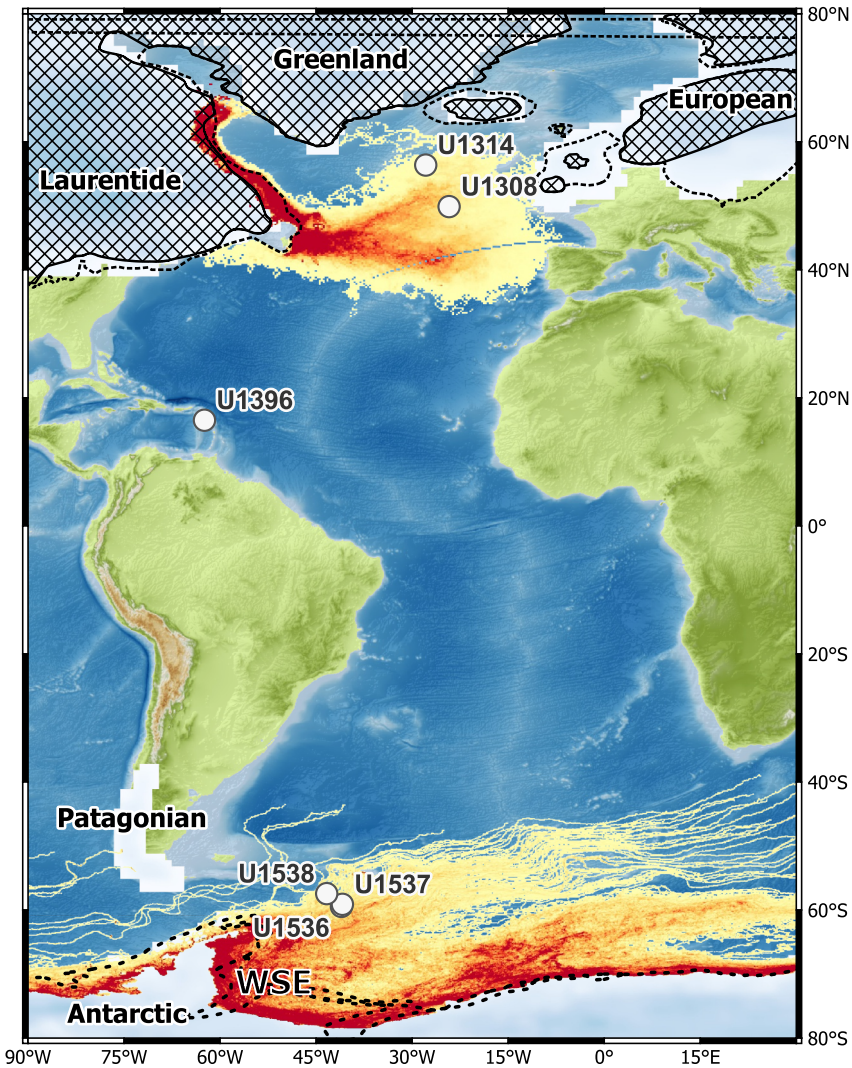

Figure 1. Map with location of sediment records used in this study. Major ice sheets of the Pleistocene are indicated with ICE7G (Roy & Peltier, 2017, 2018), with early Matuyama hypothesized ice-sheet extents indicated in the Northern Hemisphere (cross hatch = best estimate; dashed line = maximum estimate; Batchelor et al., 2019) and last glacial maximum reconstruction of the Antarctic Ice Sheet extent in the Southern Hemisphere (dashed lines; Bentley et al., 2014). Modeled iceberg pathways for Antarctica (Rackow et al., 2017) and medium sized icebergs from the Hudson Strait outlet of the Laurentide Ice Sheet (Fendrock et al., 2022) are included as heat maps with reds indicating relatively more icebergs and yellows indicating fewer icebergs. The base map is Global Multi-Resolution Topography (GMRT) v4.2 (Ryan et al., 2009). WSE, Weddell Sea Embayment.

Scotia Sea, display strong orbital variation in the relative proportion of biogenic to lithogenic sediments. Through comparison with Site U1538 from the Pirie Basin to the north, these lithologic variations have also been demonstrated to be well reproduced on a broader regional level (Bailey et al., 2022; Weber et al., 2021b). In the Pleistocene, long-period evolution in the amplitude modulation of these lithologic changes within frequency bands associated with the eccentricity and obliquity of Earth's orbit display a similar pattern to amplitude modulation of these frequency bands in benthic $\delta^{18}O$, a proxy for globally integrated ice volume and deep-sea temperature (Reilly et al., 2021). However, differences in the amplitude modulation within the frequency bands associated with precession (~1/23–1/19 kyr^{-1}) between Scotia Sea lithology and benthic $\delta^{18}O$ indicates that processes controlling sedimentation in the Scotia Sea may be sensitive to high latitude peak summer insolation during the so-called "41-kyr" world of the early Pleistocene. If the mechanism is related to changes in the volume of the Antarctic Ice Sheets, this observation would be consistent with the predictions of the "anti-phase

hypothesis" of Raymo et al. (2006) and have important implications for our understanding of ice sheet dynamics in the 41-kyr world.

The Reilly et al. (2021) study has at least two major limitations. First, Scotia Sea sediments are influenced by a variety of sediment transport processes and contain a convolved signal that encodes bottom current dynamics, Antarctic sediment discharge, and primary productivity (Diekmann et al., 2000; Hallmaier et al., 2025; Shin et al., 2020; Sprenk et al., 2013; Weber et al., 2014) with ice-rafted debris (IRD) fluxes likely providing clearer insight into Antarctic ice volume changes (Jasper et al., 2024). Second, magnetic reversals only occurred sporadically, on average every 250 kyr over the last 3.5 Ma with durations of stable polarity intervals ranging from 21 to 773 kyr (Channell et al., 2016; Gradstein et al., 2020). This limits the precision of the age model and prohibits precise constraints on the details of higher frequency precession and obliquity paced signals. In this study, we seek to provide new constraints to address the need for a highly resolved age model, developed independently from direct orbital turning, through Dove Basin's record of geomagnetic relative paleointensity (RPI) correlated to a benthic $\delta^{18}O$ age calibrated RPI template. A subsequent study will explore the implications for IRD fluxes and provenance.

RPI stratigraphy, a method of stratigraphic correlation that utilizes proxy reconstructions of geomagnetic field strength (Opdyke & Channell, 1996; Roberts et al., 2013; Tauxe, 1993; Tauxe & Yamazaki, 2007), provides the potential for global correlation between sedimentary archives independent of the tuning of climate sensitive proxies (Channell et al., 2009; Stoner et al., 2002; Ziegler et al., 2011). Around Antarctica, where rare or discontinuous biogenic calcite limits the ability to use radiocarbon and benthic $\delta^{18}O$ for age constraints, RPI has been an important tool for assessing and/or constraining chronologies on Holocene (Brachfeld et al., 2003; Smith et al., 2021; Truax et al., 2025; Willmott et al., 2006) and Pleistocene (Channell et al., 2019; Guyodo et al., 2001; Hopkins et al., 2024) timescales. Globally, deep sea contourites with accumulation rates of ~5–20 cm/kyr and limited diagenetic alteration have proved to be some of the best archives of resolving long time series of orbital to sub-orbital timescale RPI variations (e.g., Channell et al., 2002; Guyodo et al., 2001; Xuan et al., 2016). Here we explore the RPI record, geomagnetic instabilities, and chronology of a similar setting deep sea contourite deposit from the Scotia Sea's Dove Basin. These new orbital resolution age constraints have allowed us to study the climate signals recorded in Dove Basin lithology without making any lithologic orbital tuning assumptions.

2. Materials and Methods

Site U1537 (59°6.65′S, 40°54.37′W, 3713 m water depth) was drilled from a deep-sea contourite deposit in the Scotia Sea's Dove Basin during IODP Expedition 382, "Iceberg Alley and Subantarctic Ice and Ocean Dynamics" (for previous work and additional details of this site see Jasper et al., 2024; Pérez et al., 2021; Reilly et al., 2021, 2024; Warnock et al., 2022; Weber et al., 2021c, 2021a, 2022) (Figure 1). Advanced piston cored sediments at Site U1537 extend to below the Gilbert-Gauss (C2Ar–C2An.3n; 3.596 Ma) boundary with slumped intervals becoming common below the base of the Mammoth Subchron (C2An.2r; 3.330 Ma) (Reilly et al., 2021; Weber et al., 2021c). With nearby Dove Basin Site U1536 (Figure 1), these IODP Expedition 382 Dove Basin sites represent one of the highest resolution and most continuous late Pliocene and Pleistocene records ever recovered near Antarctica (Reilly et al., 2021; Weber et al., 2021a). Dove Basin sediments are demonstrated to be sensitive to centennial, millennial, orbital, and longer term Antarctic Ice Sheet variability and Southern Ocean Dynamics, receiving sediments focused by bottom currents and transported as IRD (Jasper et al., 2024; Pérez et al., 2021; Reilly et al., 2021; Sprenk et al., 2013; Weber et al., 2012, 2014, 2022). Dove Basin lithostratigraphy primarily reflects changes in the relative proportion of diatom ooze and terrigenous silty clays, which can be traced using routine non-destructive measurements like gamma ray attenuation (GRA) density, natural gamma radiation (NGR), and the blue-yellow sediment color parameter b* (Reilly et al., 2021; Sprenk et al., 2013; Weber et al., 2022). In the late Quaternary, magnetic susceptibility (κ) is not correlated with the concentration of IRD (Weber et al., 2012) and variations in κ are likely driven by changes in the silt or finer fractions. For the last 800 kyr, Scotia Sea κ variations are noted to closely align with variations in Antarctic ice core dust concentrations, with independent chronometers indicating similarity in the signals over the last glacial cycle and at the 0.773 Ma Matuyama-Brunhes (C1r.1r–C1n) boundary (Pugh et al., 2009; Weber et al., 2012, 2022; Xiao et al., 2016). It has been proposed that these κ variations follow variations in global ice volume and sea level, tracked by benthic $\delta^{18}O$, back to at least 1.5 Ma (Weber et al., 2022).

Fifty-three u-channel samples, 2 cm × 2 cm × up to 150 cm plastic tubes with clip-on lids (e.g., Mead et al., 1986; Weeks et al., 1993) were collected from the center of selected core sections to create a near-continuous record using sections from the working halves of Hole U1537D Cores 24H to 31F and sections from archive halves of Hole U1537A Cores 24H-27F. The u-channel sampled interval spans ∼1.7–2.8 Ma (Reilly et al., 2021; Weber et al., 2021c). This interval was chosen to address questions about the early Pleistocene where appropriate targets for climate correlation are less clear than they are for the later Pleistocene (c.f., Weber et al., 2022), and because shipboard paleomagnetic data indicated promise for RPI reconstruction for having well-defined magnetizations and strong natural remanent magnetization (NRM) intensities. The deepest depths sampled were chosen in consultation with the IODP Expedition 382 sample allocation committee to limit u-channel sampling to where there was parallel recovery in two holes (Hole U1537A and U1537D). We prioritized sampling working half sections from Hole U1537D that had not been previously sampled whenever possible and so u-channel data are not always from the equivalent sections used to create the U1537 composite record of Reilly et al. (2021). However, these u-channel were mapped onto that depth scale through correlation of physical properties (Figure S1 in Supporting Information S1; Table S3 in Reilly et al., 2025b). The composite depth scales for this interval follow those used by Reilly et al. (2021) and Jasper et al. (2024) and are identical to those presented in the expedition proceedings for the spliced interval (Weber et al., 2021c, 2021d) with additional offsets to cores recovered below the spliced interval to account for core expansion.

U-channel data were supplemented by shipboard physical properties and paleomagnetic data from Sites U1536 and U1537 previously reported in the Expedition 382 proceedings (Weber et al., 2021c, 2021d, 2021e) and further discussed in other recent studies (Pérez et al., 2021; Reilly et al., 2021, 2024; Weber et al., 2022). Stacking procedures for the composite κ and κ normalized NRM after 15 mT peak alternating field (AF) demagnetization for Sites U1536 and U1537 record follow the methods, depth scale, and correlation of the previously published Dove Basin physical property stacks of Reilly et al. (2021).

2.1. Sediment Magnetism

Progressive demagnetization of the NRM of the u-channel samples was measured at the Oregon State University (OSU) Paleo and Environmental Magnetism Laboratory on a 2G Enterprises™ model 755–1.65UC superconducting rock magnetometer (SRM) with inline AF coils optimized for u-channel samples. Because sediments from archive half sections were previously demagnetized to 15 mT peak AF while at sea (Weber et al., 2021c, 2021e), measurements of the remanent magnetization were made before and after peak AF demagnetization from 15 to 55 mT in 5 mT increments and 60–100 mT in 20 mT increments. Following 100 mT peak AF demagnetization of the NRM, anhysteretic remanent magnetizations (ARM) were applied using a 50 μT bias field and the same peak AF steps used to demagnetize the NRM. Finally, the strongest ARM acquired at 100 mT peak AF was progressively demagnetized using the same peak AF steps used to demagnetize the NRM. Flux jumps were monitored for and corrected using UPmag MATLAB tools (Xuan & Channell, 2009; Xuan & Oda, 2015). All measurements were made at 1 cm increments with a 10 cm leader and trailer; however, the effective resolution is the integrated remanent magnetization within the 7.6 cm full width at half maximum (FWHM) response function of the magnetometer (see Oda & Xuan, 2014 for a detailed description of the OSU system).

U-channel κ was measured every 1 cm on a motion-controlled u-channel track built at OSU with a Bartington MS3 meter attached to a MS2C loop sensor with an internal diameter of 36 mm. Reported values are the mean of three repeat measurements. Following a string break on 14 July 2020, and subsequent replacement, the positioning system on the OSU κ track had to be recalibrated for position errors and offsets between κ and SRM data. Investigating this issue using point magnetizations at known positions identified that a 1.0158 correction factor applied to the κ position data collected after 14 July 2020 allowed for accurate depth comparison. These adjusted position offsets are the positions reported here. This issue has been subsequently corrected.

Five subsamples were taken for detailed rock magnetic investigations on the Quantum Design Magnetic Properties Measurements System 3 (MPMS3) and Lakeshore Model 8600 Vibrating Sample Magnetometer (VSM) at the Institute for Rock Magnetism, University of Minnesota. The MPMS3 was used to measure Field Cooled (FC) and Zero Field Cooled (ZFC) Saturation Isothermal Remanent Magnetization (SIRM) imparted in a 2.5 T field at 10 K and monitored during warming to 300 K, and Low Temperature Cycling of Room Temperature SIRM (LTC-RTSIRM) curves using a 2.5 T field and minimum temperatures of 10 K (see Bilardello & Jackson, 2013). From these curves, we calculate the change in remanence across the Verwey Transition ($\delta T_v = (LTSIRM_{80K} - LTSIRM_{150K})/LTSIRM_{80K}$;

where LTSIRM is the FC or ZFC low temperature SIRM; Moskowitz et al., 1993), the remanence loss above the Verwey Transition (δM = (LTSIRM150K − LTSIRM300K)/LTSIRM150K; Hatfield et al., 2017) and the change in RTSIRM after cooling and warming (δRTSIRM). The VSM was used to measure hysteresis loops, direct current demagnetization (DCD) curves, and first order reversal curves (FORCs). Standard hysteresis parameters including remanent magnetization (M_r), saturation magnetization (M_s), and bulk coercivity (H_c) were calculated from the hysteresis loop after paramagnetic correction using an approach to saturation correction (Jackson & Solheid, 2010). The DCD curves were used to calculate the coercivity of remanence (H_{cr}) and S ratio ($IRM_{-300mT}/IRM_{1000mT}$; Stober & Thompson, 1979). FORC diagrams (Pike et al., 1999; Roberts et al., 2000), determined from 136 FORCs with 500 mT saturating field, 150 mT max H_c field, and −50 to 70 mT H_u fields, were processed using FORCinel v. 3.06 (Harrison et al., 2018; Harrison & Feinberg, 2008) and VARIFORC smoothing (Egli, 2013).

2.2. Computed Tomography (CT)

Computed Tomography (CT) scans were made on the u-channel samples using the OSU College of Veterinary Medicine Toshiba Aquillon 64 Slice Medical CT Scanner in collaboration with the OSU Marine and Geology Repository. U-channels were scanned in batches of eight in a custom-built wooden box and converted to 2 mm thick slices with an effective in-plane resolution of ~0.5 mm following the methods of Reilly et al. (2017). SedCT MATLAB tools (Reilly et al., 2017) were used to generate CT images and extract CT# values in quantitative Hounsfield Units (HU). HU values are the X-ray attenuation coefficient of the material relative to the X-ray attenuation coefficient of water and are a reflection of the materials density and atomic number (Hounsfield, 1973). For clayey sediments, the density of the sediments, in g/cm^3, can be approximated by CT#/1250 + 1 (Reilly et al., 2017). All CT data are presented in Figures S2–S13 of Supporting Information S1 with raw DICOM data available in the Zenodo database (Reilly, 2024).

2.3. X-Ray Fluorescence (XRF)

X-Ray Fluorescence (XRF) measurements were made on the split archive half surface using an Avaatech XRF Core Scanner (see Richter et al., 2006) at the Texas A&M Gulf Coast Repository, following their standard practices and as previously described for the 0–1.5 Ma interval (Weber et al., 2022). Measurement increments were generally around 2 cm, with measurement locations moved as needed to avoid cracks or surface imperfections and, in some cases, at higher resolution in sections of interest. Core sections were first scanned using a source energy of 10 kV (no filter) and then 30 kV (Pd filter) at 6 s count time to collect data for a wide range of elements. For the core sections of interest to this study, a third scan was performed at 50 kV (Cu filter) at 12 s count time to target Ba. While all data are available in the IODP-LIMS data repository and will be the focus of future studies, In this study, we only focus on the Ti/K and Si/Al ratios and remove values with Ar counts greater than zero.

2.4. Construction of a 1.65–2.80 Ma RPI Template

Our study's objectives require an RPI template that spans the latest Pliocene to early Pleistocene and is directly intercalibrated with the widely used LR04 benthic $\delta^{18}O$ timescale (Lisiecki & Raymo, 2005) and other climate signals of interest. Any one RPI record may be complicated by a variety of local factors, including coring and lithologic artifacts (Brachfeld & Banerjee, 2000; Mazaud, 2006; Schwartz et al., 1996; Tauxe, 1993) and thus are strengthened by demonstrating reproducible signals on regional and global scales. The PISO-1500 (Channell et al., 2009) and HINAPIS-1500 (Xuan et al., 2016) stacks serve as templates with intercalibrated RPI and benthic $\delta^{18}O$ signals for the last 1.5 Myr and the NARPI-2200 stack (Channell et al., 2016) can be used to extend the template back to 2.2 Ma. All these templates are entirely composed of, or strongly biased to, paleomagnetic records from the North Atlantic. Additional Pleistocene stacks include the global SINT-2000 (Valet et al., 2005), global PADM2M (Ziegler et al., 2011) and western Equatorial Pacific EPAPIS-3 Ma (Yamazaki & Oda, 2005); however, these stacks have limited or no direct calibration with the benthic $\delta^{18}O$ signal in our study interval. While important for understanding geomagnetic change on these timescales, they cannot therefore be used to address the objectives of this study. This intercalibration is critical for RPI studies in this time interval, as, for example, the age of the base of the Olduvai Subchron (C2n) varies by the length of an obliquity cycle between timescales from 1.950 Ma (Shackleton et al., 1990, 1995), 1.942 Ma (Lourens et al., 1996), 1.945 Ma (Gradstein et al., 2012; Horng et al., 2002), 1.968 Ma (Lisiecki & Raymo, 2005), and 1.925 Ma (Channell et al., 2016, 2020) depending on how each timescale was developed (see Channell et al., 2020, 2016 for discussion). The confusion

10.1029/2025PA005360

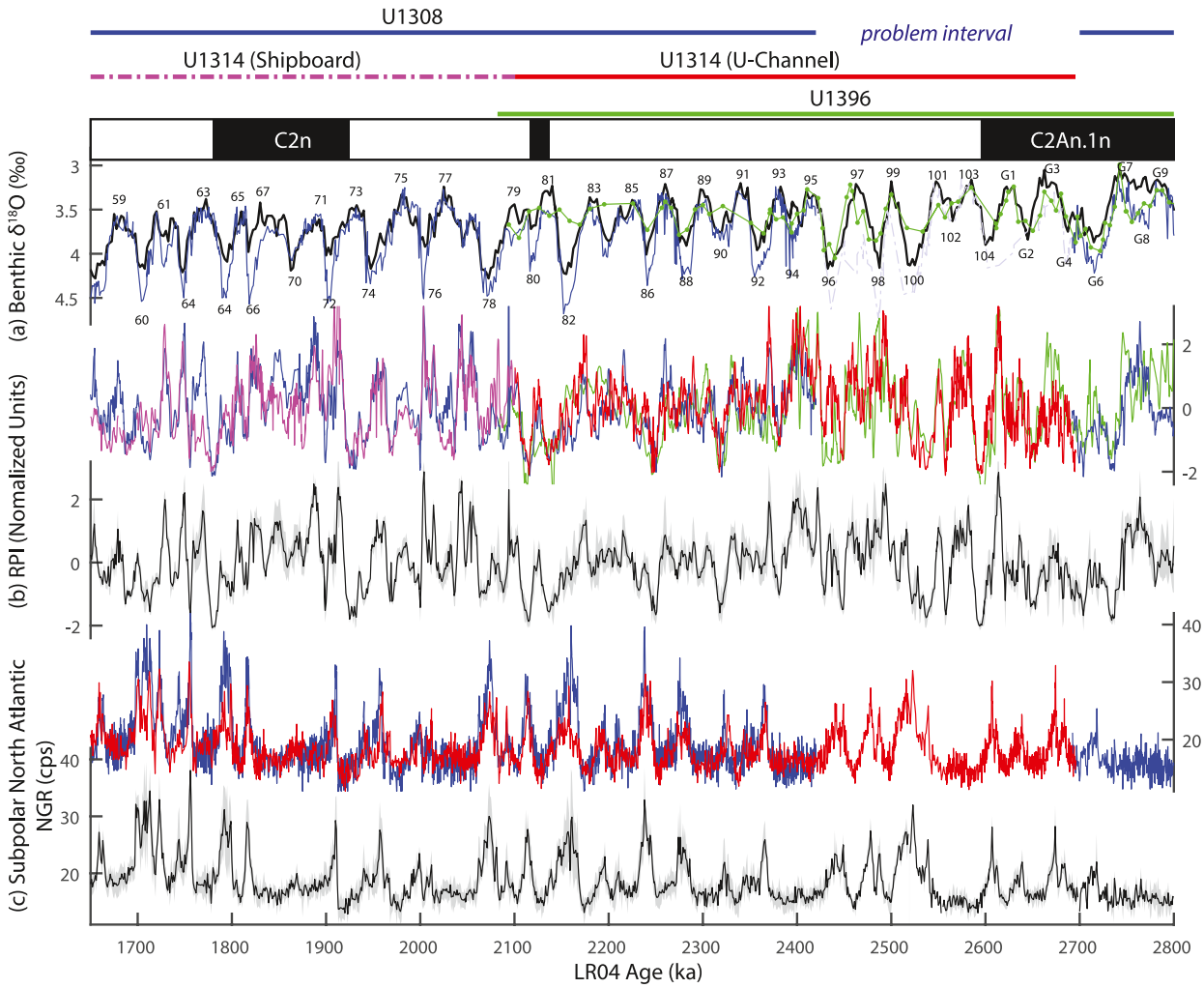

Figure 2. 1.65–2.8 Ma RPI Template using data from IODP Sites U1308 (blue; Channell et al., 2016, 2006; Hodell & Channell, 2016), U1314 (red/purple; Channell et al., 2006; Ohno et al., 2012), and U1396 (Fraass et al., 2017; Hatfield et al., 2021). (a) Comparison of the Site U1308 and U1396 benthic $\delta^{18}O$ records with the LR04 benthic $\delta^{18}O$ stack (black; Lisiecki & Raymo, 2005). (b) Comparison of Sites U1308, U1314, and U1396 normalized RPI records and resulting RPI template (black = median, shading = ±1σ). (c) Comparison of Sites U1308 and U1314 NGR and stacked signal (black = median, shading = ±1σ).

in the determination of the age of this subchron is common and has even resulted in different ages reported in different tables of the recent 2020 Geologic Timescale (i.e., 1.925 in their Table 5.2 and Figure 30.1 vs. 1.934 Ma in their Table 5.3 and Table 29.7; Gradstein et al., 2020).

Several RPI records exist that span the last ∼3 Ma, but IODP Site U1308 (a reoccupation of Deep Sea Drilling Project Site 609) is exceptional for having a mostly continuous and high-resolution co-registered record of terrigenous input to the subpolar North Atlantic, benthic $\delta^{18}O$, and RPI (Channell et al., 2008, 2016; Hodell & Channell, 2016; Hodell et al., 2008). However, the U1308 record is complicated by low sedimentation rates and hiatuses around the Pliocene-Pleistocene transition, notably between ∼2.60–2.65 Ma during Marine Isotope Stage (MIS) G2–104 with additional complications in the ∼2.45–2.55 Ma interval during MIS 97–100 (Bailey et al., 2010; Channell et al., 2016; Hodell & Channell, 2016). A previous paleoclimate study that wished to leverage the long and high resolution Site U1308 benthic $\delta^{18}O$ decided to patch in data from North Atlantic Site U1313 between 2.42 and 3.00 Ma (Liautaud et al., 2020) and previous paleomagnetic work has noted that the paleomagnetic signal at Site U1308 is complicated in this interval (Blake-Mizen et al., 2019; Channell et al., 2016; Hatfield et al., 2021). Thus, we use Site U1308 on its published age model (Channell et al., 2016) as the anchor record for constructing our 1.65–2.80 Ma template but remove the 2.42–2.69 Ma interval due to these lithologic complications (Figure 2).

To bridge the Site U1308 problem interval, we include IODP Site U1396 from the Caribbean Sea which has a well-defined RPI signal between 0–0.6 Ma and 2.1–4.5 Ma (Hatfield et al., 2021) and co-registered, albeit low resolution in comparison to Site U1308, benthic $\delta^{18}O$ (Fraass et al., 2017). This record is included in the 2.1–2.8 Ma interval and uses its published age model, which is based on a combination of benthic $\delta^{18}O$ and RPI (Hatfield et al., 2021). As far as we are aware, Site U1396 has the only moderate resolution and co-registered benthic $\delta^{18}O$ and RPI reconstructions available for the Pliocene-Pleistocene transition and future work would benefit greatly from targeted efforts on higher resolution archives across this time interval.

One of the highest quality and highest resolution paleomagnetic records documented between 2.10 and 2.75 Ma is North Atlantic Site U1314 from the Gardar Drift (Ohno et al., 2012). In younger time intervals, paleomagnetic records of the Gardar Drift have proven to be remarkable and immensely valuable for contributing to our understanding to long-term geomagnetic change (Channell, 1999; Channell et al., 1997, 2002; Channell & Kleiven, 2000; Xuan et al., 2016). However, a benthic $\delta^{18}O$ chronology is not available for the 1.65–2.80 interval recovered at Site U1314 and previously published chronologies have relied on assuming synchronous changes in sediment lithology and benthic $\delta^{18}O$ (Hayashi et al., 2010; Sato et al., 2015), an assumption we wish to avoid in this study. Instead, we correlate the natural gamma radiation (NGR) at Site U1314 to NGR variations at Site U1308 between 1.65 and 2.42 Ma, which is interpreted to reflect terrigenous input to the subpolar North Atlantic (Channell et al., 2006; Hodell & Channell, 2016). Likewise, to avoid assumptions of the correlation of U1314 lithology to benthic $\delta^{18}O$ prior to 2.41 Ma, we correlate the Site U1314 u-channel RPI reconstruction of Ohno et al. (2012) to Site U1396 between 2.42 and 2.75 Ma, which has previously been demonstrated to be consistent on independent age models (Hatfield et al., 2021). To extend the Site U1314 u-channel RPI reconstruction to include the 1.65–2.10 interval, we normalize the NRM following 20 mT peak AF demagnetization by the κ measured during IODP Expedition 306 (Channell et al., 2006), as we note excellent agreement between this method and the u-channel results where they overlap (Figure 2b).

Using IODP Sites U1308, U1314, and U1396, we constructed a 1.65–2.80 Ma stacked RPI template that is intercalibrated with both benthic $\delta^{18}O$ and a stacked record of terrigenous input to the subpolar North Atlantic (tracked by NGR; Figure 2). The final stacks were developed by binning and averaging data at 1 kyr intervals. Overlap of these three records demonstrates the reproducibility of RPI at sub-orbital timescales in the Atlantic sector through the 1.65–2.80 Ma time interval. While there are other records that span this interval from the Ontong Java Plateau (Kok & Tauxe, 1999), eastern equatorial Pacific (Valet & Meynadier, 1993; Yamazaki & Yamamoto, 2018), and western equatorial Pacific (Horng et al., 2003; Sakuramoto et al., 2017; Yamazaki & Oda, 2005), we do not include them in our template reconstruction due to their lower resolution and/or lack of direct correlation to benthic $\delta^{18}O$ or subpolar North Atlantic NGR. However, there are often broadly similar patterns with differences that could be attributed to differences in chronology and accumulation rate (e.g., Figure S15 in Supporting Information S1).

3. Results

3.1. Sediment Magnetism

For these U1537 u-channel samples, median NRM intensities after 15 mT AF demagnetization are 1.0×10^{-2} A/m, with a ± 1 sigma range of 0.3–2.5 $\times 10^{-2}$ A/m (Figures 3f and 4a). Progressive AF demagnetization of the Site U1537 u-channels generally indicate a well-defined Characteristic Remanent Magnetization (ChRM). Samples from U1537D, that had not been previously AF demagnetized during Expedition 382, have median destructive fields (MDF) with a ± 1 sigma range of 25–33 mT, although these estimates also reflect the influence of a low coercivity drill string overprint that is typically removed by 5 or 10 mT peak AF (Reilly et al., 2021; Richter et al., 2007; Weber et al., 2021c). Typically, the greatest rates of demagnetization occur between 15 and 35 mT peak AF, with median rates of ~2% of the initial NRM demagnetized per mT in this range. Targeting this interval, ChRMs were calculated using an unanchored PCA over six steps in the 15–40 mT range (Kirschvink, 1980) (Figures 3j and 3k). 95% of the maximum angular deviation (MAD) values, a measure of how well the magnetic vector is defined, are <5.7° and 68% of MAD values are less than 1.7°. Higher MAD values are generally associated with lower NRM intensities and transitional directions (Figures 3k and 4a).

Modern inclination, influenced by the South Atlantic Anomaly (SAA), at Site U1537 is −56° (Thébault et al., 2015), considerably shallower than the ± 73° inclination predicted by the geocentric axial dipole (GAD) hypothesis (Hospers, 1954). Site U1537 15–40 mT ChRM inclinations and inclinations after 15 mT peak AF (as

10.1029/2025PA005360

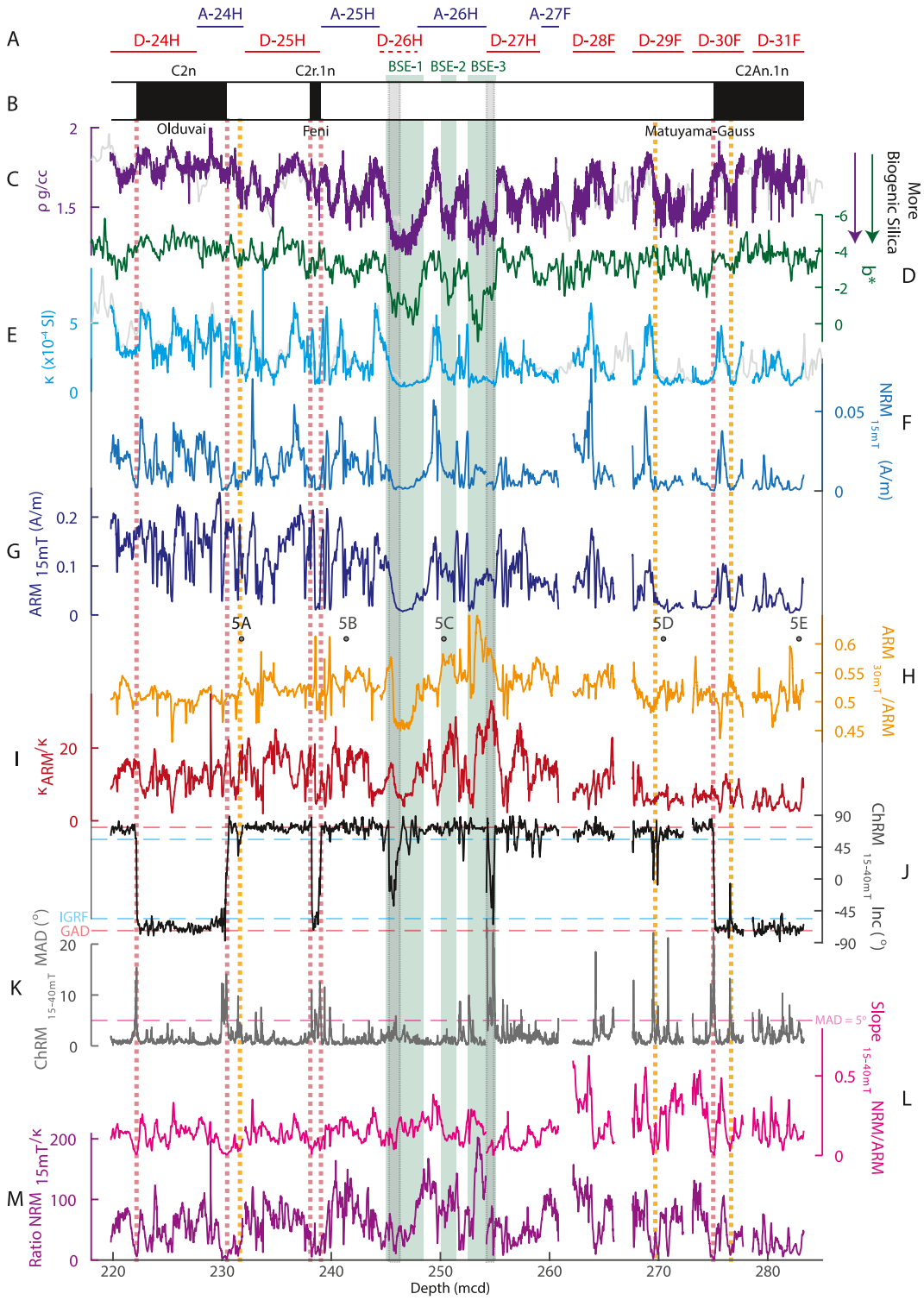

Figure 3.

discussed by Reilly et al. (2021); Weber et al. (2021c)) have nearly identical distributions with symmetric GAD-like histogram peaks at ±~71° (Figure 4b). This indicates that, on these timescales and the resolution our record resolves, SAA-like features are not a persistent feature of the geomagnetic field and long-term behavior is consistent with the GAD hypothesis. Thick intervals of anomalous inclinations containing intermediate directions, inconsistent with normal or reverse GAD predictions are found at depths of 245.28–246.26, in U1537D-26H-5W–6W, and 254.22–254.96 mcd, in U1537D-27H-3W (Figure 3j). These two intervals are also anomalous for having the highest b* (blue-yellow) color parameter values of the study interval and low density (Figures 3c and 3d), indicating a lithology with high concentrations of biogenic silica as demonstrated through direct comparison of b* and biogenic silica over the last 1.5 Ma (Sprenk et al., 2013; Weber et al., 2022). We identify three intervals of anomalously high b* values, low density, and low κ during the earliest Matuyama Chron C2r.2r, which we will refer to as Biogenic Silica Events (BSE) 1, 2, and 3 (Figure 3).

Declination values indicate that some cores experienced twisting and the u-channel declination values, while well-defined and in good agreement with shipboard data, should be treated with caution (Figures S16a and S16b in Supporting Information S1). Following the removal of linear trends, declination values can be rotated to means of 0 and 180° for each APC/HLAPC core based on the polarity interpreted from the inclination data, allowing for an imperfect estimate of virtual geomagnetic pole (VGP) latitudes dependent on these corrections and assumptions (Figures S16c and S16d in Supporting Information S1).

κ, NRM intensity, and ARM intensity display cyclicity in magnetic mineral concentration that generally correspond with increased magnetic mineral concentration in the silty clay lithofacies (higher density/lower b*) and lower concentrations in the biogenic ooze lithofacies (lower density/high b*) (Figures 3d–3h). However, the relationship between magnetic mineral concentration and lithofacies is not a simple 1:1 relationship, suggesting additional controls on magnetic mineral concentration beyond dilution by biogenic sediments, such as terrigenous sediment particle-size and/or provenance (e.g., Hatfield et al., 2017, 2019). While magnetic mineral concentration does not correlate with IRD concentrations in the late Quaternary, magnetic mineral assemblages have been shown to change along with terrigenous sediment composition in the Scotia Sea (Diekmann et al., 2000; Pugh et al., 2009; Shin et al., 2020; Weber et al., 2014).

Detailed rock magnetic analyses of five subsamples (positions indicated in Figure 3h) display properties consistent with a detrital magnetic mineral assemblage dominated by "pseudo-single domain" (or vortex state) (titano)magnetite with minor contributions from high coercivity minerals like hematite, similar to previously reported data for Site U1537 for 0–1.3 Ma (Reilly et al., 2024). This includes: (a) well defined Verwey Transitions in low temperature data, indicative of a significant non-oxidized stoichiometric magnetite component in the assemblage (Özdemir et al., 1993); (b) S-ratios that range from 0.87 to 0.97, illustrating variable contributions of high coercivity minerals like hematite with minor contribution to the overall remanence properties of the magnetic mineral assemblage (Frank & Nowaczyk, 2008; Stober & Thompson, 1979); (c) H_{cr} values that range from 37 to 45 mT and M_r/M_s ratios that range from 0.14 to 0.18, indicating pseudo-single domain (or vortex state) behavior of the bulk magnetic mineral assemblage (Day et al., 1977; Roberts et al., 2018) like values often observed for northern Antarctic Peninsula source rocks and regional detrital magnetic mineral assemblages (Reilly et al., 2016; Reilly, McCormick, et al., 2020; Shin et al., 2020; Xiao et al., 2016) (Figure 5). Consistent with these observations, FORC diagrams indicate abundant particles with vortex states (Lascu et al., 2018), but also indicate additional contribution from particles with single domain properties including a negative region close to the negative H_u axis and a central ridge structure that extends along the H_c axis (Egli et al., 2010) (Figure 5). The coercivity distributions along the H_c axis at $H_u = 0$ peak at $H_c = 0$ mT for the two samples with

Figure 3. Summary of u-channel results in the context of U1537 lithostratigraphy. (a) Intervals from Holes U1537A and U1537D used in this study (Figure S1 in Supporting Information S1). (b) Interpreted polarity (black = normal; white = reverse). (c, d) Dove Basin density (gray; (c)) and b* (green) stacks (Reilly et al., 2021), compared with CT derived density from the u-channel samples (purple; (d)). (e) U-channel κ (light blue) compared with a Dove Basin stack (gray). (f–g) U-channel NRM (blue; (f) and ARM (dark blue; g) intensity after 15 mT peak AF demagnetization. Black circles annotated as 5A-5E refer to the location of detailed rock magnetic measurements presented in Figure 5. (h, i) Magnetic "grain-size" parameters ARM_{30mT}/ARM (orange; (h) and κ_{ARM}/κ (red; (i). (j, k) ChRM Inclination (black; (j) and MAD values (gray; (k) calculated over the 15–40 mT peak AF range. (l, m) RPI proxies calculated as the slope of the NRM and ARM intensities between 15 and 40 mT peak AF (pink; l) and the ratio of NRM after 15 mT peak AF to κ (purple; m). Vertical red dashed lines indicate magnetic reversals and vertical orange dashed lines indicate likely magnetic excursions. Vertical gray shading indicates thick intervals where the inclinations are not consistent with stable normal or reverse polarity. Vertical green shading indicates biogenic silica events (BSE) 1–3 that occurred during the earliest Matuyama Chron C2r.2r and are recognized by anomalously high b* values.

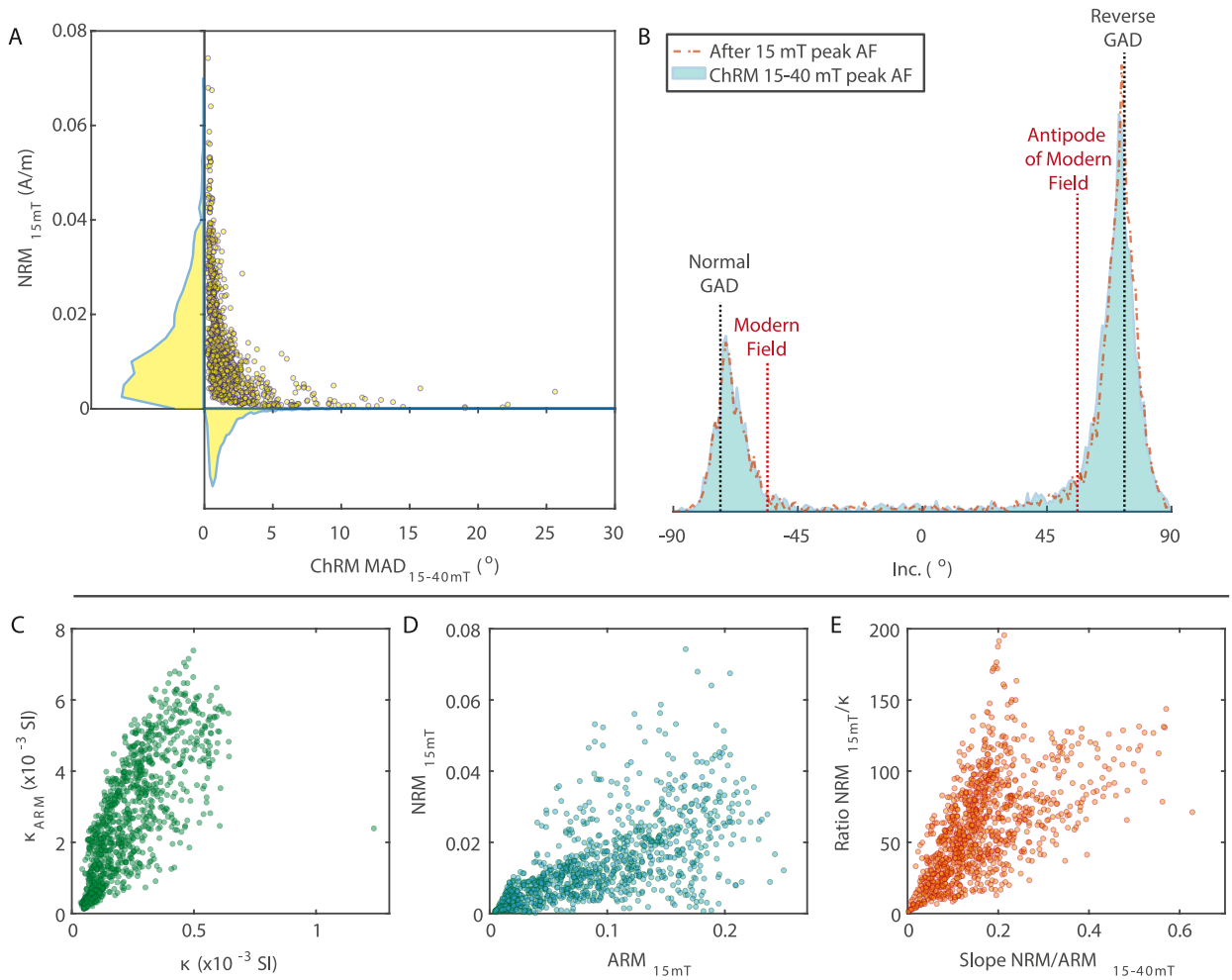

Figure 4. (a) Comparison of NRM intensity after 15 mT peak AF demagnetization and ChRM MAD values isolated using a PCA between 15 and 40 mT peak AF. Dots are individual measurements, while shaded areas represents the total distribution of values. (b) Histogram of inclination values after 15 mT peak AF demagnetization and ChRM inclinations isolated using a PCA between 15 and 40 mT peak AF. The modes of these distributions (±71°) are compared to Geocentric Axial Dipole (GAD) predicted inclinations (±73°) and modern inclination (−56°) for Site U1537. (c, d) Biplots of magnetic concentration parameters, κ and κ_{ARM} (c) and NRM and ARM after 15 mt peak AF demagnetization (d), and RPI proxies, the slope of NRM to ARM intensities between 15 and 40 mT peak AF and the ratio of the NRM after 15 mT peak AF demagnetization to κ (e). For all biplots, only every 5th u-channel measurement is plotted.

higher δRTSIRM and lower M_r/M_s, indicating potentially greater contribution from coarser magnetic particles in those samples (samples from Cores 25H and 31F; Figures 5b and 5e). The other three samples have maxima in their coercivity distributions along the H_c axis between 20 and 30 mT, indicating greater contribution from finer magnetic particles (samples from Cores 24H, 26H and 29F; Figures 5a, 5c and 5d). While central ridge features are often associated with magnetofossils, in all five samples, the broad coercivity distributions along the H_c axis, their relatively low peak coercivity values, and relatively higher Verwey Transition, >100 K, are more consistent with fine components in detrital assemblages than magnetofossils (Chang et al., 2016). The presence of these fine-grained magnetic particles is also supported by R_{LT} values greater than 1.1, which Smirnov (2009) found were related to fine (<150 nm) synthetic magnetite.

ARM intensity and variability, which is biased toward the concentration of finer-grained ferrimagnetic minerals (Maher, 1988), notably increases over our study interval, with lower values between ~265 and 285 mcd and higher values stratigraphically above that to ~220 mcd (Figure 3g). This transition is captured in the κ_{ARM}/κ ratio, which is considered a magnetic "grain-size" parameter and tracks the proportion of fine-grained ferrimagnetic minerals to total magnetic minerals assuming a consistent magnetic mineralogy (Banerjee et al., 1981; King et al., 1982) (Figure 3i). The ARM coercivity ratio (ARM_{30mT}/ARM) provides another perspective of magnetic "grain-size" by tracking how susceptible the fine-grained ferrimagnetic mineral assemblage is to AF

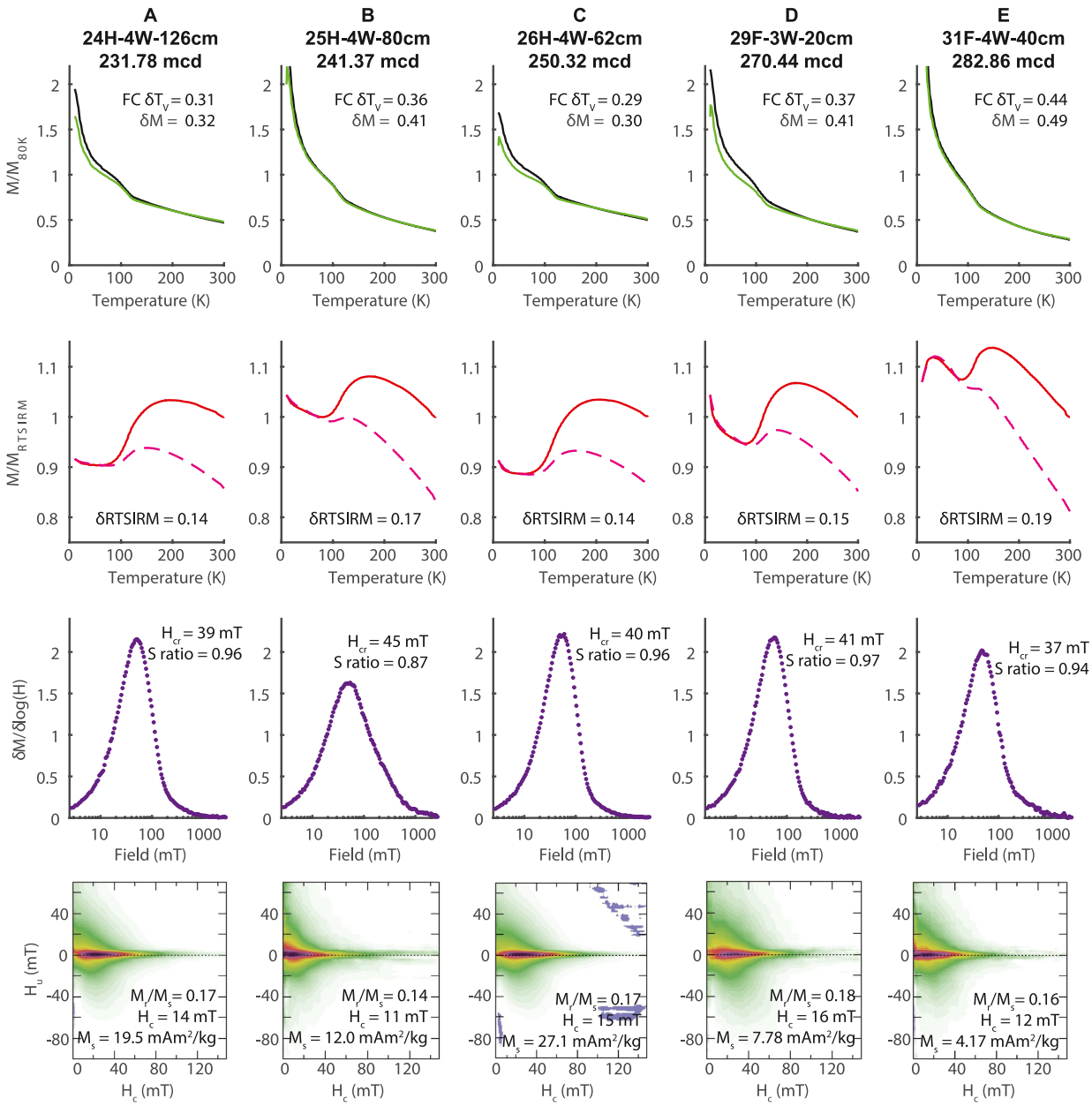

Figure 5. Detailed rock magnetic investigation of five samples over the study interval, including: FC (black) and ZFC (green) curves; LTC-RTSIRM curves (red is cooling, dashed magenta is warming); coercively spectra from DCD curves (purple); and FORC diagrams. Select parameters are indicated, as described in the text. Sample locations for (a–e) are indicated in Figure 3.

demagnetization (Stoner & St-Onge, 2007) (Figure 3h). These parameters also reveal cyclic variations in the composition of the magnetic mineral assemblages. However, we note that there is not a consistent magnetic mineralogy associated with the C2r.2r Chron BSEs and their associated anomalous inclinations (Figures 3h–3j).

To investigate potential RPI proxies, NRM intensity was normalized to control for magnetic mineral concentration in two ways. First, the slope of the best fit line of NRM intensities as a function of ARM intensities was calculated using the same 15–40 mT range used to calculate the ChRM (after the psuedo-Thellier method of Tauxe et al., 1995; see also Valet & Meynadier, 1998) (Figure 3l). 95% of these best fit lines have average r^2 values greater than 0.98 and the $\pm 1\sigma$ range of the standard error of the slope calculations is 0.001–0.006, indicating a good fit between the NRM and ARM coercivities in this range. Second, the NRM intensity after 15 mT peak AF was normalized by κ (after Harrison & Somayajulu, 1966) (Figure 3m). This method is more difficult to

assess and could be complicated by the fact that the normalizer is an in-field (non-remanence) parameter. However, it also has advantages, including that κ tracks a wider range of magnetic coercivities than ARM, and the NRM_{15mT}/κ ratio can be calculated using data collected during the expedition. Relative changes in normalized intensity are similar using the two methods; a strong long-period trend, however, exists in the slope calculated values that reflects the long-period trend in magnetic "grain-size," as tracked by κ_{ARM}/κ (Figures 3i, 3l, 3m and 4e). Ideal sediments for RPI analysis have well-defined ChRMs, have NRM coercivities that match the coercivity of the normalizer, and have little variation in magnetic "grain-size" (Tauxe, 1993); however, the latter of these conditions is rarely possible in natural samples, particularly in the dynamic environments where environmentally independent stratigraphic methods are more needed. While we reasonably meet the first two of these conditions, we also see significant magnetic "grain-size" variations, as illustrated on a Banerjee-King plot (Figure 4D) that is largely driven by the previously discussed long term trend in κ_{ARM}/κ (Figure 3h). Thus, in our correlation, we consider both RPI estimates derived from normalizing NRM intensity by ARM and by κ, as both show the same relative highs and lows but different long term trends (Figures 4l and 4m).

3.2. Assessment of Anomalous Inclinations

The two most prominent intervals of anomalous inclinations outside of interpreted polarity chron boundaries occur within the interval containing the BSEs. The interpretation of the origin of these two thicker intervals of anomalous inclinations is difficult because they are also associated with anomalous lithology and should be treated with caution. However, none of the u-channel samples that span this interval show any obvious indications of sediment deformation in CT imagery (Figures S6–S8 in Supporting Information S1).

For the upper event near the top of BSE1, located in U1537D-26H, we see indications that the inclination event is reproducible, including (a) similar shallow inclinations in overlapping sediments near the base of U1537A-25H and top of U1537D-26H in shipboard data; (b) reproduced inclinations in shipboard data and u-channel ChRM directions; and (c) reproduced u-channel ChRM directions below the event where u-channel sampling overlapped ~247–248 m (Figures 6b and 6c; Figure S14 in Supporting Information S1). Magnetic mineralogy and coercivity are not anomalous and not consistent with higher coercivity authigenic iron sulfides that can complicate paleomagnetic signals (e.g., Nowaczyk, Frank, et al., 2013) (Figures 3h and 3i). These observations indicate the origin of this inclination anomaly could be geomagnetic in nature. At least four intervals of geomagnetic instability have previously been documented in C2r.2r at Site U1314 using sediments from replicate intervals (Ohno et al., 2012), for which potential relationships will be discussed in Section 4.1.

In contrast to the BSE1 inclination feature, we consider the lower of the two thicker intervals of anomalous inclination, found near the base of BSE3 in U1537D-27H, unlikely to be of geomagnetic origin. This feature is associated with poorly defined magnetizations (Figure 3k), is not reproduced between shipboard data and u-channel ChRM directions, and appears to be the continuation of anomalous u-channel ChRM directions in U1537D-27H, above the splice tie point with U1537D-26H (Figures 6b and 6c; Figure S14 in Supporting Information S1). While the exact reason for these anomalous directions is unknown, differences between the two holes suggests that coring deformation in this low density lithology may be responsible.

Several less prominent inclination anomalies are also observed, and we consider three as possible candidates for geomagnetic excursions, in late C2r.1r, early C2r.2r and late C2An.1n (indicated by vertical yellow lines in Figure 3). We assess these features as plausible recordings of geomagnetic instabilities, based on comparisons to how events of similar timing are documented in other paleomagnetic studies in Section 4.1. There are likely more geomagnetic instabilities through this time interval that are not recorded or clearly recognized in U1537 sediments (e.g., comparing with the eight events recorded at Site U1314 between 2.1 and 2.75 Ma; Ohno et al., 2012; Figures S16 and S17 in Supporting Information S1). But this fact is not necessarily surprising, as deep sea sediments from the same basin often record some events and not others, potentially due to local variations in sedimentation rate (e.g., Channell, 2017), directional manifestations of excursions may vary across the globe during times of low dipole intensity (e.g., Brown et al., 2007), and smoothing by sediment magnetic acquisition processes and/or by u-channel measurements may hide short duration events (e.g., Roberts & Winklhofer, 2004).

3.3. Integrating U-Channel and Shipboard Data

While the u-channel data represent more pristine samples from the center of the cores and allow for more detailed analyses of NRM and magnetic mineral assemblages, the data collected during Exp. 382 on whole and half round

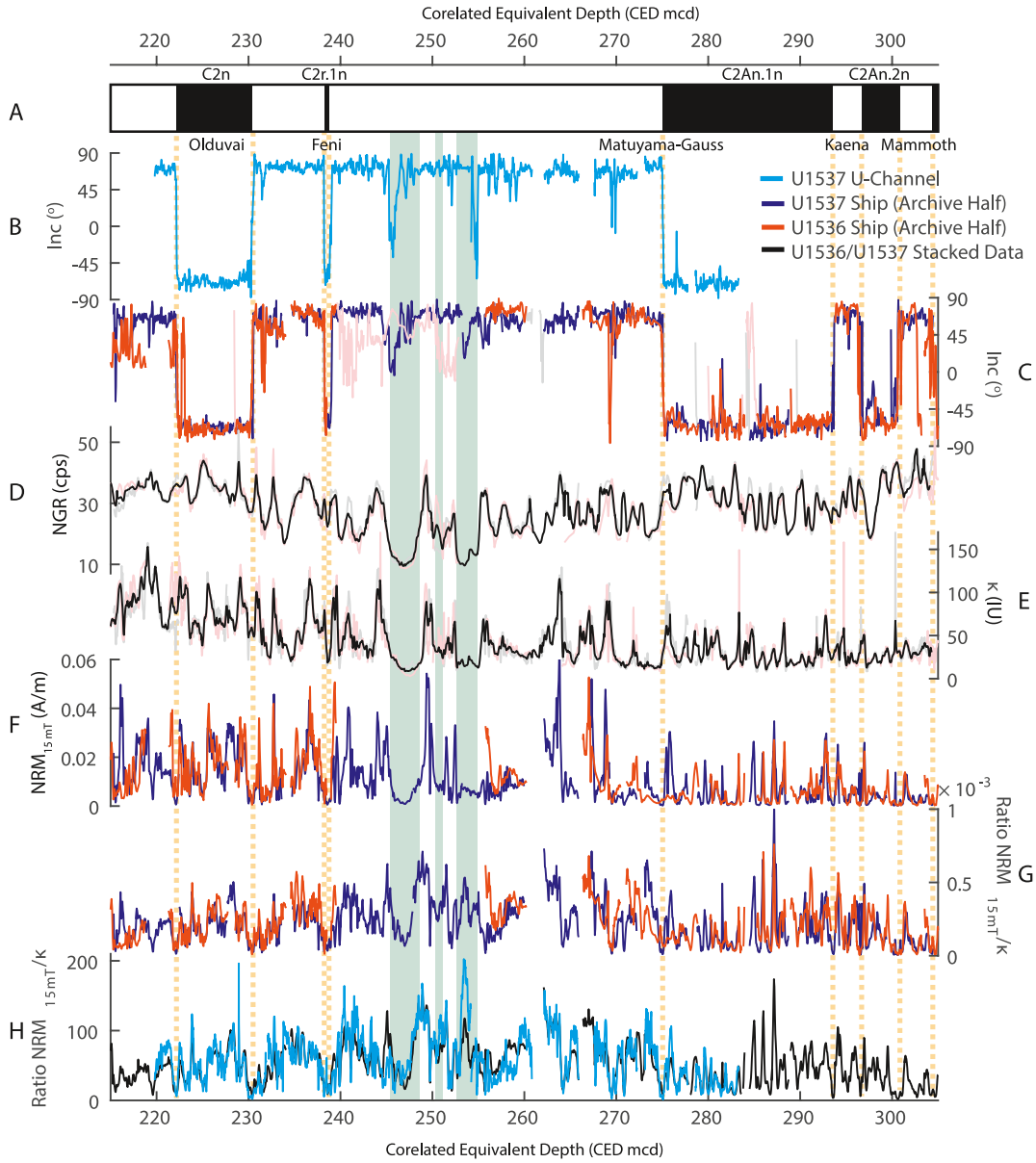

Figure 6. Comparison of U1537 U-Channel Data (cyan) to U1536 (orange) and U1537 (dark blue) shipboard data with Dove Basin data stacks (black) on the correlated equivalent depth (CED) scale of Reilly et al. (2021). (a) Polarity interpretation of Reilly et al. (2021). (b) U-channel ChRM inclination. (c) Archive half inclination after 15 mT AF demagnetization measured on ship. Light intervals are disturbed/complicated intervals. (d) Dove Basin NGR stack (black) with individual site data in light colors. (e) Dove Basin magnetic susceptibility (k) stack (black) with individual site data in light colors. (f) Archive half NRM intensity after 15 mT AF demagnetization. (g) Shipboard NRM intensity after 15 mT AF demagnetization normalized by k. (h) Comparison of u-channel derived RPI estimate to stacked Dove Bain RPI estimate data from (**G**. Vertical orange lines are reversal boundaries. Vertical green shading are the BSEs highlighted in Figure 3.

cores allow for tests of reproducibility between Dove Basin Sites U1536 and U1537, and allow us to extend our RPI reconstruction below Core U1537D-31F where sediments were recovered in a single hole. After removing intervals that are likely disturbed (light shading in Figure 6c) we compare data from Sites U1536 and U1537 using the previously established NGR-based correlation presented by Reilly et al. (2021), including: shipboard inclination after 15 mT peak AF demagnetization, NRM intensity after 15 mT peak AF demagnetization, κ, and the ratio of NRM after 15 mT peak AF demagnetization to κ (an RPI proxy) (Figure 6). Using these data, new stacks are generated that capture the variability in κ (Figure 6e) and the ratio of NRM after 15 mT peak AF demagnetization to κ (Figure 6h). We find excellent agreement between the two sites and with the u-channel data,

providing further support that we have reconstructed a normalized intensity record that is of high quality and representative of Dove Basin.

3.4. Dove Basin RPI Chronology: 1.75–3.14 Ma

We visually correlate the Dove Basin RPI proxies to the template discussed in Section 2.4 (Figure 2), extended to the base of the Kaena Subchron (C2An.1r) using the benthic $\delta^{18}O$ LR04 chronology of Site U1308 (Channell et al., 2016) to establish an RPI-based chronology from 1.75 to 3.14 Ma for Dove Basin Sites U1536 and U1537 (Figures 7a–7d; Figure S17 in Supporting Information S1). Correlations were established by working from the magnetic reversals toward the centers of each polarity zone. We did not establish any correlation lines around the base of BSE3, where anomalous inclinations indicate potentially complicated data (see discussion in Section 3.2). We establish a correlation and note the similarity in the two RPI signals on timescales of 10–100s of kyrs (Figure 7d). Moreover, we note that following our RPI correlation, the Dove Basin physical properties display intriguing, but imperfect relationships with both orbital variability, tracked by the normalized precession index plus obliquity with 3 and 7 kyr lags, respectively (lags approximated after Lisiecki & Raymo, 2005), and benthic $\delta^{18}O$ (Figures 7e and 7f). We explore these relationships and how they might be interpreted in the context of age model uncertainty in our discussion section.

As correlations such as these can be non-unique, we investigate potential uncertainty in our RPI-based age model using the Undateable MATLAB tools (Lougheed & Obrochta, 2019). While the magnetic reversals are treated in the same manner as in the Reilly et al. (2021) age model, considering the depth uncertainty in defining the reversal only, each RPI tie point is given a ±20 cm uncertainty in depth and ±5 kyr uncertainty in age, which are meant to account for uncertainties related to tie point location, imperfection in the template, and potential millennial scale offsets in regional geomagnetic field strength. While post-depositional remanent magnetization (pDRM) acquisition processes could potentially offset the geomagnetic signal anywhere from ∼0 to 20 cm (e.g., Channell & Guyodo, 2004; deMenocal et al., 1990; Simon et al., 2018; Stoner et al., 2013; Tauxe et al., 1996), we consider this additional source of uncertainty negligible relative to the uncertainties we already provide, given the similar sediment accumulation rates in Dove Basin and the sites used to build our template. However, pDRM offsets could be variable and have a larger impact in lower accumulation rate intervals. The Undateable age-depth model was run 1,000 times, using an *x-factor* = 0.1 and bootstrapping only 75% of the RPI tie points in each model run to allow for the age-model uncertainty structure to accommodate the possibility that only a subset of our tie points are correct (Figure 8a). The final age-depth model results in average ±1 sigma uncertainty of ∼5.3 kyr, with uncertainties as high as ±10–15 kyr around 2.15–2.25 Ma and 2.75 Ma, where a lower density of RPI tie points exists. 1.7–3.2 Ma sedimentation rates, calculated in 10 kyr bins, have a median of 4.7 cm/kyr and 95% interval of 1.7–11.5 cm/kyr (Figure 8b). We assess this age model further, including potential unquantified uncertainties, in our discussion section.

4. Discussion

4.1. Timing of 1.75–2.80 Ma Dove Basin Excursions

The anomalous inclinations at Site U1537 discussed in Section 3 are placed on the following ages on this chronology: 1.967, 2.247, 2.527/2.538, and 2.625 Ma (Table 1). We discuss the stratigraphic context for these early Pleistocene and latest Pliocene excursions and summarize these observations in age and in relation to MIS names in Figure S18 of Supporting Information S1.

The youngest event in our u-channel record is found near the end of a low density interval below the base of the Olduvai Subchron (C2n) (Figures 3c, 3j, 6b and 6c). Our age model places this event at 1.967 Ma at the transition from MIS 75 to 74 (Figures 3 and 6 and Figure S18 in Supporting Information S1), consistent with an excursion previously documented at ODP Site 984, Bjorn Drift, at the top of the first interglacial interval below the Olduvai Subchron, preceding the reversal by ∼32 ka and named 2r.1r.1n at Site 984 (Channell et al., 2002). While they place this event at the top of MIS 73, 1.977 Ma, this was based on prevailing timescales that placed the base of the Olduvai Subchron (C2n) in MIS 71 with ages ranging from 1.94 to 1.95 Ma (Lourens et al., 1996; Shackleton et al., 1990). However, the actual assignment to MIS 71 came from DSDP Site 677, which did not in itself have paleomagnetic data that defined the reversal; rather, the position was determined by the last occurrence of the calcareous nannofossil *Discoaster brouweri*, which was observed to have occurred close to the base of the Olduvai in the North Atlantic and Italian sections (Raymo et al., 1989; Ruddiman et al., 1986; Shackleton

10.1029/2025PA005360

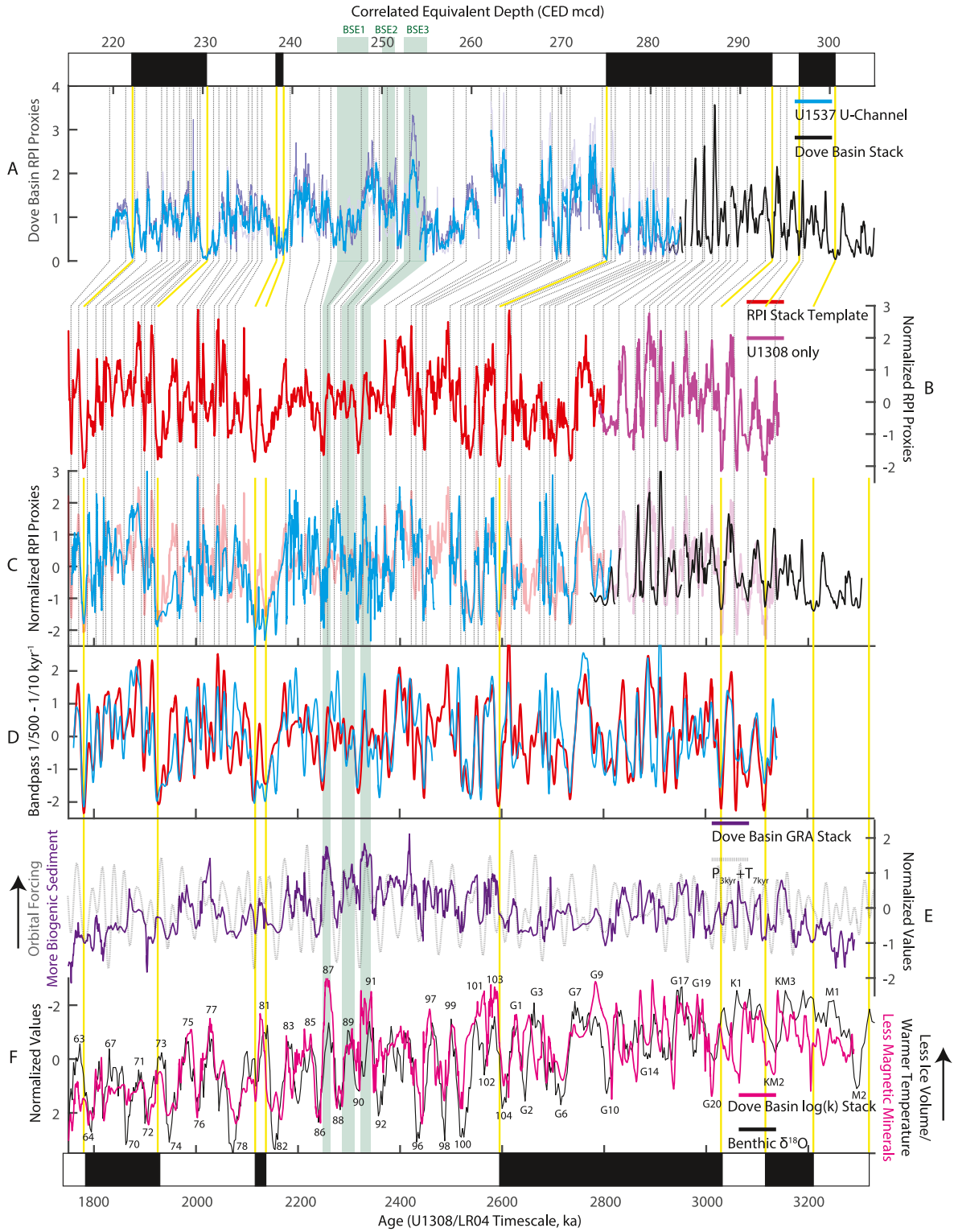

Figure 7.

et al., 1990; Tauxe et al., 1983). This assignment has since been challenged by the high resolution and co-registered benthic $\delta^{18}O$ and paleomagnetic record from Site U1308, which placed the base of the Olduvai in interglacial MIS 73 (Channell et al., 2020, 2016; the timescale constraint we use in this study), at 1.925 on the LR04 timescale (Lisiecki & Raymo, 2005). A prominent RPI minimum from ~1.964 to 1.974 Ma at Site U1308 is firmly within the second half of MIS 75 with a midpoint 44 kyr prior to the base of the Olduvai in MIS 73 (Channell et al., 2016; Lisiecki & Raymo, 2005). As far as we are aware, Sites U1536, U1537, and 984 are the only locations where a directional excursion is documented at this stratigraphic position. We note that this excursion is distinct from an Olduvai precursor event documented and discussed at ODP Site 981 (Channell et al., 2003) and in Lake El'gygytgyn (Haltia & Nowaczyk, 2014; Nowaczyk, Haltia, et al., 2013), as this precursor and the reversal itself occurs within the same interglacial, ~10 kyr apart. A radiometric date from a low latitude VGP (2.6°N) site from the Erebus Volcanic Province, Royal Society Range, Antarctica, dates to within the uncertainty of this event at 1.9 ± 0.12 Ma (site mc1145; Asefaw et al., 2021) with new results also indicating low absolute paleomagnetic intensity (Tauxe et al., 2025); however, this age is also within the age uncertainty of the base of the Olduvai Subchron (C2n). We are not aware of any other higher precision radiometric dates from lava flows that are related to this event, with the closest radiometric age included in a recent compilation from transitional directions in the Huckleberry Ridge Tuff in Yellowstone, WY, USA of around 2.078 Ma (Channell et al., 2020; Singer et al., 2014)—111 kyr older than the late MIS 75 event we describe (Table 1).

An excursion at 2.247 Ma is placed at the transition from MIS 87 to 86 (Figures 3 and 6 and Figure S18 in Supporting Information S1), consistent with the L1 event documented at Gardar Drift Site U1314, recalculated to have an age of 2.248 Ma on our updated U1314-U1308 NGR correlated chronology (Figure 2) (2.25 on the original Ohno et al., 2012 chronology) and an event at the MIS 87 to 86 transition at Eirik Drift Site U1307 (Blake-Mizen et al., 2019). At the lower accumulation rate Site 982 (~1–2 cm/kyr between MIS 82 and 94), there is also an unnamed event at 2.24 Ma which is placed in MIS 85/86 on their $\delta^{18}O$ chronology (Channell & Guyodo, 2004; Laj & Channell, 2007). At Lake E'gygytgyn, a prominent shallow inclination is also observed at MIS 87 (Nowaczyk, Haltia, et al., 2013). Recent work on IODP Expedition 395 Holes U1555H and U1563a also recognize several excursions below the Feni Subchron in early Matuyama Chron C2r.2r, including excursions e14 (U1555H) and e12 (U1563A) that they correlate to the Site U1314 L1 event (Di Chiara et al., 2025). The thickness of this event at Site U1537, could be explained by the high accumulation rates our age model estimates for MIS 87 and the relative thickness of this cycle (5.5 m) compared to other cycles (Figures 3 and 8). This timing is in close agreement with the 2.20 ± 0.01 Ma updated radiometric date for the Reunion event, a short lived geomagnetic instability predating C2r.1n (formerly referred to as the Reunion Subchron, now referred to as the Feni Subchron in the GTS20 Timescale; Channell et al., 2020; Gradstein et al., 2020; Singer et al., 2014). Thus it is plausible that the Reunion excursion, defined by this radiometric age, occurred at the MIS 87/86 boundary, providing an opportunity for further intercalibration of radiometric and benthic $\delta^{18}O$ timescales (c.f., Balbas et al., 2016; Barker et al., 2022; Channell et al., 2020; Singer, 2014).

The double anomalous inclination event in the earliest Matuyama has inclination lows at 2.527 and 2.538 Ma during the transition into MIS 100 (Figures 3 and 6, and Figure S18 in Supporting Information S1). This is consistent with the 11 kyr long L4 excursion at Site U1314, recalculated for the two anomalous inclinations to have ages of 2.530 and 2.538 Ma on our updated U1314-U1308 NGR correlated chronology (Figure 2) (2.53–2.55 Ma on the original Ohno et al., 2012 chronology), a prominent 2.52 Ma early MIS 100 event at Site U1307 (Blake-Mizen et al., 2019), an inclination anomaly in early MIS 100 at Lake El'gygytgyn (Nowaczyk, Haltia, et al., 2013), and excursions described in IODP Expedition 395 materials, e16 in Hole U1555H and e14 in Hole U1563A, that have been correlated to the Site U1314 L4 event (Di Chiara et al., 2025). These ages are consistent with the 2.514 ± 0.039 Ma radiometric data for the Halawa event from Hawaii (Herrero-Bervera et al., 2007) and a 2.56 ± 0.13 Ma low 9 ZAm^2 virtual axial dipole moment with shallow normal 50° VGP latitude from the Erebus

Figure 7. (a–c) Correlation of Dove Bain RPI proxies (blue, black) to the RPI template presented in Figure 2 (dark red in b and light red in c), extended by the benthic $\delta^{18}O$ age calibrated U1308 record (Channell et al., 2016) to 3.142 Ma (dark purple in b and light purple in c). U-channel data (blue lines in a and c) represent the mean of u-channel ARM and k normalized data (lighter purple and darker purple lines in a, respectively). RPI tie points are dashed gray lines and magnetic reversals are dashed yellow lines. (d) Comparison of bandpass filtered (1/500–1/10 kyr^{-1}) Dove Basin (blue) and North Atlantic (red) RPI proxies. (e, f) Implications for the timescale of density variations, a proxy for biogenic versus lithogenic sediments in Dove Basin, (purple) and magnetic susceptibility variations (pink) are compared with normalized and summed orbital curves with time lags previously documented for this time interval (gray) and benthic $\delta^{18}O$ (black). An expanded version of this figure to show greater detail is presented as Figure S17 in Supporting Information S1.

10.1029/2025PA005360

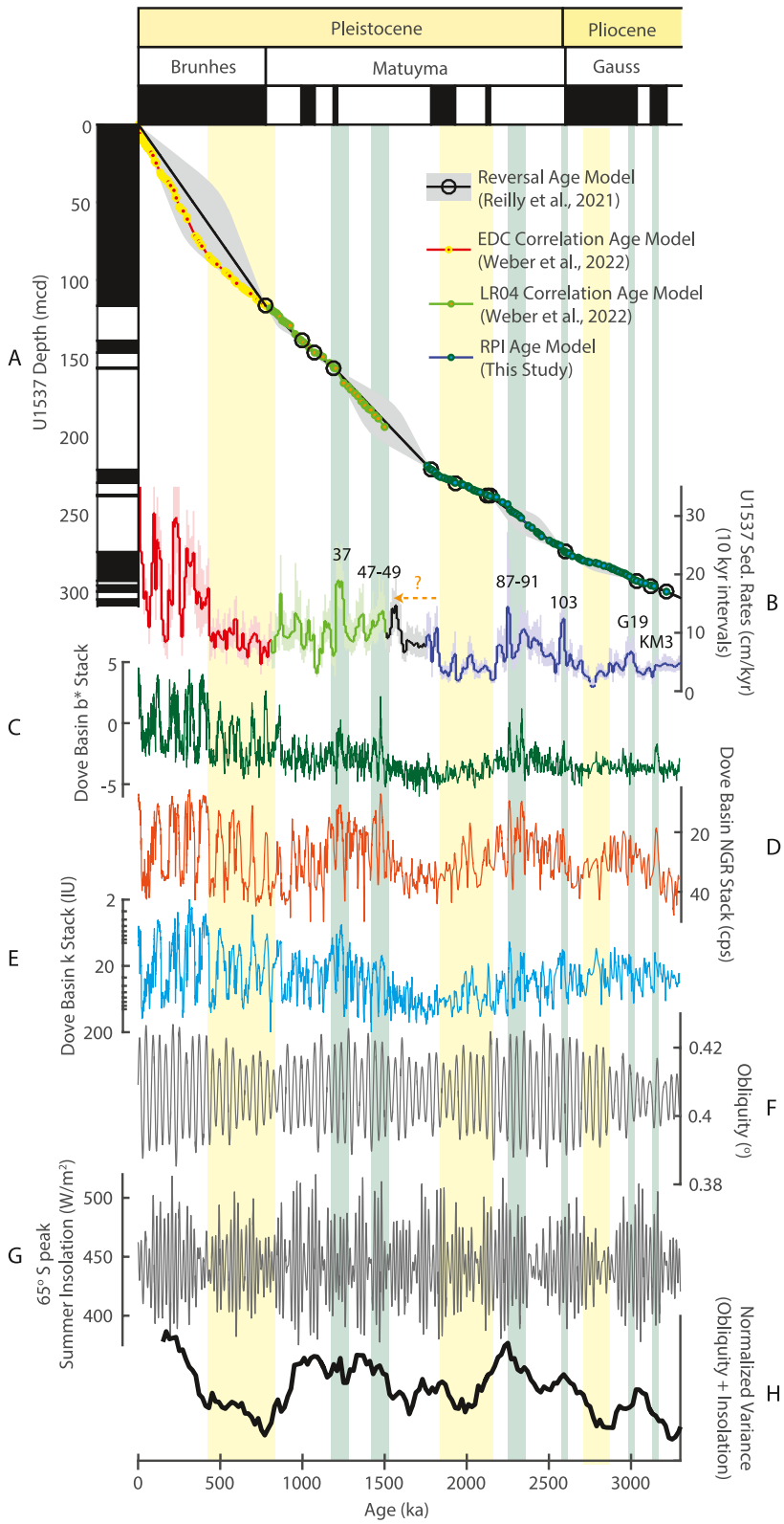

Figure 8.

Volcanic Province, Antarctica (site mc1306; Asefaw et al., 2021). Given the long duration of this event at Sites U1536, U1537 and U1314, the so-called Cryptochron C2r.2r-1, located 54% of the way across C2r.2r along the CK92 South Atlantic spreading center (Cande & Kent, 1992), may be a correlative event and has previously been suggested to potentially be associated with the Halawa excursion (Channell et al., 2020; Herrero-Bervera et al., 2007; Singer, 2014). The age of Cryptochron C2r.2r-1 can be updated to 2.37–2.40 Ma assuming constant spreading rates during C2r.2r on the GTS20 Timescale (Gradstein et al., 2020). Given this assumption, C2r.2r-1 is ∼130 kyr younger than this long duration excursion in early MIS 100 and outside of the ±2 sigma uncertainty range for the Halawa excursion radiometric age, implying these events are either unrelated or spreading rates were not constant during C2r.2r. However, using an age of 2.53 Ma for the midpoint of the C2r.2r-1 "tiny wiggle" would implicate spreading rates of 43.5 m/Myr prior to the event and 8.6 m/Myr after the event—spreading rates that are well outside of the range of expected values for the Pliocene and Pleistocene. Ohno et al. (2012) document a different event, L3, during glacial MIS 96, at 2.448 Ma on our updated U1314-U1308 NGR correlated chronology (Figure 2) that may be a better candidate for Cryptochron C2r.2r-1. Similar to the above, the low accumulation rate at ODP Site 982 also finds an event around this time at 2.421 Ma; however, this event has been placed slightly younger in MIS 95 (Channell & Guyodo, 2004; Laj & Channell, 2007). A second, younger excursion is also supported by Holes U1555H and U1563a that displays anomalous inclinations that they correlate to the Site U1314 L3 event, e15 and e13 respectively (Di Chiara et al., 2025). Transitional directions from Santiago Island, Cape Verde that are bracketed by ages of 2.38 ± 0.05 Ma and 2.41 ± 0.04 Ma (Knudsen et al., 2009) are also more consistent with the L3 event in MIS 96 and more constant spreading rates along the CK92 South Atlantic transect in C2r.2r. We thus propose that the early MIS 100 event might best be associated with the Halawa excursion, while the MIS 96 event (and possibly C2r.2r-1) may be associated with the Santiago excursion.

Finally, an anomalous inclination at 2.625 Ma falls in the middle of interglacial G1, consistent with the 2.62 Ma L5 event documented at Site U1314 (Ohno et al., 2012) (Table 1; Figure S18 in Supporting Information S1). As far as we are aware, Site U1314 is the only other location where an excursion is documented relative to MIS G1, although an excursion named e17 is described at IODP Hole U1555H with a 2.62 Ma age consistent with linear extrapolation of the sedimentation rates in early Matuyama Chron C2r.2n (Di Chiara et al., 2025).

4.2. Long Term Patterns in Dove Basin Sedimentation

Unsurprisingly, the RPI-based age model we present in this study implies non-linear accumulation rates for Site U1537 between magnetic reversals from 1.75 to 3.14 Ma, similar to those proposed for the last 1.5 Myr by Weber et al. (2022) (Figures 8a and 8b; Figure S19 in Supporting Information S1). Here we describe this variability on both orbital (single glacial-interglacial cycle) and longer-term (multiple glacial-interglacial cycles) timescales. Our age model is characterized by a relatively long-term interval of high accumulation rates between 2.2 and 2.7 Ma and low accumulation rate intervals on either side between 1.84–2.18 Ma, and 2.75–2.85 Ma. These accumulation rate changes are consistent with long-period lithologic changes that track the relative contribution of biogenic versus lithogenic sediments, previously discussed by Reilly et al. (2021). Broad periods of low (high) accumulation rates are associated with broad periods of high (low) NGR and GRA and low (high) b*, indicating decreased (increased) contribution of diatom-rich biogenic sediments (Figures 8b–8d). We find our new Dove Basin κ stack also shows long period variations, including a broad interval of high κ centered around 1.75 Ma, around the lower accumulation rate, higher NGR, higher relative terrigenous content interval (Figures 8b–8e). However, the κ stack does not perfectly follow NGR, indicating that on these timescales, as observed for the late Quaternary (e.g., Pugh et al., 2009), changes in κ cannot be fully explained by dilution of a constant magnetic concentration by biogenic sediments, but must also require changes in the composition of the terrigenous sediments being deposited at Site U1537. Long term changes in the composition of the magnetic mineral assemblage are supported by changes in κ_{ARM}/κ values that mimic trends in XRF ratios that trace sediment composition, such as the Ti/K ratio, over multiple orbital cycles (Figures 9d and 9e). When compared to the 0–1.5 Ma Weber

Figure 8. (a) Age depth-models for Site U1537 (including Reilly et al., 2021; Weber et al., 2022). (b) Sedimentation rates calculated in 10 kyr intervals, with color changes corresponding to the different methods used to construct the age models over each time slice. (c, d) Physical properties stacks from Dove Basin: b*, natural gamma radiation (NGR), and magnetic susceptibility (κ) (Reilly et al., 2021). (f, g) Laskar et al. (2004) obliquity curve and peak summer insolation for 65°S. (h) Normalized variance for summed obliquity and insolation curves calculated in a 300 kyr moving window (see Figure S19 in Supporting Information S1 for a more detailed comparison). Yellow shading highlights intervals of relatively long periods of low sedimentation rates.

Table 1
Summary of Observed Geomagnetic Instabilities at Site U1537 for the Latest Pliocene and Early Pleistocene

Excursion observed at U1537	Equivalent U1314 L-event[a]	Other sedimentary sections observed	U1537 age (Ma)	MIS (LR04)[b]	Potential radiometric age (Ma)
Unnamed (one interglacial below the Lower Olduvai)		984[c]	1.967	74/75	1.9 ± 0.12 (?)[d]
Reunion	L1	982(?)[e], U1307[f], U1314[a], U1555H(?)[g], U1563A(?)[g], Lake El'gygytgyn[h]	2.248	86/87	2.20 ± 0.01 (?)[i]
Halawa	L4	U1307[f], U1555H(?)[g], U1563A(?)[g], Lake El'gygytgyn[h]	2.527/2.538	Early 100	2.514 ± 0.039[j]
Unnamed	L5	U1314[a], U1555H(?)[g]	2.625	G1	

[a]Ohno et al., 2012. [b]Lisiecki & Raymo, 2005. [c]Channell et al., 2002. [d]Asefaw et al., 2021. [e]Channell & Guyodo, 2004. [f]Blake-Mizen et al., 2019. [g]Di Chiara et al., 2025. [h]Nowaczyk, Haltia, et al., 2013. [i]Singer et al., 2014. [j]Herrero-Bervera et al., 2007.

et al. (2022) age model, we see a similar relationship between long-term accumulation rates and lithology for the ∼1.0–3.3 Ma interval, however a lower accumulation rate interval from ∼0.5 to 1.0 Ma does not fit this pattern (Figure 8).

At higher frequencies, our age model also implies intervals of high accumulation rate with changes on timescales less than 100 kyr. Like the long-term patterns, these intervals of high accumulation rates are often associated with the deposition of high concentrations of biogenic sediments, tracked by high b* and low NGR values. While this relationship does not seem to hold in the 0.5–1 Ma interval of the Weber et al. (2022) 0–1.5 Ma chronology, high accumulation rates and high b* values do appear to have been a feature of multiple interglacial periods of the mid to late Brunhes Chron (MIS 1, 5, 7, 9, and 11) and select interglacial intervals between 1.2 and 1.5 Ma—most notably MIS 37, but also MIS 47 and 49. We find high accumulation rates and anomalous b* values during the 3 BSE intervals in C2r.2r, which our age model implies were formed during interglacials MIS 87, 89, and 91 (Figure 8b). Other intervals that fit this pattern of anomalously high accumulation rate and high biogenic component on our age model include the interglacials MIS 103 and G19. While our RPI age model does not extend beyond 3.14 Ma, anomalously high b* and low NGR are also found just below the Kaena subchron in the time interval around the interglacial MIS KM3 (Figures 8b–8e). For the late Quaternary, Hallmaier et al. (2025) document that U1537 interglacials are characterized by high biogenic opal flux and changes in sediment focusing factors. Thus, these high biogenic opal and high accumulation intervals may be associated with both increases in primary productivity and increases in lateral sediment transport.

As previously discussed in detail by Reilly et al. (2021), these long-term physical property patterns in Dove Basin lithology closely match long wavelength patterns in the amplitude modulation of Earth's orbital changes, such as the ∼1.2 Myr period in obliquity and 0.4 Myr period in precession, as modulated by eccentricity (Figures 8f and 8g). Here, we document that long term changes in sedimentation rates also follow these patterns and appear to reflect the combined influence of obliquity and precession. To capture time variations in the amplitude of orbital forcing, we sum the normalized variance of peak summer insolation and the normalized variance of obliquity in a moving 300 kyr window. This shows that intervals of lower accumulation rates at Site U1537 are associated with intervals of lower amplitude changes of both obliquity and precession, while higher accumulation rate intervals are associated with greater variance (Figure 8h; Figure S19 in Supporting Information S1). Notably, the interglacial intervals discussed previously that have both high accumulation rates and high biogenic components are systematically located near the intervals with highest variability in both precession and obliquity. These periods of heightened variability in orbital forcing may be important for increasing the probability of extreme interglacial expressions in both high southern and northern latitudes. This suggestion is supported by the lithologic record of Arctic Lake El'gygytgyn in northeastern Russia, which records anomalous facies of reddish-brown laminated silts with high Si/Ti ratios that were seemingly deposited at the same time as many of these late Pliocene to early Pleistocene interglacials, including at MIS 49, 87, 91, 103, and KM3 (Brigham-Grette et al., 2013; Melles et al., 2012) (Figures 8, 9i and 9j).

10.1029/2025PA005360

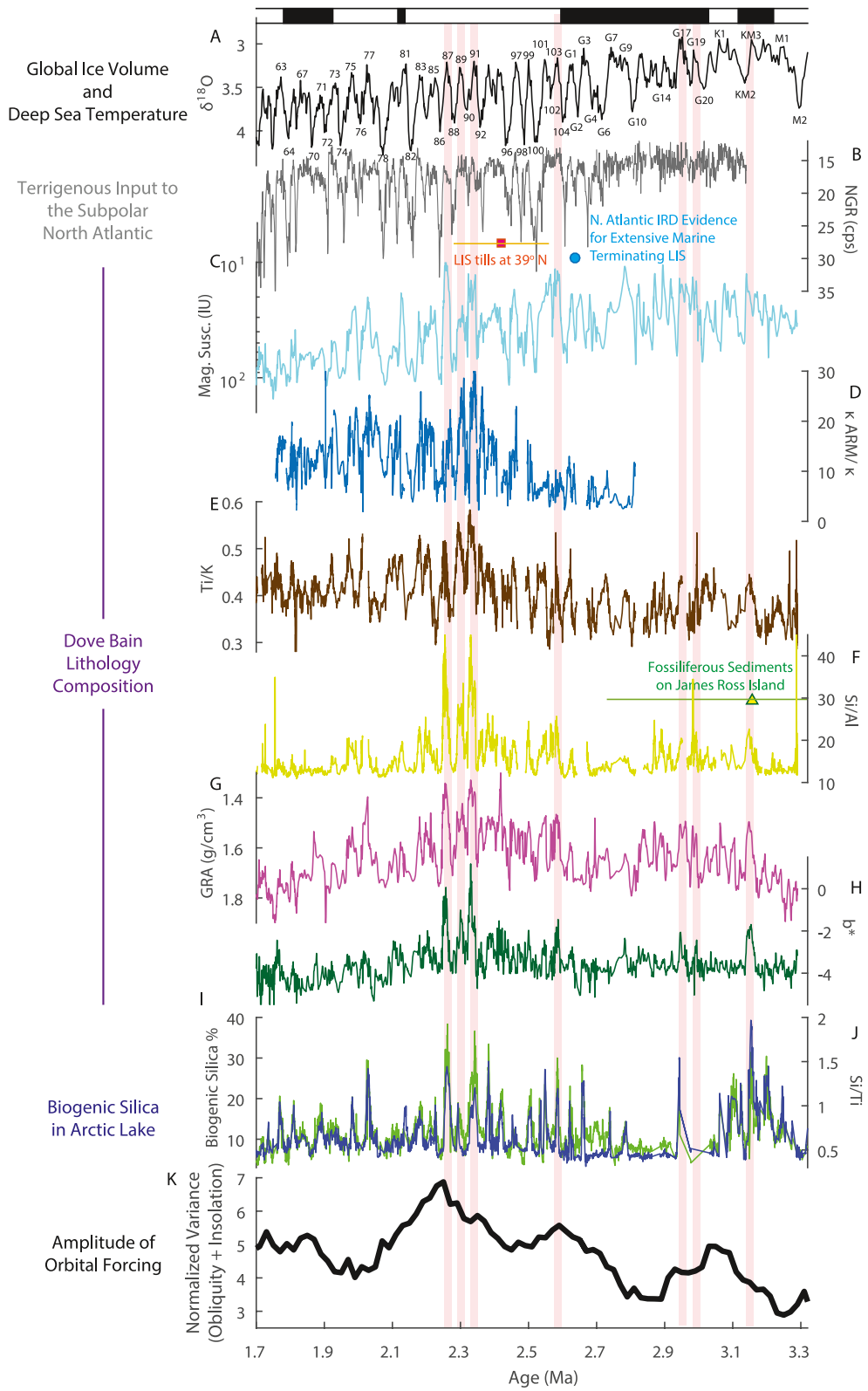

Figure 9.

4.3. Assessing the RPI Chronology on Glacial-Interglacial Timescales

Tie points between sediment logarithm of κ and the LR04 benthic $\delta^{18}O$ stack have been used to help construct a chronology for Site U1537 sediments for the last 1.5 Ma (see Figure 4a in Weber et al., 2022). It is therefore noteworthy that our correlation of the Dove Basin RPI record to the benthic $\delta^{18}O$ calibrated North Atlantic RPI template reveals a remarkably and independently derived close correspondence between the logarithm of the Dove Basin κ stack and LR04 variations despite differences in long-term trends (Figure 7f), consistent with the assumptions used in the previously published highly resolved chronology. However, we also note that, although strong, this relationship is not perfect. Specifically, the apparent timing of terminations and inceptions are often offset and, in some cases, there are extra or missing "stages" implied—for example around MIS G3 and between MIS K1 and M1 (Figure 7f). As discussed in Section 3.4, our estimates of the uncertainty in our chronology are on the order of 5 kyr, and there may be additional sources of uncertainty not quantified here. To address such uncertainties, we use a newly designed Dynamic Time Warming (DTW) experiment to explore objective correlation results, in comparison to our supervised RPI correlation, while varying assumptions and tuning targets used to develop our chronology.

DTW utilizes dynamic programing to find optimal alignments between time series data and has been used extensively in the geoscience and paleomagnetic communities (Channell et al., 2009; Clark, 1985; Hagen et al., 2020; Hay et al., 2019; Lisiecki & Lisiecki, 2002; Lisiecki & Raymo, 2005; Reilly et al., 2023; Thompson & Clark, 1989). Here we utilize a simple DTW algorithm that first calculates the squared difference between every possible pairing of strata between a target template and a candidate record (in this case proxies from our Dove Basin record) to populate a "cost matrix." However, in this application, rather than using just a single target record and single candidate record, we populate the "cost matrix" with several pairs of target and candidate records, with each record normalized to a mean of zero and unit variance. Weighting factors are then applied to the squared differences for each pair of target and candidate records to determine how important each pair is for the "cost matrix" calculation. Given our high confidence in the designation of the magnetic polarity boundaries relative to the LR04 benthic $\delta^{18}O$ timescale (Reilly et al., 2021), we calculate a cost matrix for each polarity chron and then solve for the optimal path following the approach of Hay et al. (2019) and Hagen et al. (2020), excluding any additional constraints such as their "g" and "edge" parameters.

In our experiment, we seek to find if there are objective correlations that find good correlation to a combination of:

1. Dove Basin RPI to our benthic $\delta^{18}O$ calibrated North Atlantic RPI template,
2. the relative proportion of biogenic to terrigenous sediments, tracked by GRA, to local orbital forcing, tracked by normalized precession plus obliquity with time lags of 3 and 7 kyr, respectively (e.g., Figure 7e; c.f. Reilly et al., 2021), and
3. the logarithm of κ to LR04 benthic $\delta^{18}O$ (e.g., Figure 7f; c.f. Weber et al., 2022).

Given the potential for non-uniqueness in signal correlation, using RPI stratigraphy in concert with stratigraphic correlation of other signals has proved to be a successful means of achieving a more meaningful and higher resolution chronology than could be possible by any single method alone (e.g., Channell et al., 2014; Hatfield et al., 2021; Stoner et al., 2000; Xuan et al., 2016). In Figure 10, we present a result where we assign a weighting factor of 1 to the RPI correlation and inverse weighting factors between 0 and 1 for the GRA and logarithm of κ correlations. We find the majority of DTW solutions fall within the uncertainty structure of the Undatable age-depth model calculated from our supervised RPI correlation (Figures 8a, 10a and 10b). Notably, we often find "stable" solutions where the various DTW solutions follow the same age-depth relationship, highlighted as a thick black line in Figure 10b. This "stable" solution only falls outside the uncertainty structure of our supervised correlation at ~2.7 Ma, which also corresponds to where our supervised correlation places very low accumulation rates (~1.5 cm/kyr) and NGR values indicate an interval with relatively high terrigenous concentration

Figure 9. Interhemispheric proxy data through our study interval, including (a) benthic $\delta^{18}O$ (Lisiecki & Raymo, 2005), (b) NGR from our composite Site U1308-U1314 record (Figure 2) with indication for southern expansion of an extensive Laurentide Ice Sheet (LIS) through IRD provenance (Bailey et al., 2013) and cosmogenic dating of tills in Missouri, USA (Balco & Rovey, 2010), (c–h) Lithologic, XRF and magnetic parameters for the Dove Basin (Figures 3 and 8), with Sr isotope age constraint for the age of the youngest warm open marine fossiliferous deposit documented on James Ross Island (Bertoa del Llano et al., 2021) (i, j) Si/Ti (green) and percent biogenic silica from Lake El'gygytgyn (Brigham-Grette et al., 2013; Melles et al., 2012), and (h) summed normalized variance of obliquity and peak summer insolation at 65°S (Laskar et al., 2004), calculated in a moving 300 kyr window. Pink shading highlights times of high accumulation and high biogenic silica at Site U1537 discussed in the text.

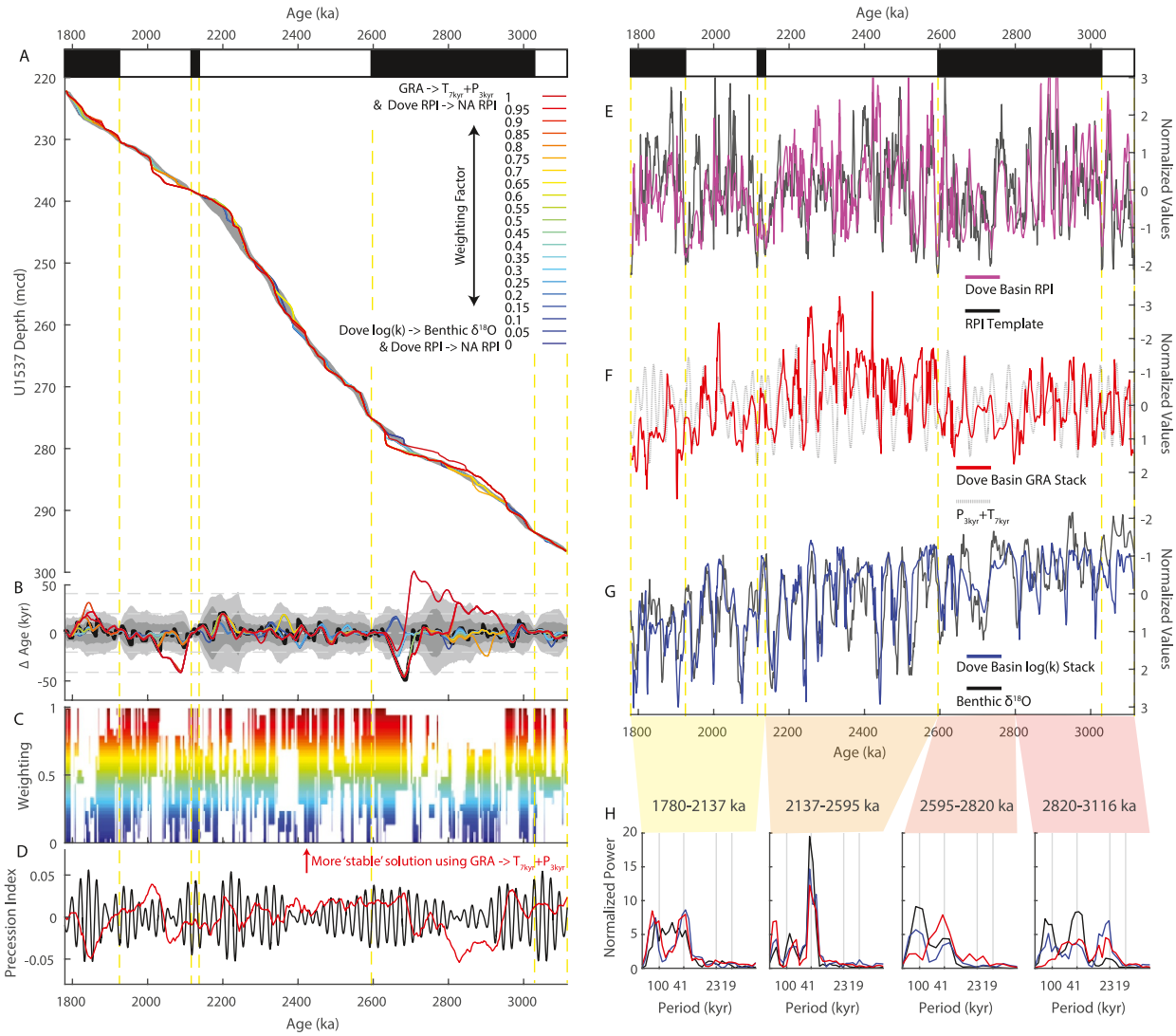

Figure 10. (a) Age-depth relationships for DTW experiments that use RPI correlation and vary the weighting correlating the Dove Basin GRA stack to precession (3 kyr time lag) plus obliquity (7 kyr time lag) and the Dove Basin logarithm of magnetic susceptibility stack (log(k)) to benthic $\delta^{18}O$. Gray shading indicates the age model uncertainty of our supervised RPI correlation (Figures 7 and 8). (b) Difference in age between each DTW solution and our supervised RPI correlation. Gray shading indicates the age model uncertainty of our supervised RPI correlation. (c) Indication of which weighting schemes resulted in a "stable" solution replicated between the different DTW solutions. (d) Average of the weighting parameters in (c) compared to the precession index (Laskar et al., 2004). (e, f) Implication of the "stable" DTW solutions for the Dove Basin parameters and the targets they are correlated to. (h) Frequency spectra of four time intervals of Dove Basin GRA (red), Dove Basin logarithm of magnetic susceptibility (blue), and benthic $\delta^{18}O$ (black; Lisiecki & Raymo, 2005).

(Figures 8b and 8d). The weighting factors between the Dove Basin GRA versus the logarithm of κ correlations used in the DTW solutions that contribute to this "stable" solution varies as a function of time (Figure 10c), and, prior to ~2.1 Ma, may in part reflect the amplitude modulation of the precession index (Figure 10d).

We apply the age-depth relationship of the "stable" DTW solutions to our data (Figures 10e–10f) and calculate the frequency spectra in four time intervals for benthic $\delta^{18}O$, the Dove Basin GRA stack, and the Dove Basin logarithm of κ stack using the multi-taper method: Chrons C2n–C2r.1n (1,780–2,137 ka), Chron C2r.2r (2,137–2,595 ka), the low accumulation rate interval at Site U1537 in late Chron C2An.1n (2,595–2,820 ka), and below the low accumulation rate interval to the base of C2An.1r (2,820–3,116 ka) (Figure 10h). For the younger two intervals in the Pleistocene, the frequency spectra are nearly identical for benthic $\delta^{18}O$ and the Dove Basin parameters with strong variability at the 41 kyr obliquity period. However, in the 2,820–3,116 ka interval in the late Pliocene, the Dove Basin parameters clearly show a much stronger response than benthic $\delta^{18}O$ at the 23 kyr precession period, implying greater sensitivity to local peak summer insolation.

This DTW analysis highlights the usefulness of RPI stratigraphy in depositional environments like those found in the Scotia Sea. While deep-sea lithologic records often display signals of orbital driven environmental change, it can be challenging to find unique correlations of these signals. Identifying the appropriate tuning target also often requires assumptions that are difficult to test. RPI provides a stratigraphic method independent of these climate variabilities that can help both identify more unique correlations and provide an independent assessment of the underlying drivers of these lithologic variations.

4.4. Implications for Antarctic Climate Around the Plio-Pleistocene Transition

Our RPI-constrained chronology for the Dove Basin provides further evidence for the strong sensitivity of Scotia Sea lithology to orbital forcing and here, for the first time, documents a clear change in this lithologic sensitivity at or just prior to the Pliocene-Pleistocene Boundary around 2.6–2.8 Ma (Figure 10h). Transitions in the sensitivity of the Antarctic Ice Sheet around this time have previously been suggested from relative sea level reconstructions from the Wanganui Basin in New Zealand that find variability at precession and eccentricity timescales between 2.7 and 3.3 Ma and variability at obliquity timescales after (Grant et al., 2019), and in the precession and eccentricity paced variability of IRD flux to the Wilkes Land margin between ∼3.5 and 2.5 Ma (Patterson et al., 2014). The timing of this change occurs around the final benthic $\delta^{18}O$ defined Pliocene glacial intervals—the G6, G4, and G2 glacials (2.64–2.73 Ma). This late Pliocene time may have also occurred in combination with anomalous warmth in the Weddell Sea sector, with evidence for warm-indicating fossiliferous marine sediments within volcanic deposits of Cerro Domo, James Ross Island, dated to 3.16 (+0.59, −0.42) Ma using strontium isotopes and further constrained by limiting volcanic $^{40}Ar/^{39}Ar$ ages to have been deposited between 3.57 ± 0.19 and 2.72 ± 0.09 Ma (Bertoa del Llano et al., 2021) (Figures 9f–9h).

These MIS G6-G2 glacial intervals are critical times in the expansion of large marine-terminating ice sheets in the Northern Hemisphere, with a deep-sea temperature corrected benthic $\delta^{18}O$ indicating eustatic sea level may have been up to 100 m lower than present during MIS G6 (Jakob et al., 2020), although other estimates suggest a more modest sea level fall of ∼45 m from the preceding interglacial (Rohling et al., 2014). The onset of higher NGR values at Sites U1308 and U1314 (Hodell & Channell, 2016), the onset of widespread occurrence of IRD throughout the Nordic Seas and subpolar North Atlantic (Kleiven et al., 2002) with IRD provenance in the North Atlantic, ∼52°N, indicating the onset of late Pleistocene-like sources by MIS G2 (Bailey et al., 2013), and increase in North American-sourced aeolian dust at 41°N (Naafs et al., 2012) all signal the expansion of continental ice on circum-North Atlantic landmasses during cold stages from MIS G6 (Figures 9a and 9b). While this evidence clearly records a step-wise increase in the extent of North American glaciation from this time, mid-latitude Laurentide Ice Sheet extents were likely not achieved until MIS 96, 98 and 100, as implied from IRD deposition at Site U1313 (Bolton et al., 2010, 2018; Lang et al., 2016) and cosmogenic dating of glacial tills (Balco & Rovey, 2010). Thus, this change in the sensitivity of Dove Basin lithology, which is likely a convolved influence of Antarctic Ice Sheet dynamics, primary productivity, and Southern Ocean Dynamics (Reilly et al., 2021; Sprenk et al., 2013; Weber et al., 2022), appears to be coupled with the significant expansion of marine-based Northern Hemisphere Ice Sheets during these three late Pliocene glacial intervals—plausibly establishing an interhemispheric connection between extensive marine-based ice sheets in both the Northern and Southern Hemisphere via sea level variations (e.g., Denton & Hughes, 1983). However, it is also significant that this mechanism does not require the mid-latitude Laurentide Ice Sheet extents believed to have occurred by MIS 96–100 (Balco & Rovey, 2010; Bolton et al., 2010, 2018; Lang et al., 2016) to establish bipolar ice sheet interactions.

The newly identified transition in Dove Basin strata around the Pliocene-Pleistocene boundary indicates pacing of lithologic variations at obliquity timescales in the early Pleistocene, similar to those observed in the convolved global ice volume and deep-sea temperature benthic $\delta^{18}O$ signal (Figure 10h). Yet, the timing of anomalous events characterized by high accumulation rates and high biogenic silica, tracked through the b* color parameter in interglacials MIS 87, 89, 91, 103, G17, G19, and KM3 (Figures 8b and 9h), indicate Dove Basin lithology must also be sensitive to local radiative forcing because of the systematic occurrence of these extreme interglacial expressions and maxima in the amplitude modulation of precession superimposed on the amplitude modulation of obliquity (Figure 9h). Brief periods of warmth with low ice cover in the Ross Sea were also found to have occurred around the timing of MIS 91, G17, and KM3, although the exact timing of these events are limited by age model resolution (Seidenstein et al., 2024). This sensitivity to the combined influence of the magnitude of variance in both precession and obliquity may be a feature of high latitude environments in both hemispheres during the late Pliocene and early Pleistocene, as seen by the co-occurrence of these high b* intervals, supported

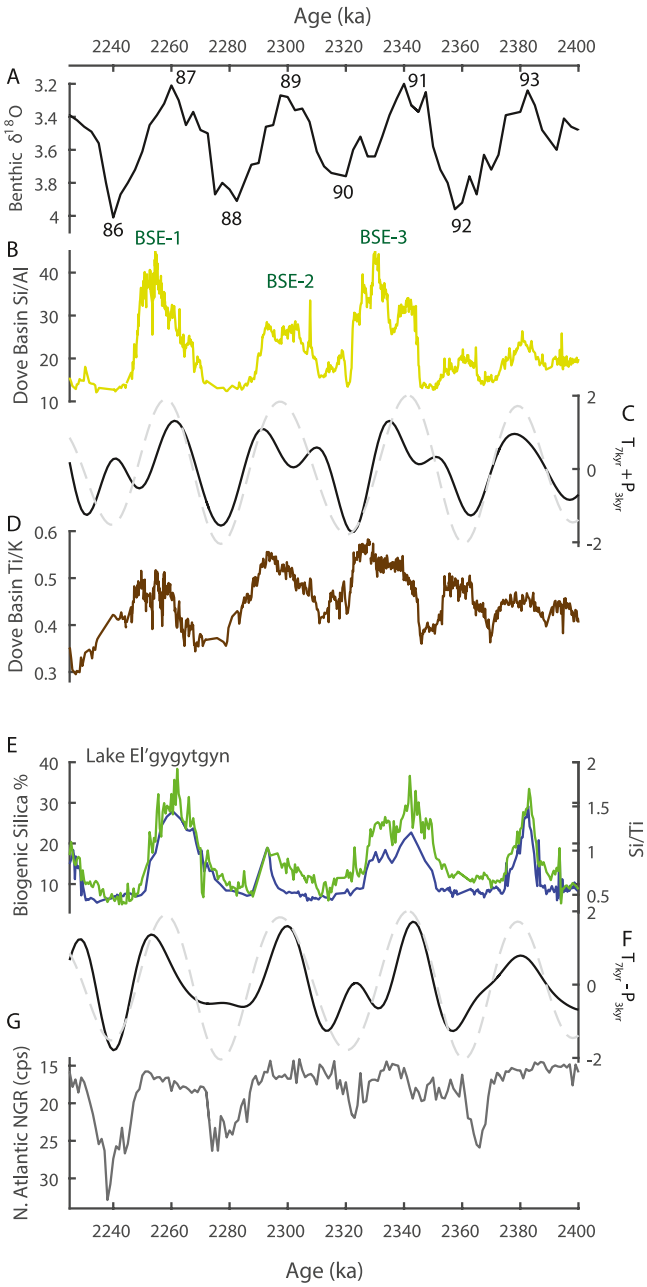

Figure 11. Structure of glacial-interglacial variability during MIS 86-92, characterized by high orbital forcing and high biogenic silica concentrations in the Antarctic Dove Basin and Arctic Lake El'gygytgyn. For a, b, d, e, and g, colors and data as in Figure 9. (c) Normalized Obliquity (7 kyr lag) plus normalized precession (3 kyr lag) (solid line), and normalized obliquity (dashed line). (f) Normalized Obliquity (7 kyr lag) minus normalized precession (3 kyr lag) (solid line), and normalized obliquity (dashed line).

by XRF Si/Al observations, with "super-interglacial" lithology described in the Arctic Lake El'gygytgyn (Brigham-Grette et al., 2013; Melles et al., 2012) (Figures 9f–9k).

Raymo et al. (2006) hypothesized that both Northern and Southern Hemisphere Ice Sheets were likely still sensitive to local precession-paced summer insolation forcing in the so-called 41-kyr-world of the early Pleistocene, but that evidence for this influence would be hidden in records of global ice volume as the anti-phased hemispheric insolation signals would cancel through destructive interference (see also Morée et al., 2021; Reilly et al., 2021; Shakun et al., 2016; Yan et al., 2023). In this hypothesis, the rise in overall variance and ∼100 kyr power in benthic $\delta^{18}O$ data recording through the mid-Pleistocene Transition (Clark et al., 2006; Lisiecki & Raymo, 2007; Pisias & Moore, 1981) is associated with the expansion of marine-based sectors of the Antarctic Ice Sheet driving a change in the dynamics of Northern Hemisphere Ice Sheets and sea level (Raymo et al., 2006). While there is certainly evidence for marine-terminating Antarctic ice prior to the mid-Pleistocene Transition, Jasper et al. (2024) recently demonstrated that the IRD flux to the Dove Basin implies progressive expansion of calving margins over the course of the Pleistocene with notable increases indicating expansion of marine-terminating Antarctic ice margins near the end of our study interval at ∼1.8 and also at 0.43 Ma. Evidence for less extensive marine-terminating ice margins in the early Pleistocene has also been documented in other sectors of Antarctica. Along the western Antarctic Peninsula, Cowan et al. (2008) argue for a lesser degree of continental shelf edge glaciation during glacial intervals prior to 1.35 Ma based on IRD flux and sand microtextures. In the Ross Sea, the ANDRILL AND-1B displays a cooling step across the Plio-Pleistocene transition, but also several thick diatomite intervals up to ∼2 Ma, interbedded with diamictites, with the most recent diatomite deposition around ∼1 Ma, indicating periods of less extensive ice (McKay et al., 2012a, 2012b; Naish et al., 2009).

Given the clear evidence from lithology of the sensitivity of Dove Basin to periods with high amplitude of precession in the early Pleistocene, and thus the highest summer insolation (Figures 8 and 9), it is plausible that although Dove Basin lithology is paced by obliquity, local radiative forcing or thresholds in local radiative forcing are also important for controlling the expression of interglacial intervals. For comparison, in the Northern North Atlantic over the last 1.7 Ma where a lithologic indicator for glaciation (IRD) can be directly intercalibrated with benthic $\delta^{18}O$, Barker et al. (2022) demonstrated that while glacial-interglacial changes in IRD had a 41 kyr pacing due to the sensitivity of glacial inceptions to obliquity changes, IRD-defined glacial terminations were consistently linked to northern hemisphere peak summer insolation maxima—a signal that cannot be detected using traditional frequency analysis like we present in Figure 10h. While it remains challenging to analyze our record at the timescale relevant to assess the phasing of glacial terminations due to the 5 kyr and potentially greater age model uncertainty of our indirect calibration to benthic $\delta^{18}O$ through RPI stratigraphy, we consider the C2r.2r BSE intervals in interglacials 87, 89, and 91 particularly strong evidence for the combined influence of obliquity and precession on Dove Basin lithology within the early Pleistocene. Moreover, considering the obliquity paced variations, we observe that the shapes of the BSE intervals are consistent with a Southern Hemisphere summer insolation phase (i.e., obliquity + precession) in the Dove Basin, while the equivalent intervals at Arctic Lake El'gygytgyn are more consistent with a Northern Hemisphere summer insolation phase (i.e., obliquity–precession) (Figure 11). This is perhaps most clear in the structure of BSE-3, placed in MIS 91, which shows a delayed peak near the end of the biogenic silica

enriched interval at Site U1537 and an early peak in the biogenic silica interval associated with MIS 91 at Lake El'gygygytn, as would be predicted if each site was responding to changes in local summer insolation forcing (Figure 11).

5. Conclusion

We present and assess an RPI chronology for the late Pliocene and early Pleistocene for Dove Basin Sites U1536 and U1537, located in the Scotia Sea's Iceberg Alley, north of Antarctica's Weddell Sea embayment, spanning 1.75–3.14 Ma. Detailed u-channel analysis of the NRM of Site U1537 sediments, supplemented by rock magnetic analyses, display a well-defined magnetization hosted by a detrital magnetite dominated magnetic mineral assemblage (Figures 3–7). A bimodal distribution of inclination values has modes that are consistent with predictions for a GAD field. Distributions of inclination values for both normal and reverse polarity are significantly steeper than that of the modern field, indicating that SAA-like features are not representative of the long-term geomagnetic field or are too short to be detected (Figure 4). In addition to the magnetic reversals that define the start and end of the polarity chrons, four geomagnetic instabilities have ages and MIS stratigraphic positions of 1.967 Ma (MIS 74/75), 2.247 Ma (MIS 86/87), 2.527/2.538 Ma (early MIS 100), and 2.625 Ma (MIS G1) (Table 1; Figures 3 and 6; Figure S18 in Supporting Information S1). These stratigraphic positions are consistent with excursions that have previously been documented in Northern Hemisphere sedimentary archives (Blake-Mizen et al., 2019; Channell et al., 2002; Nowaczyk, Haltia, et al., 2013; Ohno et al., 2012) and, in the case of the MIS 86/87 and MIS 100 excursions, may be related to radioisotopically dated lava flows with transitional directions that have been previously named the Reunion and Halawa excursions (Asefaw et al., 2021; Channell et al., 2020; Herrero-Bervera et al., 2007; Singer et al., 2014).

Our RPI chronology is generated through correlation to an RPI template developed using records from the North Atlantic that are intercalibrated with benthic $\delta^{18}O$ and a proxy for terrigenous input to the subpolar North Atlantic (NGR) that captures the timing of the southward expansion of marine-terminating margins of the fringing North Atlantic ice sheets just prior to the Pliocene-Pleistocene transition (Figures 1, 2 and 7). We estimate age uncertainty that averages ±5.3 kyr between 1.75 and 3.14 Ma, with uncertainties as high as ±10–15 kyr around 2.15–2.25 Ma and 2.75 Ma where we use a lower density of correlation tie points (Figure 8). At Site U1537, both long period and orbital scale trends in accumulation rate have a close relationship with physical properties that track the relative proportion of biogenic versus terrigenous sediments, implying that higher accumulation rates are related to intervals of increased biogenic silica sediment input. Like the physical lithology (e.g., Reilly et al., 2021), accumulation rates for the last 3.3 Ma appear to be sensitive to long orbital periods associated with amplitude modulation (Figure 8). Three intervals with anomalously high biogenic silica content and high accumulation rates (the C2r.2r BSE intervals) are associated with MIS 87, 89, and 91, which occurred during the periods of the highest amplitude modulation of precession superimposed on the amplitude modulation of obliquity of our study interval (Figures 8 and 9). Prior to 1 Ma, similar intervals are also documented during other times of high variance in both precession and obliquity during MIS 37, 47, 49, 103, G17, G19, and KM3. Due to the similarity in the timing of many of these events to the "super-interglacial" lithofacies described in the Russian Arctic Lake El'gygytgyn (Brigham-Grette et al., 2013; Melles et al., 2012), it is likely that these late Pliocene and early Pleistocene intervals of heightened interglacial expression are more probable during periods with greater variance in both obliquity and precession orbital forcing in both the Northern and Southern Hemisphere high latitudes (Figure 9).

While there are differences in the Dove Basin logarithm of κ, Dove Basin GRA, and benthic $\delta^{18}O$, the three signals share nearly identical frequency characteristics in the earliest Pleistocene (Figures 9 and 10). This is contrasted to the latest Pliocene, prior to ∼2.8 Ma, when the Dove Basin lithology proxies show significantly higher variance at the precession frequency versus the obliquity frequency when compared to benthic $\delta^{18}O$ (Figure 10). The timing of this transition between 2.6 Ma and 2.8 closely matches the onset of increased terrigenous and IRD input to the subpolar North Atlantic during MIS G6 (2.73 Ma) and the first subpolar North Atlantic IRD provenance evidence for a significant southward expansion of the Laurentide Ice Sheet marine-terminating margins during MIS G2 (∼2.64 Ma) (Bailey et al., 2013), indicating Antarctic and Northern Hemisphere interaction following the establishment of significant marine-based ice sheets in both Hemispheres (Figure 9). Although we note that this does not seem to require the more mid-latitude ice extents interpreted to have occurred during MIS 96, 98, and 100 (Balco & Rovey, 2010; Bolton et al., 2010, 2018; Lang et al., 2016). Following this transition, despite obliquity playing a dominant role in the pacing of Dove Basin lithologic changes, the imprint of precession is clear in the timing of the anomalous biogenic silica rich and high

sedimentation rate intervals. Thus, while Dove Basin lithology is a convolved signal of Antarctic Ice Sheet and Southern Ocean dynamics, these observations implicate a combined influence of obliquity and local peak summer insolation forcing for regional Antarctic climate. A more complete understanding of how Scotia Sea lithology reflects Antarctic ice volume changes and Southern Ocean evolution will need to be addressed through continued community efforts to characterize sediment transport dynamics, provenance, and paleoceanographic proxies.

Given the close relationship between Scotia Sea κ and dust flux to the EPICA Dome C ice core for the last 800 kyr (Weber et al., 2022), this RPI-based age model grounded in correlation to a benthic $\delta^{18}O$ calibrated template may prove to be a useful comparison for ongoing efforts to recover Pliocene and early Pleistocene ice from Antarctica that may only capture brief windows of time. The co-registered record of climate signals, magnetic reversals, magnetic excursions, and RPI in the Dove Basin provide an opportunity to identify more unique ice core correlations through comparison to combined dust flux, ^{10}Be, and potentially other climate proxies. The demonstrated value of regions like the Dove Basin to study ice, ocean, and geomagnetic variations, emphasizes the need for further scientific drilling in the Scotia Sea and Weddell Sea to extend records like these with the recovery and resolution to examine orbital scale variation through the entire Pliocene, and even in older intervals.

Conflict of Interest

The authors declare no conflicts of interest relevant to this study.

Data Availability Statement

U-channel magnetic data are archived with the Magnetics Information Consortium (MagIC) database (Reilly et al., 2026). Rock magnetic data files are available through the Zenodo Repository (Reilly et al., 2025a). Shipboard magnetic data are archived with the MagIC database (Weber et al., 2019), Zenodo Database (Reilly, Tauxe, et al., 2020; Weber et al., 2021f, 2021g), and the IODP LIMS Database (https://web.iodp.tamu.edu/LORE/). Shipboard physical property data and post-cruise XRF data are also available through Zenodo (Weber et al., 2021h, 2021i, 2021j, 2021k) and the IODP LIMS Database. CT data are available through the Zenodo Repository (Reilly, 2024). Supporting tables and organized stratigraphic data are archived in the Zenodo Repository (Reilly et al., 2025b).

Acknowledgments

The authors are grateful to the captain, crew, IODP staff, and science party that made IODP Expedition 382 successful. All samples and data were provided by IODP. We thank H. Kuhlmann, A. Wuelbers and the Bremen Core Repository for help with sampling; J. Hertzberg and the Gulf Coast Repository for help with XRF scanning; V. Stanley, J. Wiest, and the OSU Marine and Geology Repository for help with CT scanning; A. Mix, C. Fritz, and B. Freiberg for building the wooden box to hold the u-channels during CT scanning; and K. Solada, D. Dywer, L. Monito and the OSU P-Mag Lab for help with magnetic measurements and the magnetic susceptibility track. Part of this work was performed as a Visiting Fellow at the Institute for Rock Magnetism (IRM) at the University of Minnesota. The IRM is a US National Multi-user Facility supported through the Instrumentation and Facilities program of the National Science Foundation, Earth Sciences Division, and by funding from the University of Minnesota. US participants on Expedition 382 acknowledge support from the US Science Support Program and Columbia University (National Science Foundation (NSF) award OCE 1450528). This work was made possible through a collaborative US NSF Office of Polar Programs award to B. Reilly and L. Tauxe (2114777, 2302832), S. Brachfeld (2114764), S. Hemming and I. Bailey (2114763), T. Williams (2114768), S. O'Connell (2114769), and J. Warnock (2114786). We thank two reviewers for their constructive and thoughtful comments on our manuscript.

References

Anderson, J. B., & Andrews, J. T. (1999). Radiocarbon constraints on ice sheet advance and retreat in the Weddell Sea, Antarctica. *Geology*, *27*(2), 179–182. https://doi.org/10.1130/0091-7613(1999)027<0179:RCOISA>2.3.CO;2

Asefaw, H., Tauxe, L., Koppers, A. A. P., & Staudigel, H. (2021). Four-dimensional paleomagnetic dataset: Plio-Pleistocene paleodirection and paleointensity results from the Erebus Volcanic Province, Antarctica. *Journal of Geophysical Research: Solid Earth*, *126*(2), e2020JB020834. https://doi.org/10.1029/2020JB020834

Bailey, I., Bolton, C. T., DeConto, R. M., Pollard, D., Schiebel, R., & Wilson, P. A. (2010). A low threshold for North Atlantic ice rafting from "low-slung slippery" late Pliocene ice sheets. *Paleoceanography*, *25*(1). https://doi.org/10.1029/2009PA001736

Bailey, I., Hemming, S., Reilly, B. T., Rollinson, G., Williams, T., Weber, M. E., et al. (2022). Episodes of early Pleistocene West Antarctic Ice Sheet retreat recorded by Iceberg Alley sediments. *Paleoceanography and Paleoclimatology*, *37*(7), e2022PA004433. https://doi.org/10.1029/2022PA004433

Bailey, I., Hole, G. M., Foster, G. L., Wilson, P. A., Storey, C. D., Trueman, C. N., & Raymo, M. E. (2013). An alternative suggestion for the Pliocene onset of major northern hemisphere glaciation based on the geochemical provenance of North Atlantic Ocean ice-rafted debris. *Quaternary Science Reviews*, *75*, 181–194. https://doi.org/10.1016/j.quascirev.2013.06.004

Balbas, A., Koppers, A. A. P., Kent, D. V., Konrad, K., & Clark, P. U. (2016). Identification of the short-lived Santa Rosa geomagnetic excursion in lavas on Floreana Island (Galapagos) by $^{40}Ar/^{39}Ar$ geochronology. *Geology*, *44*(5), 359–362. https://doi.org/10.1130/G37569.1

Balco, G., & Rovey, C. W. (2010). Absolute chronology for major Pleistocene advances of the Laurentide Ice Sheet. *Geology*, *38*(9), 795–798. https://doi.org/10.1130/G30946.1

Banerjee, S. K., King, J., & Marvin, J. (1981). A rapid method for magnetic granulometry with applications to environmental studies. *Geophysical Research Letters*, *8*(4), 333–336. https://doi.org/10.1029/GL008i004p00333

Barker, S., Starr, A., van der Lubbe, J., Doughty, A., Knorr, G., Conn, S., et al. (2022). Persistent influence of precession on northern ice sheet variability since the early Pleistocene. *Science*, *376*(6596), 961–967. https://doi.org/10.1126/science.abm4033

Batchelor, C. L., Margold, M., Krapp, M., Murton, D. K., Dalton, A. S., Gibbard, P. L., et al. (2019). The configuration of northern hemisphere ice sheets through the Quaternary. *Nature Communications*, *10*, 1–10. https://doi.org/10.1038/s41467-019-11601-2

Bentley, M. J., Ó Cofaigh, C., Anderson, J. B., Conway, H., Davies, B., Graham, A. G. C., et al. (2014). A community-based geological reconstruction of Antarctic Ice Sheet deglaciation since the Last Glacial Maximum. *Quaternary Science Reviews, Reconstruction of Antarctic Ice Sheet Deglaciation (RAISED)*, *100*, 1–9. https://doi.org/10.1016/j.quascirev.2014.06.025

Bertoa del Llano, M., Strelin, J. A., Calabozo, F. M., Kaplan, M. R., Hemming, S. R., & Cai, Y. (2021). Late Miocene to Plio-Pleistocene volcanic and paleoenvironmental history of the Cerro Domo and Ventisqueros Mesa area, northwest James Ross Island, northern Antarctic Peninsula. *Journal of Volcanology and Geothermal Research*, *417*, 107313. https://doi.org/10.1016/j.jvolgeores.2021.107313

Bilardello, D., & Jackson, M. (2013). What do the Mumpsies do? *The IRM Quarterly*, *23*.

Blake-Mizen, K., Hatfield, R. G., Stoner, J. S., Carlson, A. E., Xuan, C., Walczak, M., et al. (2019). Southern Greenland glaciation and Western Boundary Undercurrent evolution recorded on Eirik Drift during the late Pliocene intensification of Northern Hemisphere glaciation. *Quaternary Science Reviews*, *209*, 40–51. https://doi.org/10.1016/j.quascirev.2019.01.015

Bolton, C. T., Bailey, I., Friedrich, O., Tachikawa, K., de Garidel-Thoron, T., Vidal, L., et al. (2018). North Atlantic midlatitude surface-circulation changes through the Plio-Pleistocene intensification of Northern Hemisphere glaciation. *Paleoceanography and Paleoclimatology*, *33*(11), 1186–1205. https://doi.org/10.1029/2018PA003412

Bolton, C. T., Wilson, P. A., Bailey, I., Friedrich, O., Beer, C. J., Becker, J., et al. (2010). Millennial-scale climate variability in the subpolar North Atlantic Ocean during the late Pliocene. *Paleoceanography*, *25*(4). https://doi.org/10.1029/2010PA001951

Brachfeld, S., Domack, E., Kissel, C., Laj, C., Leventer, A., Ishman, S., et al. (2003). Holocene history of the Larsen-A ice shelf constrained by geomagnetic paleointensity dating. *Geology*, *31*(1), 749–752. https://doi.org/10.1130/g19643.1

Brachfeld, S. A., & Banerjee, S. K. (2000). A new high-resolution geomagnetic relative paleointensity record for the North American Holocene: A comparison of sedimentary and absolute intensity data. *Journal of Geophysical Research*, *105*(B1), 821–834. https://doi.org/10.1029/1999JB900365

Brigham-Grette, J., Melles, M., Minyuk, P., Andreev, A., Tarasov, P., DeConto, R., et al. (2013). Pliocene warmth, polar amplification, and stepped Pleistocene cooling recorded in NE Arctic Russia. *Science*, *340*(6139), 1421–1427. https://doi.org/10.1126/science.1233137

Brown, M. C., Holme, R., & Bargery, A. (2007). Exploring the influence of the non-dipole field on magnetic records for field reversals and excursions. *Geophysical Journal International*, *168*(2), 541–550. https://doi.org/10.1111/j.1365-246X.2006.03234.x

Cande, S. C., & Kent, D. V. (1992). A new geomagnetic polarity time scale for the late Cretaceous and Cenozoic. *Journal of Geophysical Research*, *97*(B10), 13917–13951. https://doi.org/10.1029/92jb01202

Chang, L., Roberts, A. P., Heslop, D., Hayashida, A., Li, J., Zhao, X., et al. (2016). Widespread occurrence of silicate-hosted magnetic mineral inclusions in marine sediments and their contribution to paleomagnetic recording. *Journal of Geophysical Research: Solid Earth*, *121*(12), JB013109-8431. https://doi.org/10.1002/2016JB013109

Channell, J. E. T. (1999). Geomagnetic paleointensity and directional secular variation at Ocean Drilling Program (ODP) Site 984 (Bjorn Drift) since 500 ka: Comparisons with ODP site 983 (Gardar Drift). *Journal of Geophysical Research*, *104*(B10), 22937–22951. https://doi.org/10.1029/1999JB900223

Channell, J. E. T. (2017). Mid-Brunhes magnetic excursions in marine isotope stages 9, 13, 14, and 15 (286, 495, 540, and 590 ka) at North Atlantic IODP Sites U1302/3, U1305 and U1306. *Geochemistry, Geophysics, Geosystems*, *18*(2), 473–487. https://doi.org/10.1002/2016GC006626

Channell, J. E. T., & Guyodo, Y. (2004). The Matuyama Chronozone at ODP Site 982 (Rockall Bank): Evidence for decimeter-scale magnetization lock-in depths. In J. E. T. Channell, D. V. Kent, W. Lowrie, & J. G. Meert (Eds.), *Timescales of the paleomagnetic field* (pp. 205–219). American Geophysical Union.

Channell, J. E. T., Hodell, D. A., & Curtis, J. H. (2016). Relative paleointensity (RPI) and oxygen isotope stratigraphy at IODP Site U1308: North Atlantic RPI stack for 1.2–2.2 Ma (NARPI-2200) and age of the Olduvai Subchron. *Quaternary Science Reviews*, *131*, 1–19. https://doi.org/10.1016/j.quascirev.2015.10.011

Channell, J. E. T., Hodell, D. A., & Lehman, B. (1997). Relative geomagnetic paleointensity and $\delta^{18}O$ at ODP Site 983 (Gardar Drift, North Atlantic) since 350 ka. *Earth and Planetary Science Letters*, *153*(1–2), 103–118. https://doi.org/10.1016/S0012-821X(97)00164-7

Channell, J. E. T., Hodell, D. A., Xuan, C., Mazaud, A., & Stoner, J. S. (2008). Age calibrated relative paleointensity for the last 1.5 Myr at IODP Site U1308 (North Atlantic). *Earth and Planetary Science Letters*, *274*(1–2), 59–71. https://doi.org/10.1016/j.epsl.2008.07.005

Channell, J. E. T., Kanamatsu, T., Sato, T., Stein, R., Alvarez Zarikian, C. A., & Malone, M. J. (2006). The Expedition 303/306 scientists. In *Proceedings of the IODP, 303/306*. Integrated Ocean Drilling Program.

Channell, J. E. T., & Kleiven, H. F. (2000). Geomagnetic palaeointensities and astrochronological ages for the Matuyama–Brunhes boundary and the boundaries of the Jaramillo Subchron: Palaeomagnetic and oxygen isotope records from ODP Site 983. *Philosophical Transactions of the Royal Society of London, Series A: Mathematical, Physical and Engineering Sciences*, *358*(1768), 1027–1047. https://doi.org/10.1098/rsta.2000.0572

Channell, J. E. T., Labs, J., & Raymo, M. E. (2003). The Réunion subchronozone at ODP Site 981 (Feni Drift, North Atlantic). *Earth and Planetary Science Letters*, *215*(1–2), 1–12. https://doi.org/10.1016/S0012-821X(03)00435-7

Channell, J. E. T., Mazaud, A., Sullivan, P., Turner, S., & Raymo, M. E. (2002). Geomagnetic excursions and paleointensities in the Matuyama Chron at Ocean Drilling Program Sites 983 and 984 (Iceland Basin). *Journal of Geophysical Research*, *107*(B6), EPM 1. https://doi.org/10.1029/2001JB000491

Channell, J. E. T., Singer, B. S., & Jicha, B. R. (2020). Timing of Quaternary geomagnetic reversals and excursions in volcanic and sedimentary archives. *Quaternary Science Reviews*, *228*, 106114. https://doi.org/10.1016/j.quascirev.2019.106114

Channell, J. E. T., Wright, J. D., Mazaud, A., & Stoner, J. S. (2014). Age through tandem correlation of Quaternary relative paleointensity (RPI) and oxygen isotope data at IODP Site U1306 (Eirik drift, SW Greenland). *Quaternary Science Reviews*, *88*, 135–146. https://doi.org/10.1016/j.quascirev.2014.01.022

Channell, J. E. T., Xuan, C., & Hodell, D. A. (2009). Stacking paleointensity and oxygen isotope data for the last 1.5 Myr (PISO-1500). *Earth and Planetary Science Letters*, *283*(1–4), 14–23. https://doi.org/10.1016/j.epsl.2009.03.012

Channell, J. E. T., Xuan, C., Hodell, D. A., Crowhurst, S. J., & Larter, R. D. (2019). Relative paleointensity (RPI) and age control in Quaternary sediment drifts off the Antarctic Peninsula. *Quaternary Science Reviews*, *16*.

Clark, P. U., Archer, D., Pollard, D., Blum, J. D., Rial, J. A., Brovkin, V., et al. (2006). The middle Pleistocene transition: Characteristics, mechanisms, and implications for long-term changes in atmospheric pCO_2. *Quaternary Science Reviews*, *25*(23–24), 3150–3184. https://doi.org/10.1016/j.quascirev.2006.07.008

Clark, R. M. (1985). A FORTRAN program for constrained sequence-slotting based on minimum combined path length. *Computers and Geosciences*, *11*(5), 605–617. https://doi.org/10.1016/0098-3004(85)90089-5

Cowan, E. A., Hillenbrand, C.-D., Hassler, L. E., & Ake, M. T. (2008). Coarse-grained terrigenous sediment deposition on continental rise drifts: A record of Plio-Pleistocene glaciation on the Antarctic Peninsula. *Palaeogeography, Palaeoclimatology, Palaeoecology*, *265*(3–4), 275–291. https://doi.org/10.1016/j.palaeo.2008.03.010

Day, R., Fuller, M., & Schmidt, V. (1977). Hysteresis properties of titanomagnetites, grain size and compositional dependence. *Physics of the Earth and Planetary Interiors*, *13*(4), 260–267. https://doi.org/10.1016/0031-9201(77)90108-x

deMenocal, P. B., Ruddiman, W. F., & Kent, D. V. (1990). Depth of post-depositional remanence acquisition in deep-sea sediments: A case study of the Brunhes-Matuyama reversal and oxygen isotopic stage 19.1. *Earth and Planetary Science Letters*, *99*(1–2), 1–13. https://doi.org/10.1016/0012-821X(90)90066-7

Denton, G. H., & Hughes, T. J. (1983). Milankovitch theory of ice ages: Hypothesis of ice-sheet linkage between regional insolation and global climate. *Quaternary Research*, *20*(2), 125–144. https://doi.org/10.1016/0033-5894(83)90073-X

Di Chiara, A., Satolli, S., Friedman, S. A., Dwyer, D., Acton, G. D., Jones, T. D., et al. (2025). Geomagnetic excursions recorded in North Atlantic IODP Expedition 395C Sites U1555 and U1563. *Geochemistry, Geophysics, Geosystems*, *26*(6), e2025GC012220. https://doi.org/10.1029/2025GC012220

Diekmann, B., Kuhn, G., Rachold, V., Abelmann, A., Brathauer, U., Fütterer, D. K., et al. (2000). Terrigenous sediment supply in the Scotia Sea (Southern Ocean): Response to late Quaternary ice dynamics in Patagonia and on the Antarctic Peninsula. *Palaeogeography, Palaeoclimatology, Palaeoecology*, *162*(3–4), 357–387. https://doi.org/10.1016/S0031-0182(00)00138-3

Egli, R. (2013). VARIFORC: An optimized protocol for calculating non-regular first-order reversal curve (FORC) diagrams. Global and planetary change, magnetic iron minerals in sediments and their relation to geologic processes. *Climate, and the Geomagnetic Field*, *110*, 302–320. https://doi.org/10.1016/j.gloplacha.2013.08.003

Egli, R., Chen, A. P., Winklhofer, M., Kodama, K. P., & Horng, C.-S. (2010). Detection of noninteracting single domain particles using first-order reversal curve diagrams. *Geochemistry, Geophysics, Geosystems*, *11*(1). https://doi.org/10.1029/2009GC002916

Fendrock, M., Condron, A., & McGee, D. (2022). Modeling iceberg longevity and distribution during Heinrich Events. *Paleoceanography and Paleoclimatology*, *37*(6), e2021PA004347. https://doi.org/10.1029/2021PA004347

Fraass, A. J., Wall-Palmer, D., Leckie, R. M., Hatfield, R. G., Burns, S., Le Friant, A., et al. (2017). A revised Plio-Pleistocene age model and paleoceanography of the northeastern Caribbean Sea: IODP Site U1396 off Montserrat, Lesser Antilles. *Stratigraphy*, *13*(3), 183–203. https://doi.org/10.29041/strat.13.3.183-203

Frank, U., & Nowaczyk, N. R. (2008). Mineral magnetic properties of artificial samples systematically mixed from haematite and magnetite. *Geophysical Journal International*, *175*(2), 449–461. https://doi.org/10.1111/j.1365-246X.2008.03821.x

Gradstein, F. M., Ogg, J., Schmitz, M., & Ogg, G. (Eds.) (2012). *The geologic time scale 2012* (1st ed.). Elsevier.

Gradstein, F. M., Ogg, J., Schmitz, M., & Ogg, G. (Eds.) (2020). *Geologic time scale 2020*. Elsevier.

Grant, G. R., Naish, T. R., Dunbar, G. B., Stocchi, P., Kominz, M. A., Kamp, P. J. J., et al. (2019). The amplitude and origin of sea-level variability during the Pliocene Epoch. *Nature*, *574*(7777), 237–241. https://doi.org/10.1038/s41586-019-1619-z

Guyodo, Y., Acton, G. D., Brachfeld, S., & Channell, J. E. T. (2001). A sedimentary paleomagnetic record of the Matuyama Chron from the Western Antarctic Margin (ODP site 1101). *Earth and Planetary Science Letters*, *191*(1–2), 61–74. https://doi.org/10.1016/S0012-821X(01)00402-2

Hagen, C. J., Reilly, B. T., Stoner, J. S., & Creveling, J. R. (2020). Dynamic time warping of palaeomagnetic secular variation data. *Geophysical Journal International*, *221*(1), 706–721. https://doi.org/10.1093/gji/ggaa004

Hallmaier, M., Gutjahr, M., Lippold, J., Hemming, S. R., Gerber, L., Weber, M. E., & Eisenhauer, A. (2025). Authigenic uranium preservation and bottom water oxygenation in the Scotia Sea. *Geochemistry, Geophysics, Geosystems*, *26*(9), e2025GC012415. https://doi.org/10.1029/2025GC012415

Haltia, E. M., & Nowaczyk, N. R. (2014). Magnetostratigraphy of sediments from Lake El'gygytgyn ICDP Site 5011-1: Paleomagnetic age constraints for the longest paleoclimate record from the continental Arctic. *Climate of the Past*, *10*(2), 623–642. https://doi.org/10.5194/cp-10-623-2014

Harrison, C. G. A., & Somayajulu, B. L. K. (1966). Behaviour of the Earth's magnetic field during a reversal. *Nature*, *212*(5067), 1193–1195. https://doi.org/10.1038/2121193a0

Harrison, R. J., & Feinberg, J. M. (2008). FORCinel: An improved algorithm for calculating first-order reversal curve distributions using locally weighted regression smoothing. *Geochemistry, Geophysics, Geosystems*, *9*(5), Q05016. https://doi.org/10.1029/2008GC001987

Harrison, R. J., Muraszko, J., Heslop, D., Lascu, I., Muxworthy, A. R., & Roberts, A. P. (2018). An improved algorithm for unmixing first-order reversal curve diagrams using principal component analysis. *Geochemistry, Geophysics, Geosystems*, *19*(5), 1595–1610. https://doi.org/10.1029/2018GC007511

Hatfield, R. G., Stoner, J. S., & Fraass, A. J. (2021). Relative paleointensity record of integrated Ocean Drilling Program Site U1396 in the Caribbean Sea: Geomagnetic and chronostratigraphic observations in the Pliocene. *Geochemistry, Geophysics, Geosystems*, *22*(7), e2021GC009677. https://doi.org/10.1029/2021GC009677

Hatfield, R. G., Stoner, J. S., Reilly, B. T., Tepley, F. J., Wheeler, B. H., & Housen, B. A. (2017). Grain size dependent magnetic discrimination of Iceland and South Greenland terrestrial sediments in the northern North Atlantic sediment record. *Earth and Planetary Science Letters*, *474*, 474–489. https://doi.org/10.1016/j.epsl.2017.06.042

Hatfield, R. G., Wheeler, B. H., Reilly, B. T., Stoner, J. S., & Housen, B. A. (2019). Particle size specific magnetic properties across the Norwegian-Greenland Seas: Insights into the influence of sediment source and texture on bulk magnetic records. *Geochemistry, Geophysics, Geosystems*, *20*(2), 1004–1025. https://doi.org/10.1029/2018GC007894

Hay, C. C., Creveling, J. R., Hagen, C. J., Maloof, A. C., & Huybers, P. (2019). A library of early Cambrian chemostratigraphic correlations from a reproducible algorithm. *Geology*, *47*(5), 457–460. https://doi.org/10.1130/G46019.1

Hayashi, T., Ohno, M., Acton, G., Guyodo, Y., Evans, H. F., Kanamatsu, T., et al. (2010). Millennial-scale iceberg surges after intensification of Northern Hemisphere glaciation. *Geochemistry, Geophysics, Geosystems*, *11*(9). https://doi.org/10.1029/2010GC003132

Herrero-Bervera, E., Browne, E. J., Valet, J. P., Singer, B. S., & Jicha, B. R. (2007). Cryptochron C2r.2r-1 recorded 2.51 Ma in the Koolau Volcano at Halawa, Oahu, Hawaii, USA: Paleomagnetic and $^{40}Ar/^{39}Ar$ evidence. *Earth and Planetary Science Letters*, *254*(3–4), 256–271. https://doi.org/10.1016/j.epsl.2006.11.023

Hodell, D. A., & Channell, J. E. (2016). Mode transitions in Northern Hemisphere glaciation: Co-evolution of millennial and orbital variability in Quaternary climate. *Climate of the Past*, *12*(9), 1805–1828. https://doi.org/10.5194/cp-12-1805-2016

Hodell, D. A., Channell, J. E. T., Curtis, J. H., Romero, O. E., & Röhl, U. (2008). Onset of "Hudson Strait" Heinrich events in the eastern North Atlantic at the end of the middle Pleistocene transition (~640 ka)? *Paleoceanography*, *23*(4). https://doi.org/10.1029/2008PA001591

Hopkins, B., Xuan, C., Hillenbrand, C.-D., van Peer, T. E., Jin, Y., Frederichs, T., et al. (2024). Evaluation of geomagnetic relative palaeointensity as a chronostratigraphic tool in the Southern Ocean: Refined Plio-/Pleistocene chronology of IODP site U1533 (Amundsen Sea, West Antarctica). *Quaternary Science Reviews*, *325*, 108460. https://doi.org/10.1016/j.quascirev.2023.108460

Horng, C.-S., Lee, M.-Y., Pälike, H., Wei, K.-Y., Liang, W.-T., Iizuka, Y., & Torii, M. (2002). Astronomically calibrated ages for geomagnetic reversals within the Matuyama Chron. *Earth Planets and Space*, *54*, 679–690.

Horng, C.-S., Roberts, A. P., & Liang, W.-T. (2003). A 2.14-Myr astronomically tuned record of relative geomagnetic paleointensity from the western Philippine Sea. *Journal of Geophysical Research*, *108*(B1), 2059. https://doi.org/10.1029/2001JB001698

Hospers, J. (1954). Rock magnetism and polar wandering. *Nature*, *173*(4416), 1183–1184. https://doi.org/10.1038/1731183a0

Hounsfield, G. N. (1973). Computerized transverse axial scanning (tomography): Part 1. Description of system. *BJR*, *46*(552), 1016–1022. https://doi.org/10.1259/0007-1285-46-552-1016

Jackson, M., & Solheid, P. (2010). On the quantitative analysis and evaluation of magnetic hysteresis data. *Geochemistry, Geophysics, Geosystems*, *11*(4). https://doi.org/10.1029/2009GC002932

Jakob, K. A., Wilson, P. A., Pross, J., Ezard, T. H. G., Fiebig, J., Repschläger, J., & Friedrich, O. (2020). A new sea-level record for the Neogene/Quaternary boundary reveals transition to a more stable East Antarctic ice sheet. *PNAS*, *117*(49), 30980–30987. https://doi.org/10.1073/pnas.2004209117

Jansen, E., Fronval, T., Rack, F., & Channell, J. E. T. (2000). Pliocene-Pleistocene ice rafting history and cyclicity in the Nordic Seas during the last 3.5 myr. *Paleoceanography*, *15*(6), 709–721. https://doi.org/10.1029/1999PA000435

Jasper, C. E., Dyer, B., Reilly, B. T., Williams, T., Hemming, S., & Raymo, M. E. (2024). A 3.3-million-year record of Antarctic iceberg rafted debris and ice sheet evolution quantified by machine learning. *Paleoceanography and Paleoclimatology*, *39*(9), e2024PA004897. https://doi.org/10.1029/2024PA004897

King, J., Banerjee, S. K., Marvin, J., & Özdemir, Ö. (1982). A comparison of different magnetic methods for determining the relative grain size of magnetite in natural materials: Some results from lake sediments. *Earth and Planetary Science Letters*, *59*(2), 404–419. https://doi.org/10.1016/0012-821X(82)90142-X

Kirschvink, J. L. (1980). The least-squares line and plane and the analysis of palaeomagnetic data. *Geophysical Journal of the Royal Astronomical Society*, *62*(3), 699–718. https://doi.org/10.1111/j.1365-246x.1980.tb02601.x

Kleiven, H., Jansen, E., Fronval, T., & Smith, T. M. (2002). Intensification of Northern Hemisphere glaciations in the circum Atlantic region (3.5–2.4 Ma) – Ice-rafted detritus evidence. *Palaeogeography, Palaeoclimatology, Palaeoecology*, *184*(3–4), 213–223. https://doi.org/10.1016/S0031-0182(01)00407-2

Knudsen, M. F., Holm, P. M., & Abrahamsen, N. (2009). Paleomagnetic results from a reconnaissance study of Santiago (Cape Verde Islands): Identification of cryptochron C2r.2r-1. *Physics of the Earth and Planetary Interiors*, *173*(3–4), 279–289. https://doi.org/10.1016/j.pepi.2009.01.009

Kok, Y. S., & Tauxe, L. (1999). A relative geomagnetic paleointensity stack from Ontong-Java Plateau sediments for the Matuyama. *Journal of Geophysical Research*, *104*(B11), 25401–25413. https://doi.org/10.1029/1999JB900186

Laj, C., & Channell, J. E. T. (2007). Geomagnetic excursions. In *Treatise on Geophysics* (Vol. 5).

Lang, D. C., Bailey, I., Wilson, P. A., Chalk, T. B., Foster, G. L., & Gutjahr, M. (2016). Incursions of southern-sourced water into the deep North Atlantic during late Pliocene glacial intensification. *Nature Geoscience*, *9*(5), 375–379. https://doi.org/10.1038/ngeo2688

Lascu, I., Einsle, J. F., Ball, M. R., & Harrison, R. J. (2018). The vortex state in geologic materials: A micromagnetic perspective. *Journal of Geophysical Research: Solid Earth*, *123*(9), 7285–7304. https://doi.org/10.1029/2018JB015909

Laskar, J., Robutel, P., Joutel, F., Gastineau, M., Correia, A. C. M., & Levrard, B. (2004). A long-term numerical solution for the insolation quantities of the Earth. *A&A*, *428*(1), 261–285. https://doi.org/10.1051/0004-6361:20041335

Liautaud, P. R., Hodell, D. A., & Huybers, P. J. (2020). Detection of significant climatic precession variability in early Pleistocene glacial cycles. *Earth and Planetary Science Letters*, *536*, 116137. https://doi.org/10.1016/j.epsl.2020.116137

Lisiecki, L. E., & Lisiecki, P. A. (2002). Application of dynamic programming to the correlation of paleoclimate records. *Paleoceanography*, *17*(4), 1-1–1–12. https://doi.org/10.1029/2001PA000733

Lisiecki, L. E., & Raymo, M. E. (2005). A Pliocene-Pleistocene stack of 57 globally distributed benthic $\delta^{18}O$ records. *Paleoceanography*, *20*(1), PA1003. https://doi.org/10.1029/2004PA001071

Lisiecki, L. E., & Raymo, M. E. (2007). Plio–Pleistocene climate evolution: Trends and transitions in glacial cycle dynamics. *Quaternary Science Reviews*, *26*(1–2), 56–69. https://doi.org/10.1016/j.quascirev.2006.09.005

Lougheed, B., & Obrochta, S. (2019). A rapid, deterministic age-depth modeling routine for geological sequences with inherent depth uncertainty. *Paleoceanography and Paleoclimatology*, *34*(1), 122–133. https://doi.org/10.1029/2018PA003457

Lourens, L. J., Antonarakou, A., Hilgen, F. J., Van Hoof, A. A. M., Vergnaud-Grazzini, C., & Zachariasse, W. J. (1996). Evaluation of the Plio-Pleistocene astronomical timescale. *Paleoceanography*, *11*(4), 391–413. https://doi.org/10.1029/96pa01125

Maher, B. A. (1988). Magnetic properties of some synthetic sub-micron magnetites. *Geophysical Journal International*, *94*(1), 83–96. https://doi.org/10.1111/j.1365-246X.1988.tb03429.x

Mazaud, A. (2006). A first-order correction to minimize environmental influence in sedimentary records of relative paleointensity of the geomagnetic field. *Geochemistry, Geophysics, Geosystems*, *7*, Q07002. https://doi.org/10.1029/2006GC001257

McKay, R., Naish, T., Carter, L., Riesselman, C., Dunbar, R., Sjunneskog, C., et al. (2012). Antarctic and Southern Ocean influences on late Pliocene global cooling. *PNAS*, *109*(17), 6423–6428. https://doi.org/10.1073/pnas.1112248109

McKay, R., Naish, T., Powell, R., Barrett, P., Scherer, R., Talarico, F., et al. (2012). Pleistocene variability of Antarctic Ice Sheet extent in the Ross Embayment. *Quaternary Science Reviews*, *34*, 93–112. https://doi.org/10.1016/j.quascirev.2011.12.012

Mead, G. A., Tauxe, L., & LaBrecque, J. L. (1986). Oligocene paleoceanography of the South Atlantic: Paleoclimatic implications of sediment accumulation rates and magnetic susceptibility measurements. *Paleoceanography*, *1*(3), 273–284. https://doi.org/10.1029/PA001i003p00273

Melles, M., Brigham-Grette, J., Minyuk, P. S., Nowaczyk, N. R., Wennrich, V., DeConto, R. M., et al. (2012). 2.8 million years of Arctic climate change from Lake El'gygytgyn, NE Russia. *Science*, 1222135.

Morée, A. L., Sun, T., Bretones, A., Straume, E. O., Nisancioglu, K., & Gebbie, G. (2021). Cancellation of the precessional cycle in $\delta^{18}O$ records during the early Pleistocene. *Geophysical Research Letters*, *48*, e2020GL090035. https://doi.org/10.1029/2020GL090035

Moskowitz, B. M., Frankel, R. B., & Bazylinski, D. A. (1993). Rock magnetic criteria for the detection of biogenic magnetite. *Earth and Planetary Science Letters*, *120*(3–4), 283–300. https://doi.org/10.1016/0012-821X(93)90245-5

Naafs, B. D. A., Hefter, J., Acton, G., Haug, G. H., Martínez-Garcia, A., Pancost, R., & Stein, R. (2012). Strengthening of North American dust sources during the late Pliocene (2.7Ma). *Earth and Planetary Science Letters*, *317–318*, 8–19. https://doi.org/10.1016/j.epsl.2011.11.026

Naish, T., Powell, R., Levy, R., Wilson, G., Scherer, R., Talarico, F., et al. (2009). Obliquity-paced Pliocene West Antarctic ice sheet oscillations. *Nature*, *458*(7236), 322–328. https://doi.org/10.1038/nature07867

Nowaczyk, N., Frank, U., Kind, J., & Arz, H. W. (2013). A high-resolution paleointensity stack of the past 14 to 68 ka from Black Sea sediments. *Earth and Planetary Science Letters*, *384*, 1–16. https://doi.org/10.1016/j.epsl.2013.09.028

Nowaczyk, N., Haltia, E. M., Ulbricht, D., Wennrich, V., Sauerbrey, M. A., & RosÃ, P. (2013). Chronology of Lake El'gygytgyn sediments—A combined magnetostratigraphic, palaeoclimatic and orbital tuning study based on multi-parameter analyses. *Climate of the Past*, *9*(6), 2413–2432. https://doi.org/10.5194/cp-9-2413-2013

Oda, H., & Xuan, C. (2014). Deconvolution of continuous paleomagnetic data from pass-through magnetometer: A new algorithm to restore geomagnetic and environmental information based on realistic optimization. *Geochemistry, Geophysics, Geosystems*, *15*(10), 3907–3924. https://doi.org/10.1002/2014GC005513

Ohno, M., Hayashi, T., Komatsu, F., Murakami, F., Zhao, M., Guyodo, Y., et al. (2012). A detailed paleomagnetic record between 2.1 and 2.75 Ma at IODP Site U1314 in the North Atlantic: Geomagnetic excursions and the Gauss-Matuyama transition. *Geochemistry, Geophysics, Geosystems*, *13*(5). https://doi.org/10.1029/2012GC004080

Opdyke, N. D., & Channell, J. E. T. (1996). *Magnetic stratigraphy, international geophyics series*. Academic Press.

Özdemir, Ö., Dunlop, D. J., & Moskowitz, B. M. (1993). The effect of oxidation on the Verwey transition in magnetite. *Geophysical Research Letters*, *20*, 1671–1674. https://doi.org/10.1029/93GL01483

Patterson, M. O., McKay, R., Naish, T., Escutia, C., Jimenez-Espejo, F. J., Raymo, M. E., et al. (2014). Orbital forcing of the East Antarctic Ice Sheet during the Pliocene and early Pleistocene. *Nature Geoscience*, *7*(11), 841–847. https://doi.org/10.1038/ngeo2273

Pérez, L. F., Martos, Y. M., García, M., Weber, M. E., Raymo, M. E., Williams, T., et al. (2021). Miocene to present oceanographic variability in the Scotia Sea and Antarctic ice sheets dynamics: Insight from revised seismic-stratigraphy following IODP Expedition 382. *Earth and Planetary Science Letters*, *553*, 116657. https://doi.org/10.1016/j.epsl.2020.116657

Pike, C. R., Roberts, A. P., & Verosub, K. L. (1999). Characterizing interactions in fine magnetic particle systems using first order reversal curves. *Journal of Applied Physics*, *85*(9), 6660–6667. https://doi.org/10.1063/1.370176

Pisias, N. G., & Moore, T. C., Jr. (1981). The evolution of Pleistocene climate: A time series approach. *Earth and Planetary Science Letters*, *52*(2), 450–458. https://doi.org/10.1016/0012-821x(81)90197-7

Pugh, R. S., McCave, I. N., Hillenbrand, C.-D., & Kuhn, G. (2009). Circum-Antarctic age modelling of Quaternary marine cores under the Antarctic Circumpolar Current: Ice-core dust–magnetic correlation. *Earth and Planetary Science Letters*, *284*(1–2), 113–123. https://doi.org/10.1016/j.epsl.2009.04.016

Rackow, T., Wesche, C., Timmermann, R., Hellmer, H. H., Juricke, S., & Jung, T. (2017). A simulation of small to giant Antarctic iceberg evolution: Differential impact on climatology estimates. *Journal of Geophysical Research: Oceans*, *122*(4), 3170–3190. https://doi.org/10.1002/2016JC012513

Raymo, M. E., Lisiecki, L. E., & Nisancioglu, K. H. (2006). Plio-Pleistocene ice volume, Antarctic climate, and the global $\delta^{18}O$ record. *Science*, *313*(5786), 492–495. https://doi.org/10.1126/science.1123296

Raymo, M. E., Ruddiman, W. F., Backman, J., Clement, B. M., & Martinson, D. G. (1989). Late Pliocene variation in northern hemisphere ice sheets and North Atlantic deep water circulation. *Paleoceanography*, *4*, 413–446. https://doi.org/10.1029/PA004i004p00413

Reilly, B., Tauxe, L., Bailey, I., Brachfeld, S., Fenton-Samuels, K., Hatfield, R., et al. (2025a). IODP Site U1537 1.7-3.3 Ma rock magnetic data (FC, ZFC, LTC-RTSIRM, hysteresis, DCD, FORCs) [Dataset]. *Zenodo*. https://doi.org/10.5281/zenodo.14564186

Reilly, B., Tauxe, L., Bailey, I., Brachfeld, S., Fenton-Samuels, K., Hatfield, R., et al. (2025b). Tables in support of "Antarctic response to orbital forcing during the intensification of extensive bipolar glaciation (1.75-3.30 Ma) from relative paleomagnetic intensity (RPI) stratigraphy of the Dove Basin, Scotia Sea" [Dataset]. *Zenodo*. https://doi.org/10.5281/zenodo.14564253

Reilly, B., Tauxe, L., Bailey, I., Brachfeld, S., Fenton-Samuels, K., Hatfield, R., et al. (2026). Antarctic response to orbital forcing during the intensification of extensive bipolar glaciation (1.75-3.30 Ma) from relative paleomagnetic intensity (RPI) stratigraphy of the Dove Basin, Scotia Sea [Dataset]. *Magnetics Information Consortium (MagIC)*. https://doi.org/10.7288/V4/MAGIC/20255

Reilly, B., Tauxe, L., Brachfeld, S., Raymo, M., Bailey, I., Hemming, S., et al. (2020). IODP Expedition 382: Supplementary tables for "New magnetostratigraphic insights from Iceberg Alley on the rhythms of Antarctic climate during the Plio-Pleistocene" [Dataset]. *Zenodo*. https://doi.org/10.5281/zenodo.3776573

Reilly, B. T. (2024). IODP Site U1537 U-Channel CT scan DICOM data, SedCT output, and HU values [Dataset]. *Zenodo*. https://doi.org/10.5281/zenodo.14563999

Reilly, B. T., McCormick, M. L., Brachfeld, S. A., & Haley, B. A. (2020). Authigenic ferrimagnetic iron sulfide preservation due to nonsteady state diagenesis: A perspective from Perseverance Drift, Northwestern Weddell Sea. *Geochemistry, Geophysics, Geosystems*, *21*(11), e2020GC009380. https://doi.org/10.1029/2020GC009380

Reilly, B. T., Natter, C. J., & Brachfeld, S. A. (2016). Holocene glacial activity in Barilari Bay, west Antarctic Peninsula, tracked by magnetic mineral assemblages: Linking ice, ocean, and atmosphere. *Geochemistry, Geophysics, Geosystems*, *17*(11), 4553–4565. https://doi.org/10.1002/2016GC006627

Reilly, B. T., Stoner, J. S., Ólafsdóttir, S., Jennings, A., Hatfield, R., Kristjánsdóttir, G. B., & Geirsdóttir, Á. (2023). The amplitude and timescales of 0–15 ka paleomagnetic secular variation in the Northern North Atlantic. *JGR Solid Earth*, *128*(6), e2023JB026891. https://doi.org/10.1029/2023JB026891

Reilly, B. T., Stoner, J. S., & Wiest, J. (2017). SedCT: MATLAB™ tools for standardized and quantitative processing of sediment core computed tomography (CT) data collected using a medical CT scanner. *Geochemistry, Geophysics, Geosystems*, *18*(8), 3231–3240. https://doi.org/10.1002/2017GC006884

Reilly, B. T., Tauxe, L., Brachfeld, S., Raymo, M., Bailey, I., Hemming, S., et al. (2021). New magnetostratigraphic insights from Iceberg Alley on the rhythms of Antarctic climate during the Plio-Pleistocene. *Paleoceanography and Paleoclimatology*, *36*(2), e2020PA003994. https://doi.org/10.1029/2020PA003994

Reilly, B. T., Tauxe, L., Brachfeld, S. A., Kenlee, B., Gutjahr, M., Dale, A. W., et al. (2024). A geochemical mechanism for >10 m apparent downward offsets of magnetic reversals inferred from comparison of two Scotia Sea drill sites. *Geochemistry, Geophysics, Geosystems*, *25*(7), e2023GC011325. https://doi.org/10.1029/2023GC011325

Richter, C., Acton, G., Endris, C., & Radsted, M. (2007). Handbook for shipboard paleomagnetists. *ODP Tech. Note*, *34*.

Richter, T. O., Gaast, S. V. D., Koster, B., Vaars, A., Gieles, R., de Stigter, H. C., et al. (2006). The Avaatech XRF core scanner: Technical description and applications to NE Atlantic sediments. https://doi.org/10.1144/GSL.SP.2006.267.01.03

Roberts, A. P., Pike, C. R., & Verosub, K. L. (2000). First-order reversal curve diagrams: A new tool for characterizing the magnetic properties of natural samples. *Journal of Geophysical Research*, *105*(B12), 28461–28475. https://doi.org/10.1029/2000jb900326

Roberts, A. P., Tauxe, L., & Heslop, D. (2013). Magnetic paleointensity stratigraphy and high-resolution Quaternary geochronology: Successes and future challenges. *Quaternary Science Reviews*, *61*, 1–16. https://doi.org/10.1016/j.quascirev.2012.10.036

Roberts, A. P., Tauxe, L., Heslop, D., Zhao, X., & Jiang, Z. (2018). A critical appraisal of the "day" diagram. *Journal of Geophysical Research: Solid Earth*, *123*(4), 2618–2644. https://doi.org/10.1002/2017JB015247

Roberts, A. P., & Winklhofer, M. (2004). Why are geomagnetic excursions not always recorded in sediments? Constraints from post-depositional remanent magnetization lock-in modelling. *Earth and Planetary Science Letters*, *227*(3–4), 345–359. https://doi.org/10.1016/j.epsl.2004.07.040

Rohling, E. J., Foster, G. L., Grant, K. M., Marino, G., Roberts, A. P., Tamisiea, M. E., & Williams, F. (2014). Sea-level and deep-sea-temperature variability over the past 5.3 million years. *Nature*, *508*(7497), 477–482. https://doi.org/10.1038/nature13230

Roy, K., & Peltier, W. R. (2017). Space-geodetic and water level gauge constraints on continental uplift and tilting over North America: Regional convergence of the ICE-6G_C (VM5a/VM6) models. *Geophysical Journal International*, *210*(2), 1115–1142. https://doi.org/10.1093/gji/ggx156

Roy, K., & Peltier, W. R. (2018). Relative sea level in the Western Mediterranean basin: A regional test of the ICE-7G_NA (VM7) model and a constraint on late Holocene Antarctic deglaciation. *Quaternary Science Reviews*, *183*, 76–87. https://doi.org/10.1016/j.quascirev.2017.12.021

Ruddiman, W. F., Raymo, M., & McIntyre, A. (1986). Matuyama 41,000-year cycles: North Atlantic Ocean and northern hemisphere ice sheets. *Earth and Planetary Science Letters*, *80*(1–2), 117–129. https://doi.org/10.1016/0012-821X(86)90024-5

Ryan, W. B. F., Carbotte, S. M., Coplan, J. O., O'Hara, S., Melkonian, A., Arko, R., et al. (2009). Global multi-resolution topography synthesis. *Geochemistry, Geophysics, Geosystems*, *10*(3). https://doi.org/10.1029/2008GC002332

Sakuramoto, Y., Yamazaki, T., Kimoto, K., Miyairi, Y., Kuroda, J., Yokoyama, Y., & Matsuzaki, H. (2017). A geomagnetic paleointensity record of 0.6 to 3.2 Ma from sediments in the Western equatorial Pacific and remanent magnetization lock-in depth. *Journal of Geophysical Research: Solid Earth*, *122*(10), 7525–7543. https://doi.org/10.1002/2017JB014450

Sato, M., Makio, M., Hayashi, T., & Ohno, M. (2015). Abrupt intensification of North Atlantic Deep Water formation at the Nordic Seas during the late Pliocene climate transition. *Geophysical Research Letters*, *42*(12), 4949–4955. https://doi.org/10.1002/2015GL063307

Schwartz, M., Lund, S., & Johnson, T. (1996). Environmental factors as complicating influences in the recovery of quantitative geomagnetic-field paleointensity estimates from sediments. *Geophysical Research Letters*, *23*(19), 2693–2696. https://doi.org/10.1029/96GL02375

Seidenstein, J. L., Leckie, R. M., McKay, R., De Santis, L., Harwood, D., & IODP Expedition 374 Scientists. (2024). Pliocene–Pleistocene warm-water incursions and water mass changes on the Ross Sea continental shelf (Antarctica) based on foraminifera from IODP Expedition 374. *Journal of Micropalaeontology*, *43*(2), 211–238. https://doi.org/10.5194/jm-43-211-2024

Shackleton, N. J., Backman, J., Zimmerman, H. t., Kent, D. V., Hall, M. A., Roberts, D. G., et al. (1984). Oxygen isotope calibration of the onset of ice-rafting and history of glaciation in the North Atlantic region. *Nature*, *307*(5952), 620–623. https://doi.org/10.1038/307620a0

Shackleton, N. J., Berger, A., & Peltier, W. R. (1990). An alternative astronomical calibration of the lower Pleistocene timescale based on ODP Site 677. *Earth and Environmental Science Transactions of the Royal Society of Edinburgh*, *81*(4), 251–261. https://doi.org/10.1017/s0263593300020782

Shackleton, N. J., Crowhurst, S., Hagelberg, T., Pisias, N. G., & Schneider, D. A. (1995). 6. A new late Neogene time scale: Application to Leg 138 sites. In *Proceedings of the Ocean Drilling Program* (pp. 73–101). Scientific Results.

Shakun, J. D., Raymo, M. E., & Lea, D. W. (2016). An early Pleistocene Mg/Ca-δ^{18}O record from the Gulf of Mexico: Evaluating ice sheet size and pacing in the 41-kyr world. *Paleoceanography*, *31*(7), PA002956-1027. https://doi.org/10.1002/2016PA002956

Shin, J. Y., Kim, S., Zhao, X., Yoo, K.-C., Yu, Y., Lee, J. I., et al. (2020). Particle-size dependent magnetic properties of Scotia Sea sediments since the last glacial maximum: Glacial ice-sheet discharge controlling magnetic proxies. *Palaeogeography, Palaeoclimatology, Palaeoecology*, *557*, 109906. https://doi.org/10.1016/j.palaeo.2020.109906

Simon, Q., Bourlès, D. L., Thouveny, N., Horng, C.-S., Valet, J.-P., Bassinot, F., & Choy, S. (2018). Cosmogenic signature of geomagnetic reversals and excursions from the Réunion event to the Matuyama–Brunhes transition (0.7–2.14 Ma interval). *Earth and Planetary Science Letters*, *482*, 510–524. https://doi.org/10.1016/j.epsl.2017.11.021

Singer, B. S. (2014). A Quaternary geomagnetic instability time scale. *Quaternary Geochronology*, *21*, 29–52. https://doi.org/10.1016/j.quageo.2013.10.003

Singer, B. S., Jicha, B. R., Condon, D. J., Macho, A. S., Hoffman, K. A., Dierkhising, J., et al. (2014). Precise ages of the Réunion event and Huckleberry ridge excursion: Episodic clustering of geomagnetic instabilities and the dynamics of flow within the outer core. *Earth and Planetary Science Letters*, *405*, 25–38. https://doi.org/10.1016/j.epsl.2014.08.011

Smirnov, A. V. (2009). Grain size dependence of low-temperature remanent magnetization in natural and synthetic magnetite: Experimental study. *Earth Planets and Space*, *61*(1), BF03352891-124. https://doi.org/10.1186/BF03352891

Smith, J. A., Hillenbrand, C.-D., Subt, C., Rosenheim, B. E., Frederichs, T., Ehrmann, W., et al. (2021). History of the Larsen C ice shelf reconstructed from sub–ice shelf and offshore sediments. *Geology*, *49*(8), 978–982. https://doi.org/10.1130/G48503.1

Sprenk, D., Weber, M. E., Kuhn, G., Rosén, P., Frank, M., Molina-Kescher, M., et al. (2013). Southern Ocean bioproductivity during the last glacial cycle – New detection method and decadal-scale insight from the Scotia Sea. *Geological Society*, *381*, 245–261. https://doi.org/10.1144/SP381.17

Stober, J. C., & Thompson, R. (1979). An investigation into the source of magnetic minerals in some Finnish lake sediments. *Earth and Planetary Science Letters*, *45*(2), 464–474. https://doi.org/10.1016/0012-821X(79)90145-6

Stoner, J. S., Channell, J. E. T., Hillaire-Marcel, C., & Kissel, C. (2000). Geomagnetic paleointensity and environmental record from Labrador Sea core MD95-2024: Global marine sediment and ice core chronostratigraphy for the last 110 kyr. *Earth and Planetary Science Letters*, *183*(1–2), 161–177. https://doi.org/10.1016/s0012-821x(00)00272-7

Stoner, J. S., Channell, J. E. T., Mazaud, A., Strano, S. E., & Xuan, C. (2013). The influence of high-latitude flux lobes on the Holocene paleomagnetic record of IODP site U1305 and the northern North Atlantic. *Geochemistry, Geophysics, Geosystems*, *14*(10), 4623–4646. https://doi.org/10.1002/ggge.20272

Stoner, J. S., Laj, C., Channell, J. E. T., & Kissel, C. (2002). South Atlantic and North Atlantic geomagnetic paleointensity stacks (0–80ka): Implications for inter-hemispheric correlation. *Quaternary Science Reviews*, *21*(10), 1141–1151. https://doi.org/10.1016/s0277-3791(01)00136-6

Stoner, J. S., & St-Onge, G. (2007). Chapter three magnetic stratigraphy in paleoceanography: Reversals, excursions, paleointensity, and secular variation. In *Developments in marine geology* (pp. 99–138). Elsevier.

Tauxe, L. (1993). Sedimentary records of relative paleointensity of the geomagnetic field: Theory and practice. *Reviews of Geophysics*, *31*(3), 319–354. https://doi.org/10.1029/93rg01771

Tauxe, L., Cych, B., Sprain, C., Turner, G., Hagstrum, J., Musgrave, R., et al. (2025). *The history of the Earth's magnetic field strength over the last three million years: An updated global view (GP31A-0304)*. Presented at the American Geophysical Union Fall Meeting 2025. Retrieved from https://agu.confex.com/agu/agu25/meetingapp.cgi/Paper/1870040

Tauxe, L., Herbert, T., Shackleton, N. J., & Kok, Y. S. (1996). Astronomical calibration of the Matuyama-Brunhes boundary: Consequences for magnetic remanence acquisition in marine carbonates and the Asian loess sequences. *Earth and Planetary Science Letters*, *140*(1–4), 133–146. https://doi.org/10.1016/0012-821x(96)00030-1

Tauxe, L., Opdyke, N. D., Pasini, G., & Elmi, C. (1983). Age of the Plio-Pleistocene boundary in the Vrica section, southern Italy. *Nature*, *304*(5922), 125–129. https://doi.org/10.1038/304125a0

Tauxe, L., Pick, T., & Kok, Y. S. (1995). Relative paleointensity in sediments: A Pseudo-Thellier approach. *Geophysical Research Letters*, *22*(21), 2885–2888. https://doi.org/10.1029/95GL03166

Tauxe, L., & Yamazaki, T. (2007). 5.13—Paleointensities. In G. Schubert (Ed.), *Treatise on geophysics* (pp. 509–563). Elsevier. https://doi.org/10.1016/B978-044452748-6.00098-5

Thébault, E., Finlay, C. C., Beggan, C. D., Alken, P., Aubert, J., Barrois, O., et al. (2015). International geomagnetic reference field: The 12th generation. *Earth Planets and Space*, *67*, 79. https://doi.org/10.1186/s40623-015-0228-9

Thompson, R., & Clark, R. M. (1989). Sequence slotting for stratigraphic correlation between cores: Theory and practice. *Journal of Paleolimnology*, *2*(3), 173–184. https://doi.org/10.1007/BF00202045

Truax, O. J., Nelson, F., Riesselman, C. R., Ohneiser, C., Lee, J. I., Yoo, K.-C., et al. (2025). A Holocene paleosecular variation record from the Northwestern Ross Sea, Antarctica. *Geochemistry, Geophysics, Geosystems*, *26*(2), e2024GC011912. https://doi.org/10.1029/2024GC011912

Valet, J., & Meynadier, L. (1993). Geomagnetic field intensity and reversals during the past four million years. *Nature*, *366*(6452), 234–238. https://doi.org/10.1038/366234a0

Valet, J., & Meynadier, L. (1998). A comparison of different techniques for relative paleointensity. *Geophysical Research Letters*, *25*(1), 89–92. https://doi.org/10.1029/97GL03489

Valet, J.-P., Meynadier, L., & Guyodo, Y. (2005). Geomagnetic dipole strength and reversal rate over the past two million years. *Nature*, *435*(7043), 802–805. https://doi.org/10.1038/nature03674

Warnock, J. P., Reilly, B. T., Raymo, M. E., Weber, M. E., Peck, V., Williams, T., et al. (2022). Latitudinal variance in the drivers and pacing of warmth during mid-Pleistocene MIS 31 in the Antarctic zone of the Southern Ocean. *Paleoceanography and Paleoclimatology*, *37*(8), e2021PA004394. https://doi.org/10.1029/2021PA004394

Weber, M., Raymo, M., Peck, V., & Williams, T. (2019). Expedition 382 preliminary report: Iceberg Alley and subantarctic ice and ocean dynamics [Dataset]. *Magnetics Information Consortium*. https://doi.org/10.7288/V4/MAGIC/16842

Weber, M. E., Bailey, I., Hemming, S. R., Martos, Y. M., Reilly, B. T., Ronge, T. A., et al. (2022). Antiphased dust deposition and productivity in the Antarctic zone over 1.5 million years. *Nature Communications*, *13*, 1–18. https://doi.org/10.1038/s41467-022-29642-5

Weber, M. E., Clark, P. U., Kuhn, G., Timmermann, A., Sprenk, D., Gladstone, R., et al. (2014). Millennial-scale variability in Antarctic ice-sheet discharge during the last deglaciation. *Nature*, *510*(7503), 134–138. https://doi.org/10.1038/nature13397

Weber, M. E., Kuhn, G., Sprenk, D., Rolf, C., Ohlwein, C., & Ricken, W. (2012). Dust transport from Patagonia to Antarctica – A new stratigraphic approach from the Scotia Sea and its implications for the last glacial cycle. *Quaternary Science Reviews*, *36*, 177–188. https://doi.org/10.1016/j.quascirev.2012.01.016

Weber, M. E., Raymo, M. E., Peck, V. L., Williams, T., Armbrecht, L., Bailey, I., et al. (2021f). IODP Expedition 382 magnetic remanence (SRM-longcore) [Dataset]. *Zenodo*. https://doi.org/10.5281/zenodo.8264020

Weber, M. E., Raymo, M. E., Peck, V. L., Williams, T., Armbrecht, L., Bailey, I., et al. (2021g). IODP Expedition 382 magnetic susceptibility (whole round) [Dataset]. *Zenodo*. https://doi.org/10.5281/zenodo.8263927

Weber, M. E., Raymo, M. E., Peck, V. L., Williams, T., Armbrecht, L., Bailey, I., et al. (2021h). IODP Expedition 382 bulk density (GRA) [Dataset]. *Zenodo*. https://doi.org/10.5281/zenodo.8256649

Weber, M. E., Raymo, M. E., Peck, V. L., Williams, T., Armbrecht, L., Bailey, I., et al. (2021i). IODP Expedition 382 color reflectance [Dataset]. *Zenodo*. https://doi.org/10.5281/zenodo.8263963

Weber, M. E., Raymo, M. E., Peck, V. L., Williams, T., Armbrecht, L., Bailey, I., et al. (2021j). IODP Expedition 382 natural gamma radiation [Dataset]. *Zenodo*. https://doi.org/10.5281/zenodo.8263931

Weber, M. E., Raymo, M. E., Peck, V. L., Williams, T., Armbrecht, L., Bailey, I., et al. (2021k). IODP Expedition 382 X-ray fluorescence (XRF) [Dataset]. *International Ocean Discovery Program*. https://doi.org/10.5281/zenodo.18330765

Weber, M. E., Raymo, M. E., Peck, V. L., Williams, T., Armbrecht, L., Bailey, I., et al. (2021a). Expedition 382 summary. In *Volume 382: Iceberg Alley and subantarctic ice and ocean dynamics, Proceedings of the International Ocean Discovery Program*. International Ocean Discovery Program.

Weber, M. E., Raymo, M. E., Peck, V. L., Williams, T., Armbrecht, L., Bailey, I., et al. (2021b). Site U1538, in: Volume 382: Iceberg Alley and subantarctic ice and ocean dynamics. In *Proceedings of the International Ocean Discovery Program*. International Ocean Discovery Program.

Weber, M. E., Raymo, M. E., Peck, V. L., Williams, T., Armbrecht, L., Bailey, I., et al. (2021c). Site U1537, in: Volume 382: Iceberg Alley and subantarctic ice and ocean dynamics. In *Proceedings of the International Ocean Discovery Program*. International Ocean Discovery Program.

Weber, M. E., Raymo, M. E., Peck, V. L., Williams, T., Armbrecht, L., Bailey, I., et al. (2021d). Site U1536, in: Volume 382: Iceberg Alley and subantarctic ice and ocean dynamics. In *Proceedings of the International Ocean Discovery Program*. International Ocean Discovery Program.

Weber, M. E., Raymo, M. E., Peck, V. L., Williams, T., Armbrecht, L., Bailey, I., et al. (2021e). Expedition 382 methods. In *Volume 382: Iceberg Alley and subantarctic ice and ocean dynamics, Proceedings of the International Ocean Discovery Program*. International Ocean Discovery Program.

Weeks, R., Laj, C., Endignoux, L., Fuller, M., Roberts, A., Manganne, R., et al. (1993). Improvements in long-core measurement techniques: Applications in palaeomagnetism and palaeoceanography. *Geophysical Journal International*, *114*(3), 651–662. https://doi.org/10.1111/j.1365-246X.1993.tb06994.x

Willmott, V., Domack, E. W., Canals, M., & Brachfeld, S. (2006). A high resolution relative paleointensity record from the Gerlache-Boyd paleo-ice stream region, northern Antarctic Peninsula. *Quaternary Research*, *66*, 1–11. https://doi.org/10.1016/j.yqres.2006.01.006

Xiao, W., Frederichs, T., Gersonde, R., Kuhn, G., Esper, O., & Zhang, X. (2016). Constraining the dating of late Quaternary marine sediment records from the Scotia Sea (Southern Ocean). *Quaternary Geochronology*, *31*, 97–118. https://doi.org/10.1016/j.quageo.2015.11.003

Xuan, C., & Channell, J. E. T. (2009). UPmag: MATLAB software for viewing and processing u channel or other pass-through paleomagnetic data. *Geochemistry, Geophysics, Geosystems*, *10*. https://doi.org/10.1029/2009GC002584

Xuan, C., Channell, J. E. T., & Hodell, D. A. (2016). Quaternary magnetic and oxygen isotope stratigraphy in diatom-rich sediments of the southern Gardar drift (IODP site U1304, North Atlantic). *Quaternary Science Reviews*, *142*, 74–89. https://doi.org/10.1016/j.quascirev.2016.04.010

Xuan, C., & Oda, H. (2015). UDECON: Deconvolution optimization software for restoring high-resolution records from pass-through paleomagnetic measurements. *Earth Planets and Space*, *67*, 1–17. https://doi.org/10.1186/s40623-015-0332-x

Yamazaki, T., & Oda, H. (2005). A geomagnetic paleointensity stack between 0.8 and 3.0 Ma from equatorial Pacific sediment cores: Paleointensity stack. *Geochemistry, Geophysics, Geosystems*, *6*(11). https://doi.org/10.1029/2005GC001001

Yamazaki, T., & Yamamoto, Y. (2018). Relative paleointensity and inclination anomaly over the last 8 Myr obtained from the Integrated Ocean Drilling Program Site U1335 sediments in the eastern equatorial Pacific. *Journal of Geophysical Research: Solid Earth*, *123*(9), 7305–7320. https://doi.org/10.1029/2018JB016209

Yan, Y., Kurbatov, A. V., Mayewski, P. A., Shackleton, S., & Higgins, J. A. (2023). Early Pleistocene East Antarctic temperature in phase with local insolation. *Nature Geoscience*, *16*(1), 50–55. https://doi.org/10.1038/s41561-022-01095-x

Ziegler, L. B., Constable, C. G., Johnson, C. L., & Tauxe, L. (2011). PADM2M: A penalized maximum likelihood model of the 0-2 Ma palaeomagnetic axial dipole moment. *Geophysical Journal International*, *184*(3), 1069–1089. https://doi.org/10.1111/j.1365-246X.2010.04905.x

Paleoceanography and Paleoclimatology

Supporting Information for

Antarctic response to orbital forcing during the intensification of extensive bipolar glaciation (1.75-3.30 Ma) from relative paleomagnetic intensity (RPI) stratigraphy of the Dove Basin, Scotia Sea

Brendan Reilly[1], Lisa Tauxe[2], Ian Bailey[3], Stefanie Brachfeld[4], Kelly Fenton-Samuels[1,5], Robert G. Hatfield[6], Sidney Hemming[1,5], Claire E. Jasper[1,5], Suzanne O'Connell[7], Maureen E. Raymo[1,5], Joseph Stoner[8], Jonathan Warnock[9], Trevor Williams[10]

[1]Lamont-Doherty Earth Observatory, Columbia University, Palisades, NY, USA

[2]Scripps Institution of Oceanography, University of California San Diego, La Jolla, CA, USA

[3] Camborne School of Mines, Department of Earth and Environmental Sciences, University of Exeter, Penryn Campus, Cornwall, UK

[4]Department of Earth and Environmental Studies, Montclair State University, Upper Montclair, NJ, USA

[5]Department of Earth and Environmental Sciences, Columbia University, New York, NY, USA

[6]Department of Geological Sciences, University of Florida, Gainesville, FL, USA

[7]Department of Earth and Environmental Sciences, Wesleyan University, Middletown, CT, USA

[8]College of Earth, Ocean, and Atmospheric Sciences, Oregon State University, Corvallis, OR, USA

[9]Department of Geoscience, Indiana University of Pennsylvania, Indiana, PA, USA

[10]International Ocean Discovery Program, Texas A&M University, College Station, USA

Contents of this file

Additional Supporting Information

Captions for Tables S1 to S9 (tables available at Reilly et al., 2025b; https://doi.org/10.5281/zenodo.14564253).

Introduction

This supplementary file includes 19 figures and the captions for 9 tables. Supplementary tables can be found in the Zenodo repository (Reilly et al., 2025b). For greater detail of Table S3, u-channel magnetic data are archived with the Magnetics Information Consortium (MagIC) database (Reilly et al., 2026). Rock magnetic data files are available through the Zenodo Repository (Reilly et al., 2025a). CT data presented in Figures S2-S14, including DICOM format files, are available through the Zenodo Repository (Reilly, 2024).

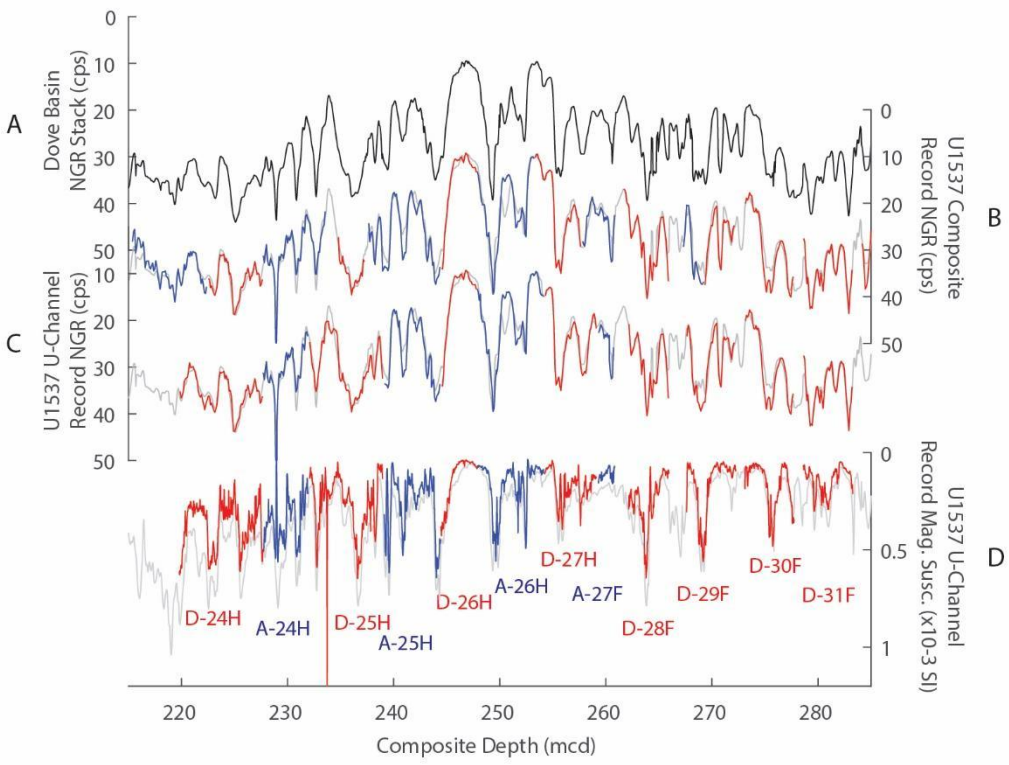

Figure S1. U-channel samples and comparison to U1537 composite depth, composite records, and stacks of Reilly et al. (2021). (a) Dove Basin NGR stack, using data from neighboring Sites U1536 and U1537 (black). (b) NGR data from Holes U1537A (blue) and U1537D (red) from intervals used to form the U1537 composite record compared with the Dove Basin NGR stack (gray). (c) NGR data from U1537 Holes A (Blue) and D (Red) from the intervals sampled with u-channels for this study compared with the Dove Basin NGR stack (gray). (d) Magnetic susceptibility measured on u-channel samples compared with a Dove Basin magnetic susceptibility stack generated in the same method as the Reilly et al. (2021) NGR stack in a. Magnetic susceptibility instrumental units reported by Weber et al. (2021e) were converted to SI units by multiplying by 6.8 x 10-6 (after Thomas et al., 2003).

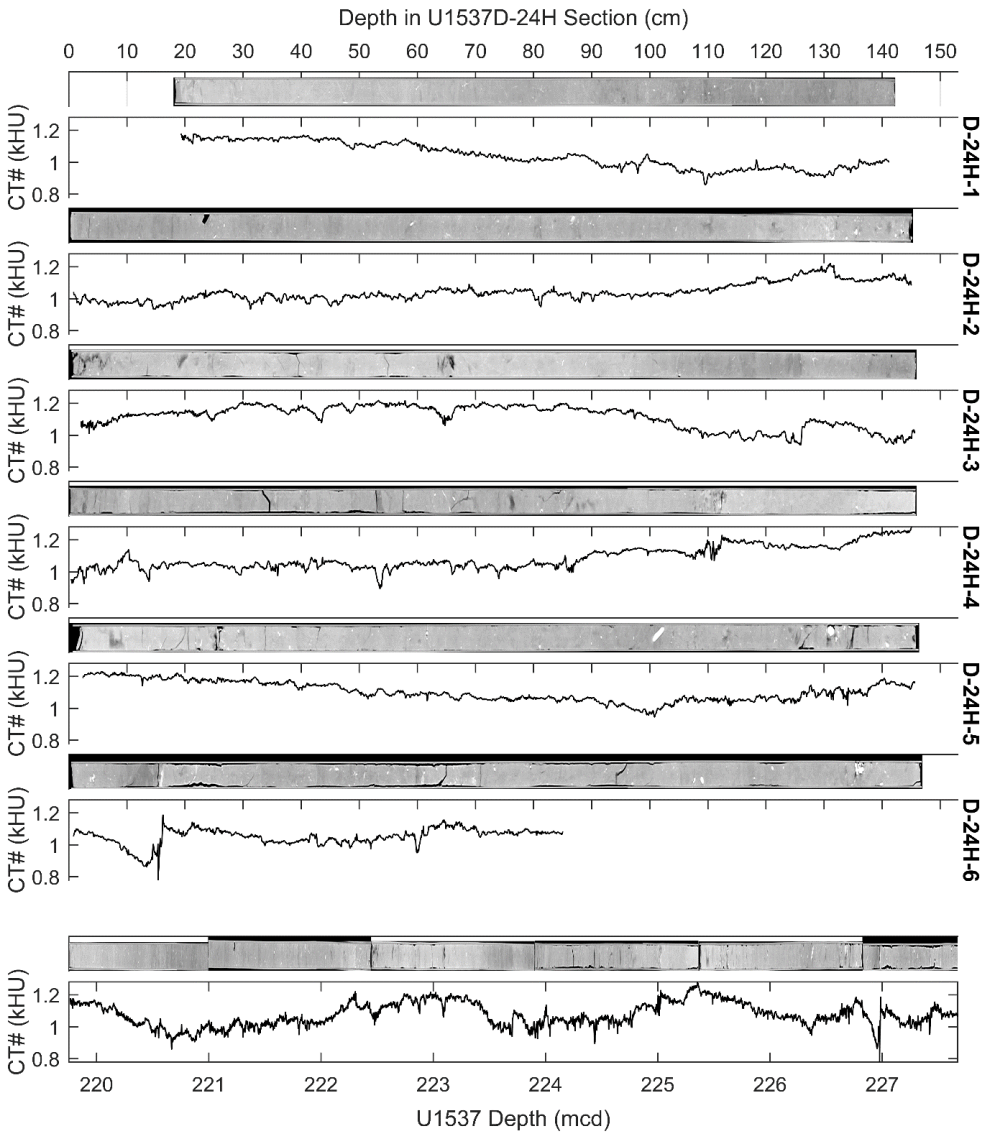

Figure S2. CT results from U1537D-24H u-channels. Images are 2 mm thick central slices, scaled from 200 (black; lower density ~1.16 g/cm^3) to 1400 (white; high density ~2.12 g/cm^3) HU. Black lines are downcore SedCT calculated CT# profiles (Reilly et al., 2017) for intervals used to build the composite record presented in this study (Figure 3C).

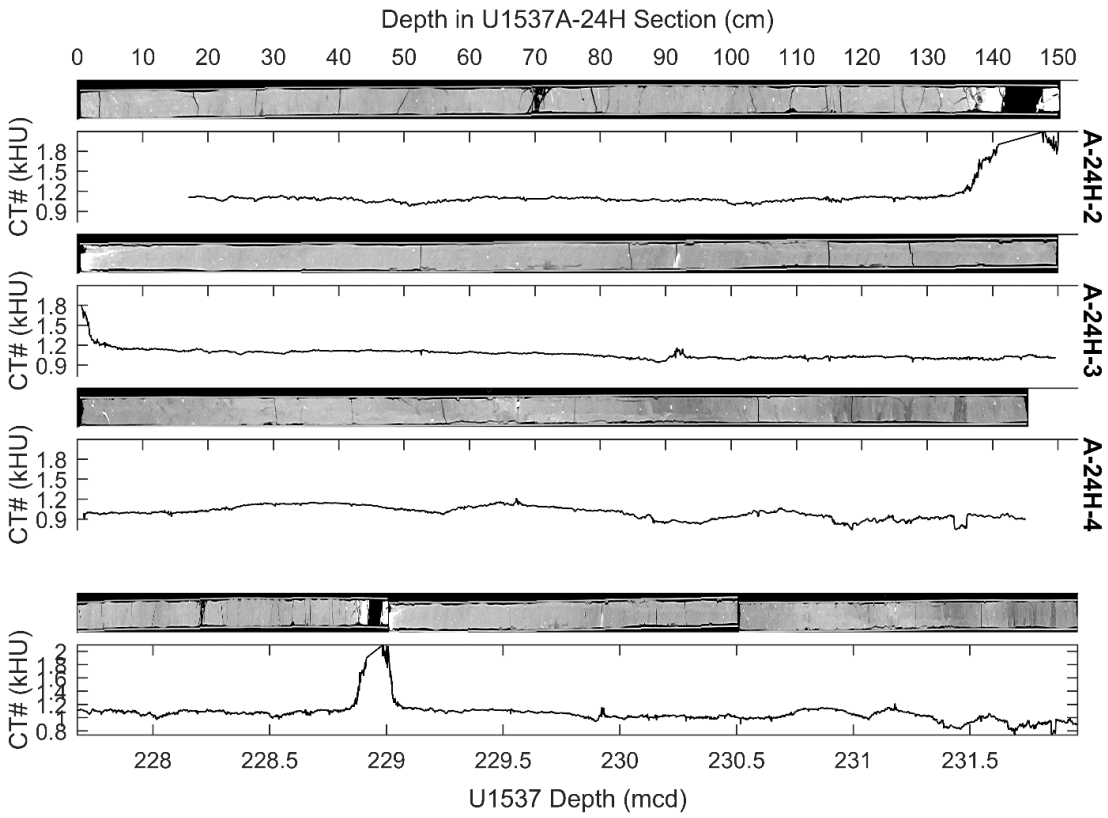

Figure S3. CT results from U1537A-24H u-channels. Images are 2 mm thick central slices, scaled from 200 (black; lower density ~1.16 g/cm^3) to 1400 (white; high density ~2.12 g/cm^3) HU. Black lines are downcore SedCT calculated CT# profiles (Reilly et al., 2017) for intervals used to build the composite record presented in this study (Figure 3C).

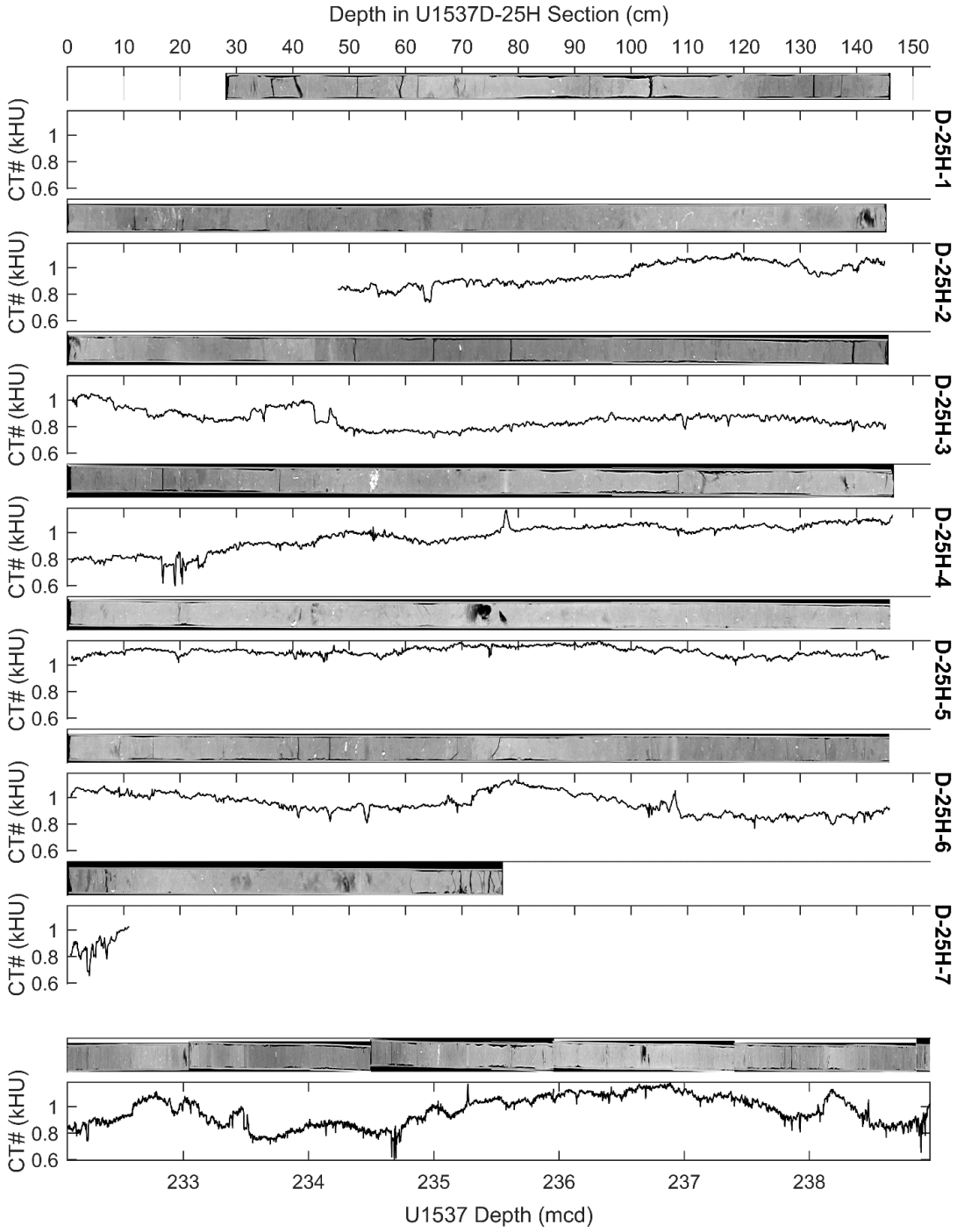

Figure S4. CT results from U1537D-25H u-channels. Images are 2 mm thick central slices, scaled from 200 (black; lower density ~1.16 g/cm^3) to 1400 (white; high density ~2.12 g/cm^3) HU. Black lines are downcore SedCT calculated CT# profiles

(Reilly et al., 2017) for intervals used to build the composite record presented in this study (Figure 3C).

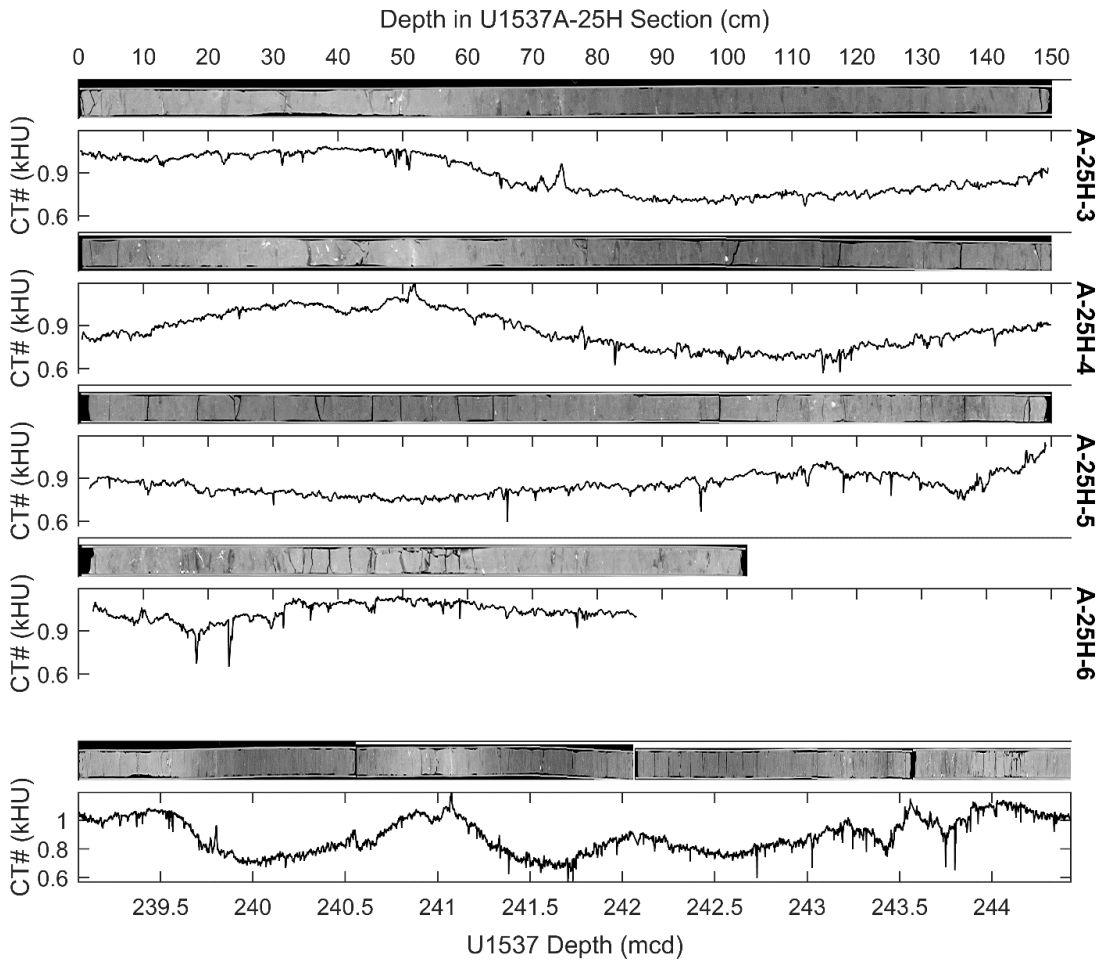

Figure S5. CT results from U1537A-25H u-channels. Images are 2 mm thick central slices, scaled from 200 (black; lower density ~1.16 g/cm^3) to 1400 (white; high density ~2.12 g/cm^3) HU. Black lines are downcore SedCT calculated CT# profiles (Reilly et al., 2017) for intervals used to build the composite record presented in this study (Figure 3C).

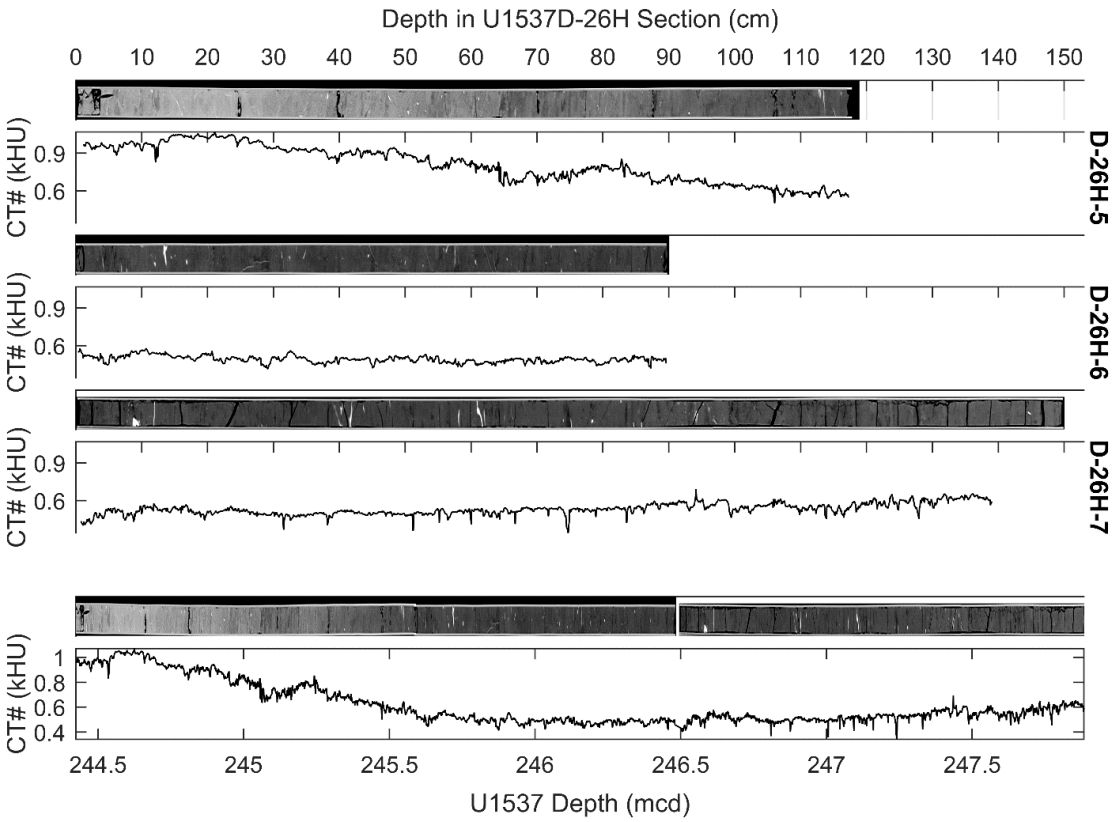

Figure S6. CT results from U1537D-26H u-channels. Images are 2 mm thick central slices, scaled from 200 (black; lower density ~1.16 g/cm^3) to 1400 (white; high density ~2.12 g/cm^3) HU. Black lines are downcore SedCT calculated CT# profiles (Reilly et al., 2017) for intervals used to build the composite record presented in this study (Figure 3C).

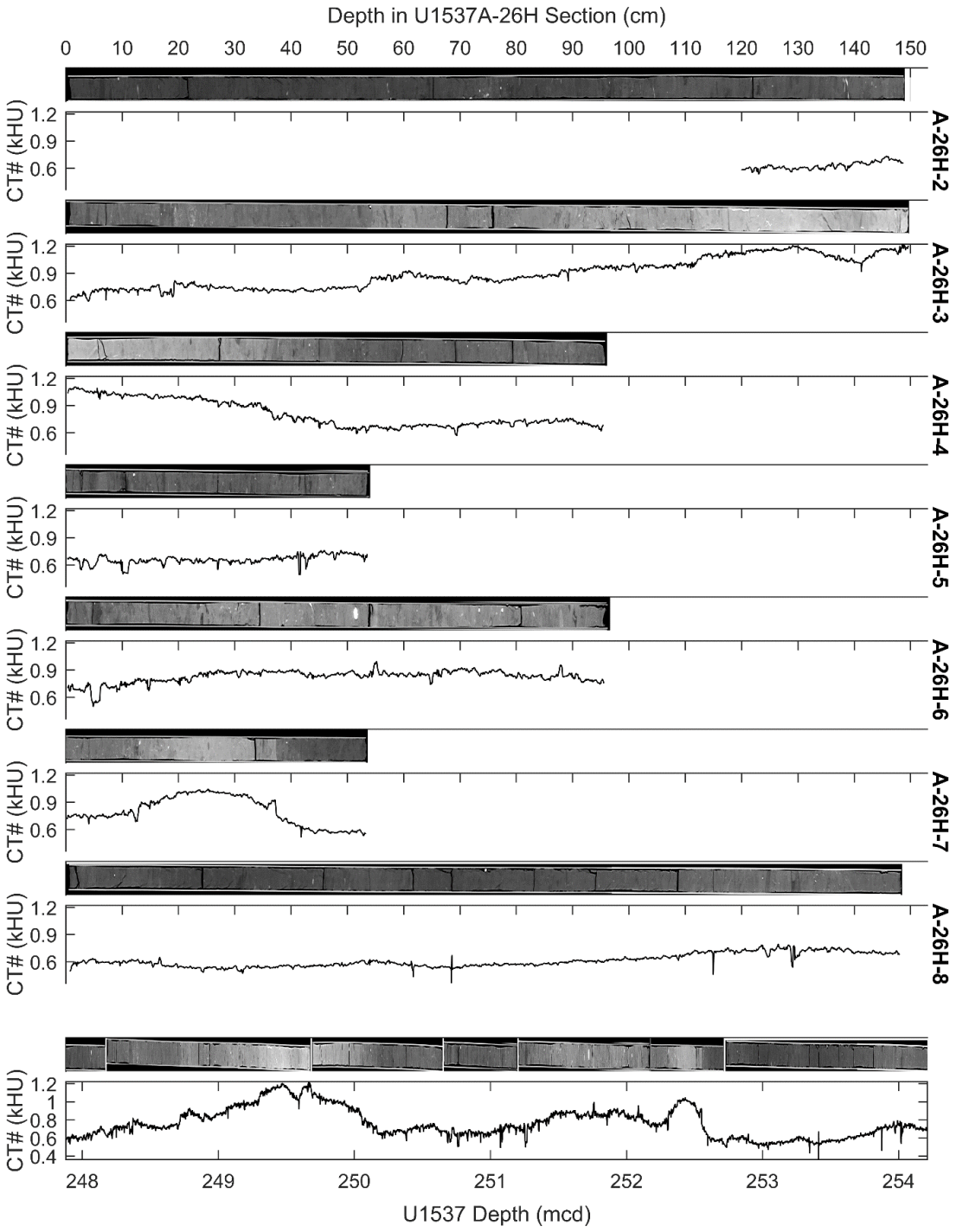

Figure S7. CT results from U1537A-26H u-channels. Images are 2 mm thick central slices, scaled from 200 (black; lower density ~1.16 g/cm^3) to 1400 (white; high density ~2.12 g/cm^3) HU. Black lines are downcore SedCT calculated CT# profiles

(Reilly et al., 2017) for intervals used to build the composite record presented in this study (Figure 3C).

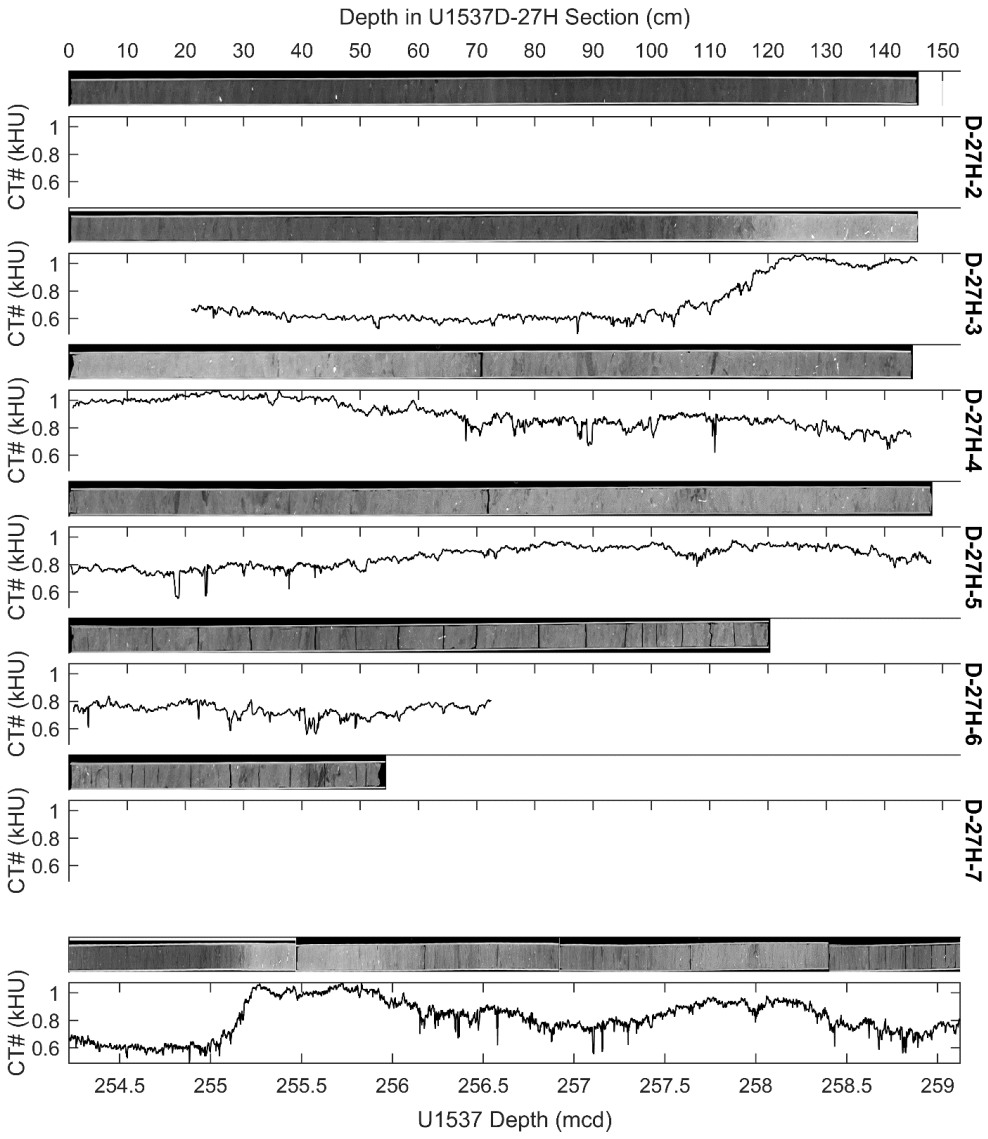

Figure S8. CT results from U1537D-27H u-channels. Images are 2 mm thick central slices, scaled from 200 (black; lower density ~1.16 g/cm^3) to 1400 (white; high density ~2.12 g/cm^3) HU. Black line are downcore SedCT calculated CT# profiles (Reilly et al., 2017) for intervals used to build the composite record presented in this study (Figure 3C).

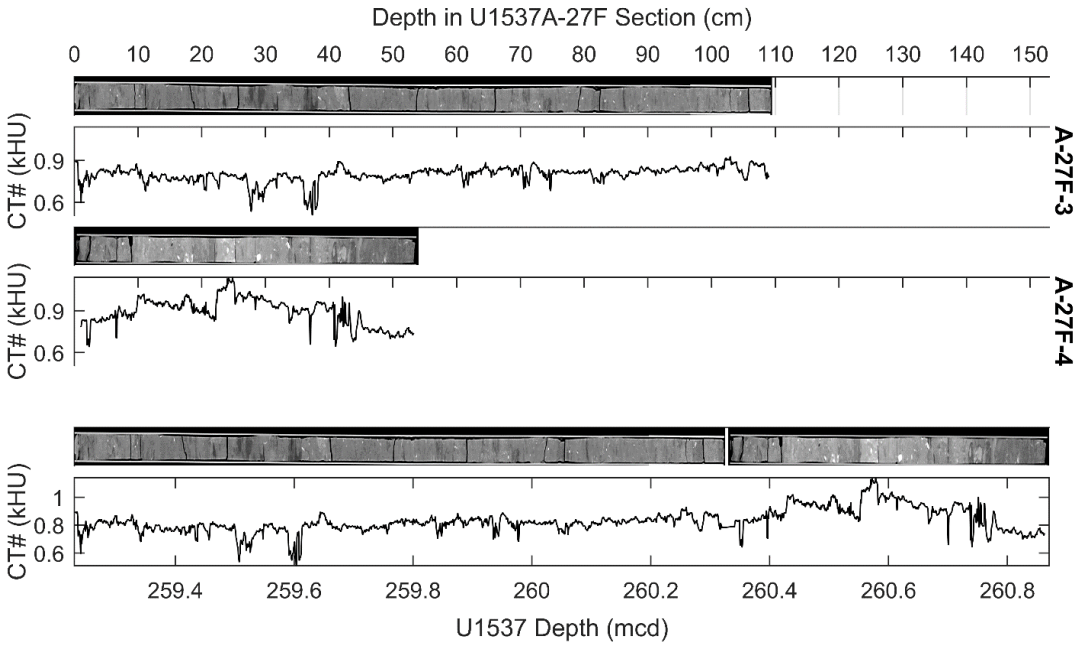

Figure S9. CT results from U1537A-27F u-channels. Images are 2 mm thick central slices, scaled from 200 (black; lower density ~1.16 g/cm^3) to 1400 (white; high density ~2.12 g/cm^3) HU. Black lines are downcore SedCT calculated CT# profiles (Reilly et al., 2017) for intervals used to build the composite record presented in this study (Figure 3C).

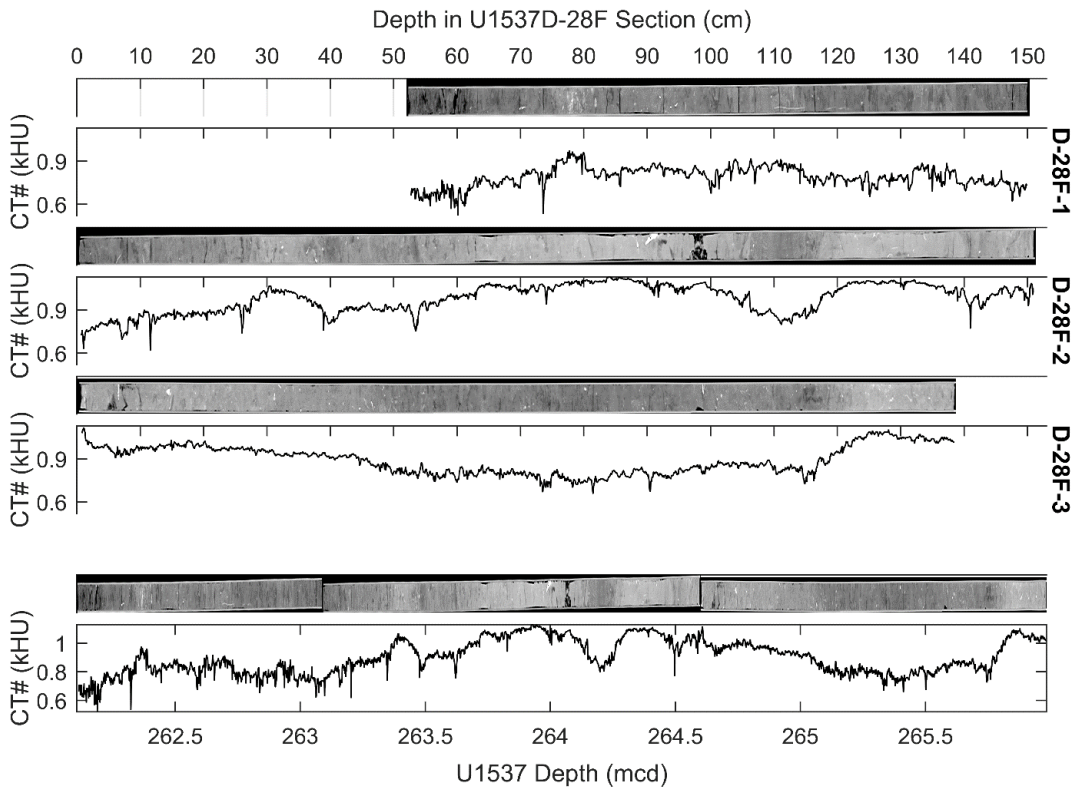

Figure S10. CT results from U1537D-28F u-channels. Images are 2 mm thick central slices, scaled from 200 (black; lower density ~1.16 g/cm^3) to 1400 (white; high density ~2.12 g/cm^3) HU. Black lines are downcore SedCT calculated CT# profiles (Reilly et al., 2017) for intervals used to build the composite record presented in this study (Figure 3C).

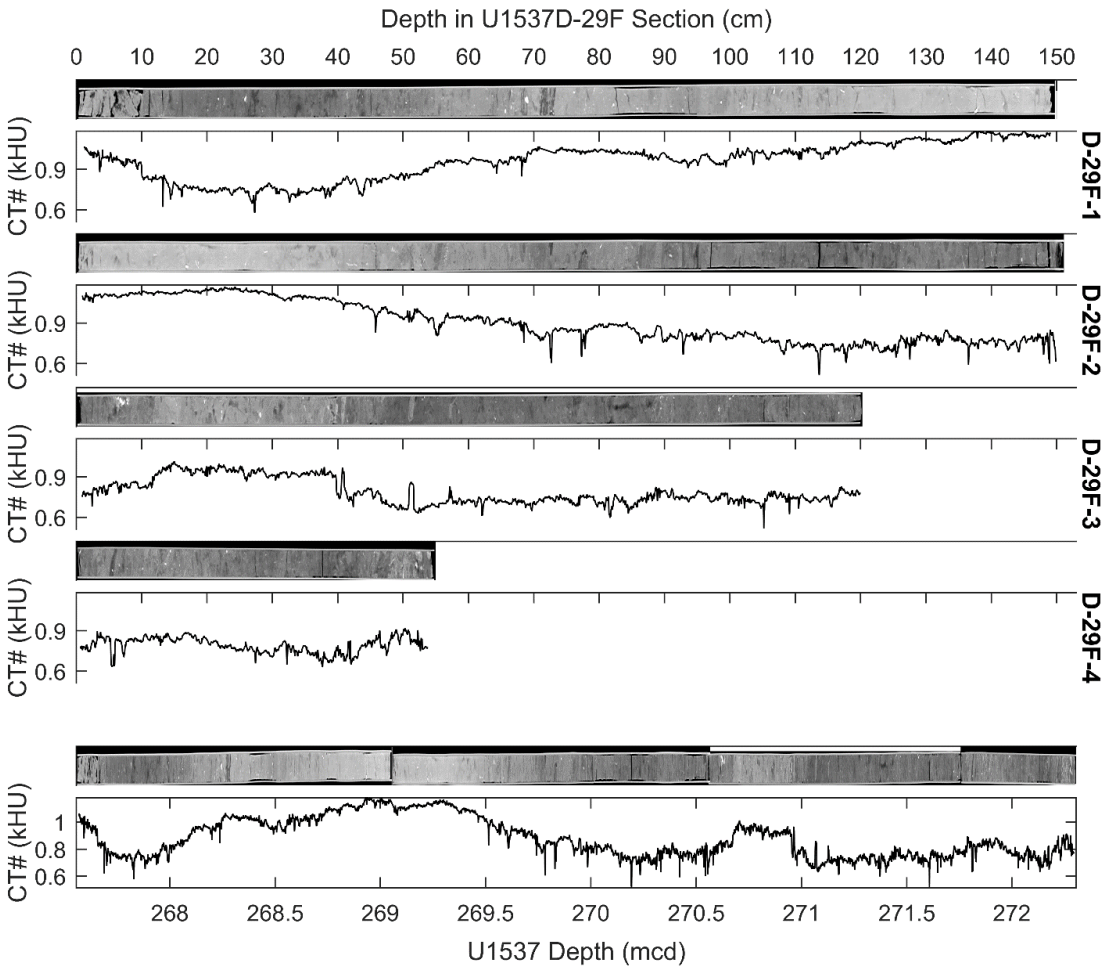

Figure S11. CT results from U1537D-29F u-channels. Images are 2 mm thick central slices, scaled from 200 (black; lower density ~1.16 g/cm^3) to 1400 (white; high density ~2.12 g/cm^3) HU. Black lines are downcore SedCT calculated CT# profiles (Reilly et al., 2017) for intervals used to build the composite record presented in this study (Figure 3C).

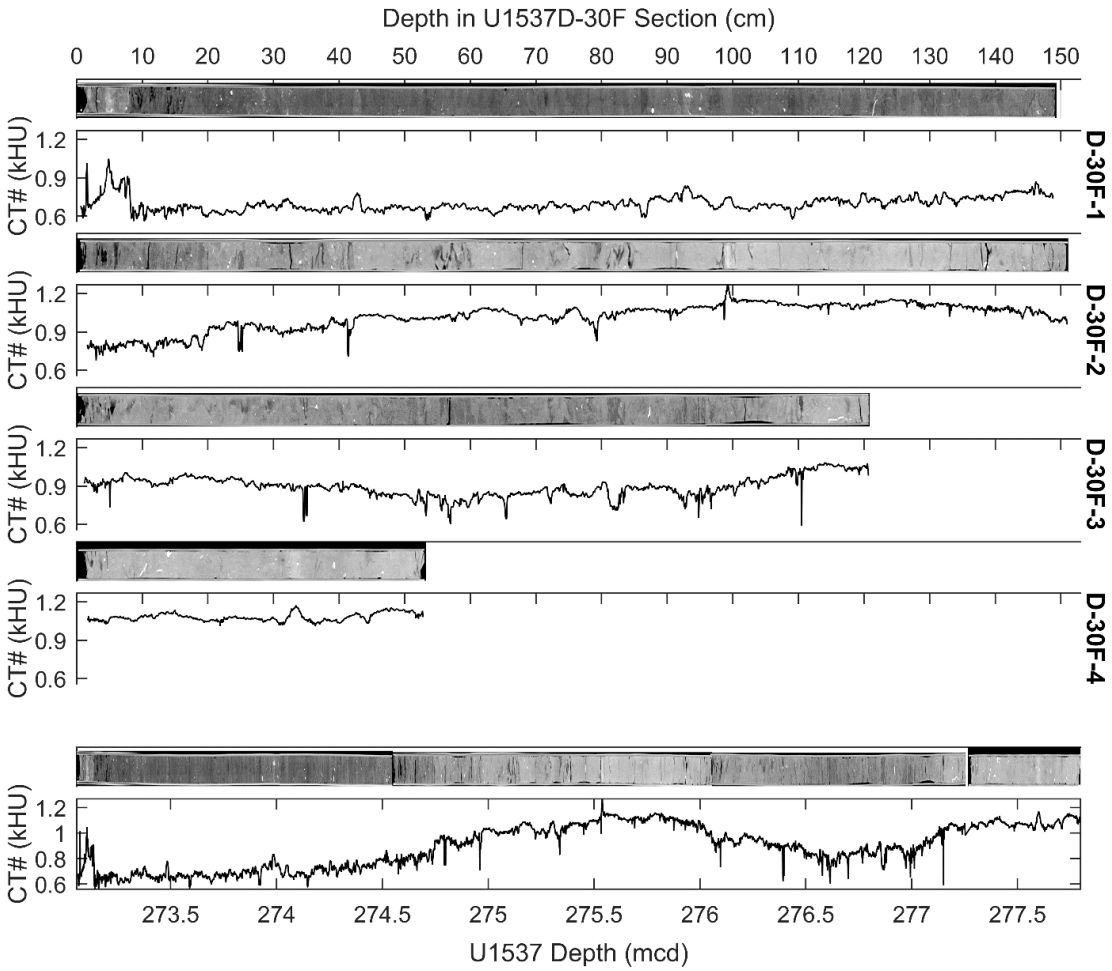

Figure S12. CT results from U1537D-30F u-channels. Images are 2 mm thick central slices, scaled from 200 (black; lower density ~1.16 g/cm^3) to 1400 (white; high density ~2.12 g/cm^3) HU. Black lines are downcore SedCT calculated CT# profiles (Reilly et al., 2017) for intervals used to build the composite record presented in this study (Figure 3C).

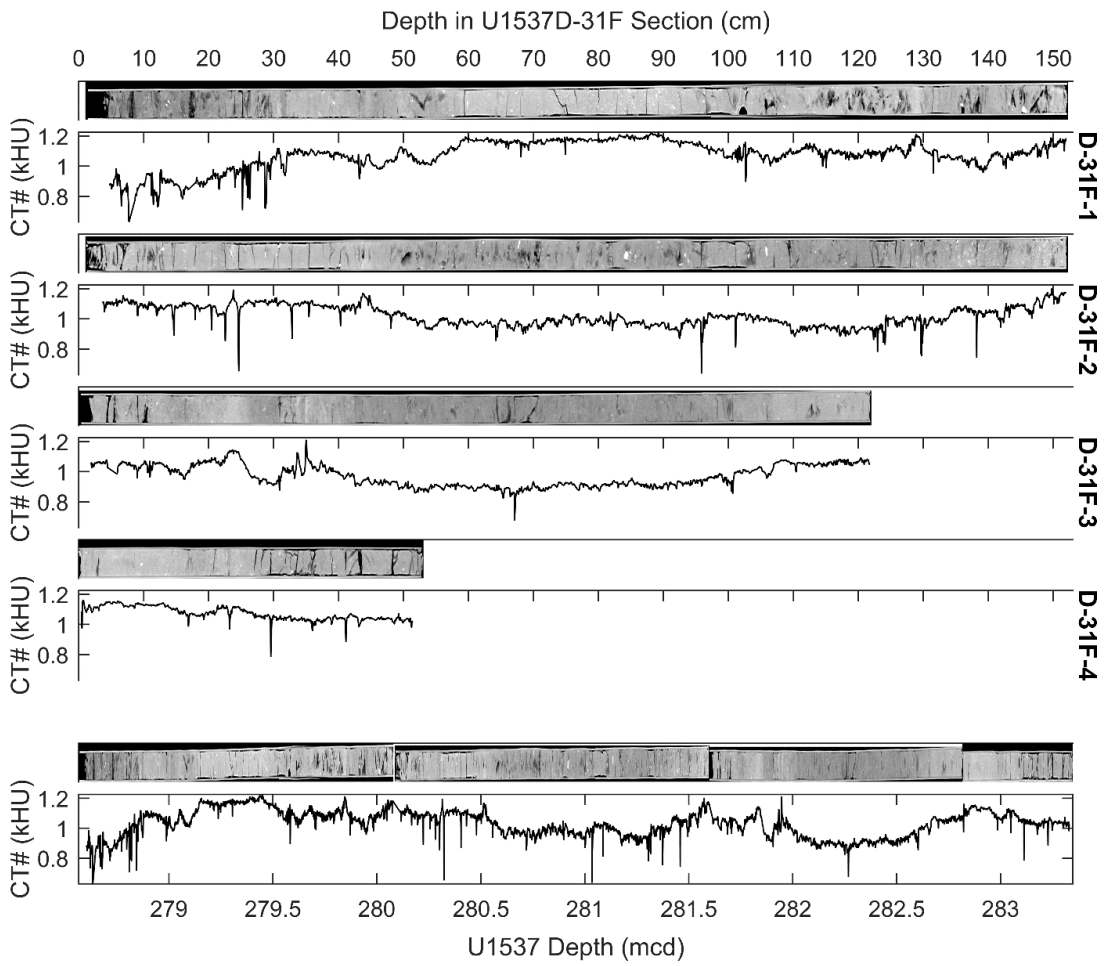

Figure S13. CT results from U1537D-31F u-channels. Images are 2 mm thick central slices, scaled from 200 (black; lower density ~1.16 g/cm^3) to 1400 (white; high density ~2.12 g/cm^3) HU. Black lines are downcore SedCT calculated CT# profiles (Reilly et al., 2017) for intervals used to build the composite record presented in this study (Figure 3C).

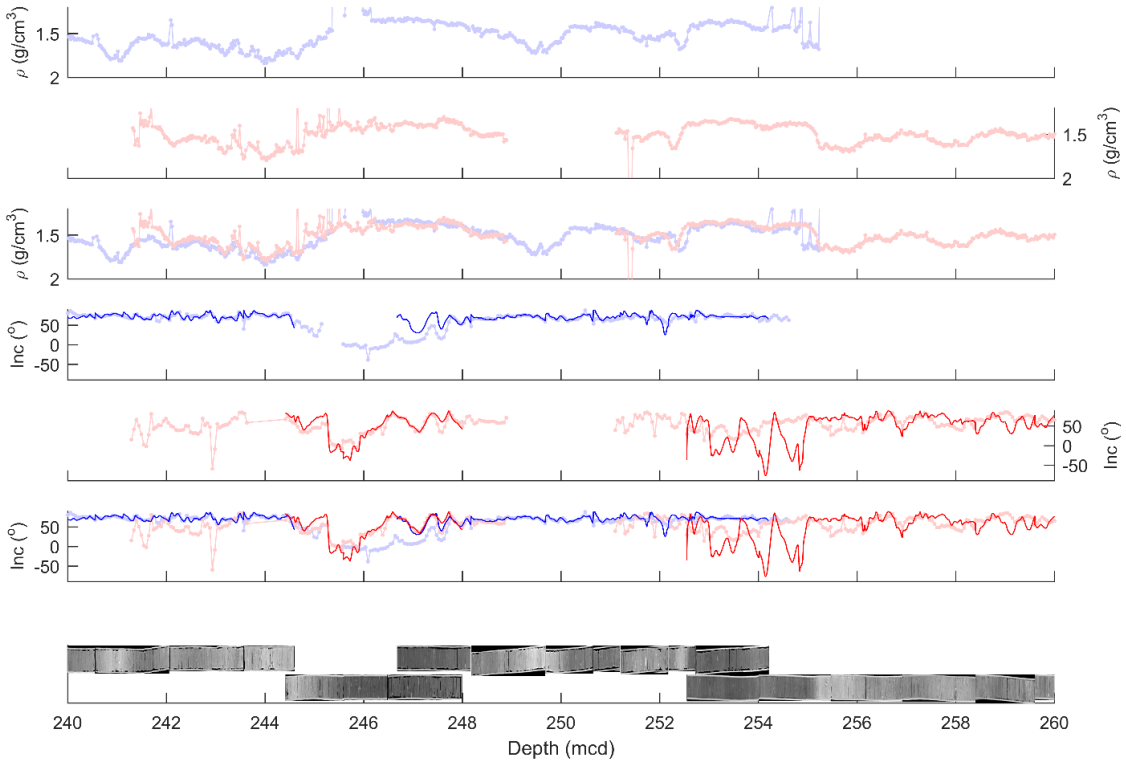

Figure S14. Comparison of shipboard and u-channel data around Biogenic Silica Events 1-3. Darker lines are u-channel data, lighter lines are shipboard data.

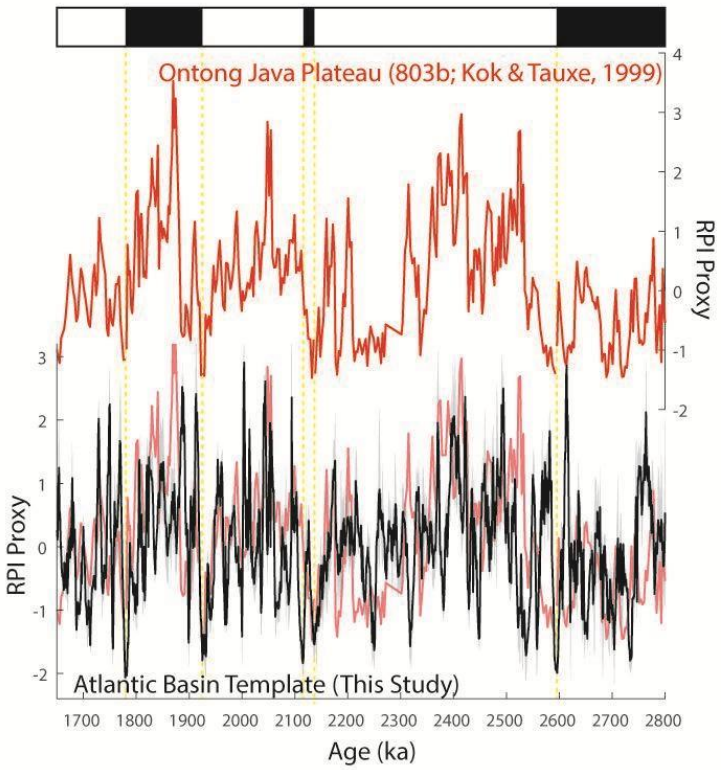

Figure S15. Comparison of the RPI template created for this study (black) with the 803b RPI record from the Ontong Java Plateau (Kok and Tauxe, 1999) on its magnetic reversal chronology with reversal ages updated to match the timescale used in this study.

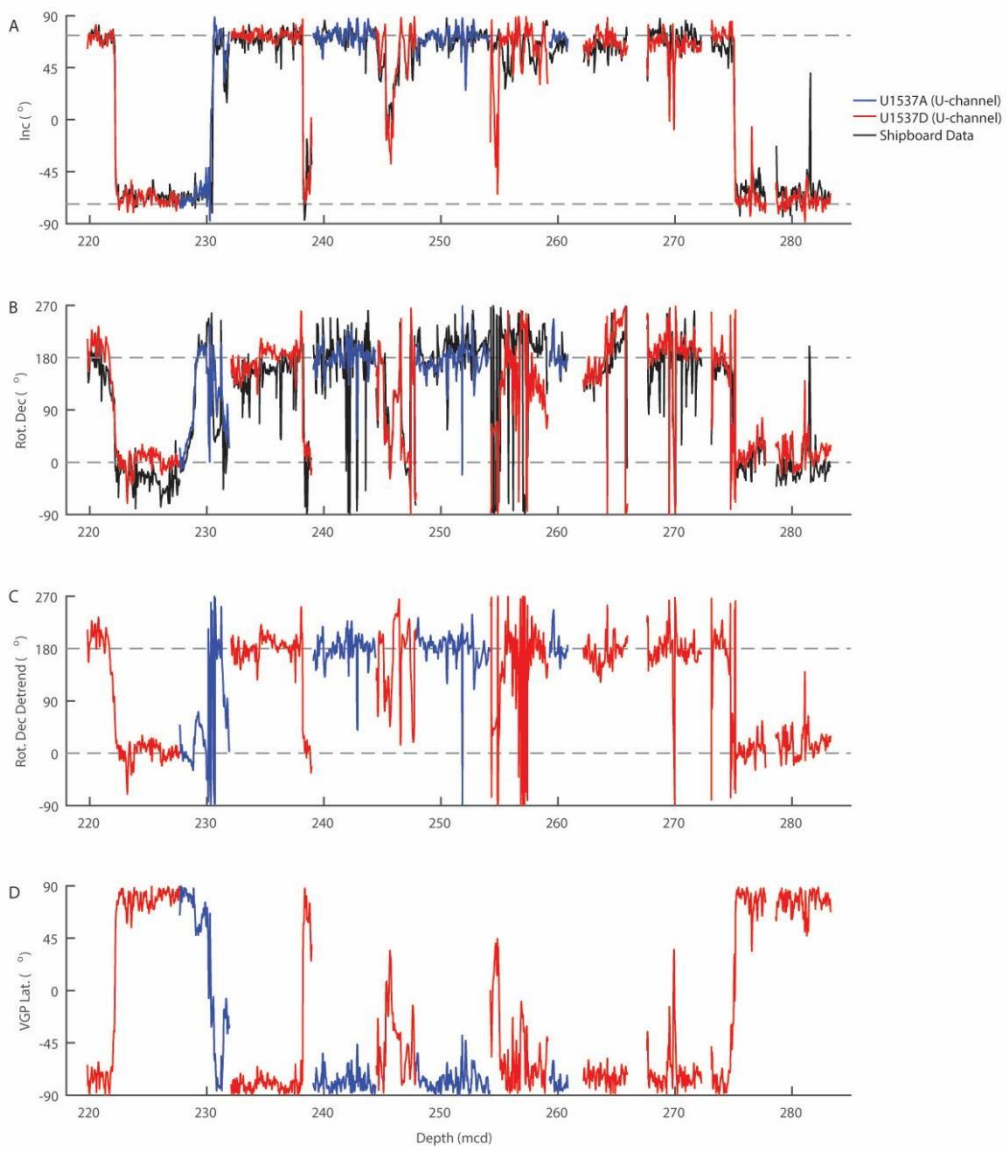

Figure S16. Comparison of shipboard (after 15 mT AF Demagnetization; black) and u-channel inclination and declination (ChRM calculated from PCA; U1537A = blue; U1537D = red) data. (A) Shipboard and u-channel inclination with horizontal lines indicating expected values for a geocentric axial dipole. (B) Shipboard and u-channel declinations rotated using the same value to reflect the polarity determined through inclination values. (C) U-channel declination data with linear trends removed to account for twisting of the cores during and/or after recovery. (D) Virtual geomagnetic pole latitudes using the rotated and detrended declination data. These values can be considered an estimate; however, are dependent on the treatment of declination data.

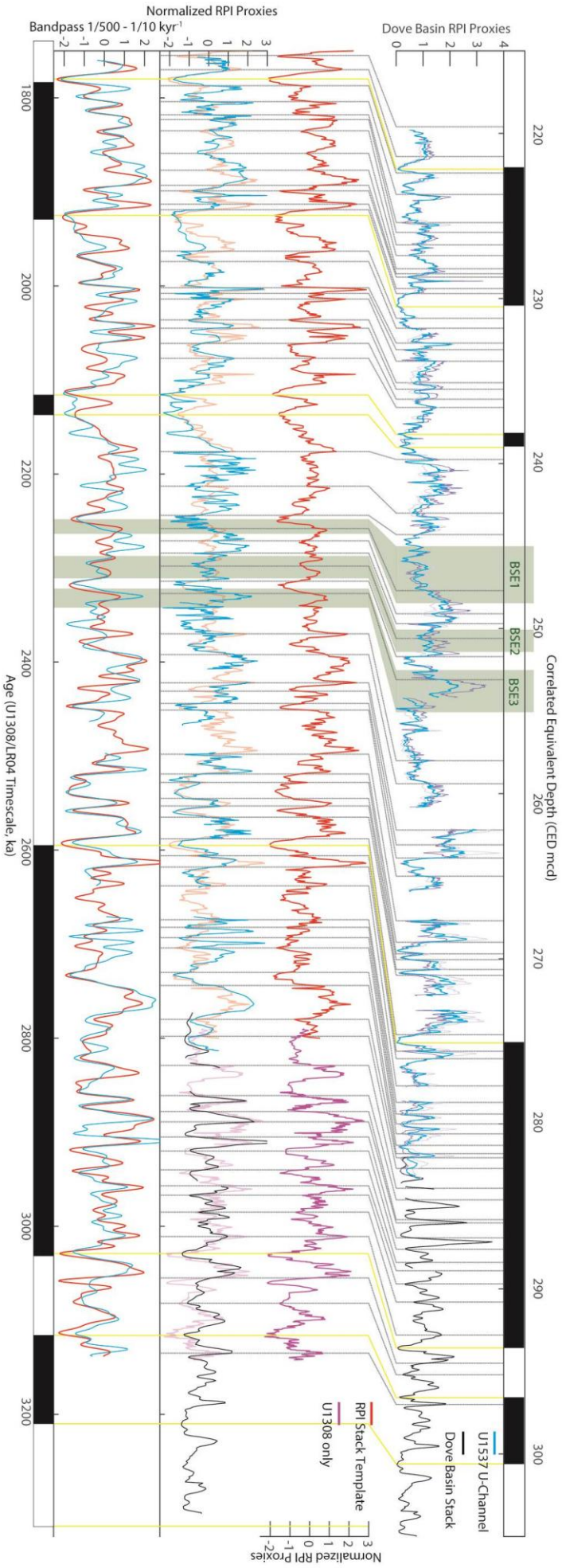
Normalized RPI Proxies
Bandpass 1/500 - 1/10 kyr-1
Dove Basin RPI Proxies
BSE1
BSE2
BSE3
Correlated Equivalent Depth (CED mcd)
Age (U1308/LR04 Timescale, ka)
U1537 U-Channel
Dove Basin Stack
RPI Stack Template
U1308 only
Normalized RPI Proxies

Figure S17. Adapted from main text **Figure 7** to show the details of the supervised correlation. Correlation of Dove Bain RPI proxies (blue, black) to the RPI template presented in **Figure 2**, extended by the benthic $\delta^{18}O$ age calibrated U1308 record to 3.142 Ma (purple). U-channel data represent the mean of u-channel ARM and k normalized data (light lines). RPI tie points are dashed grey lines and magnetic reversals are dashed yellow lines. Comparison of bandpass filtered (1/500 – 1/10 kyr-1) Dove Basin (blue) and North Atlantic (red) RPI proxies.

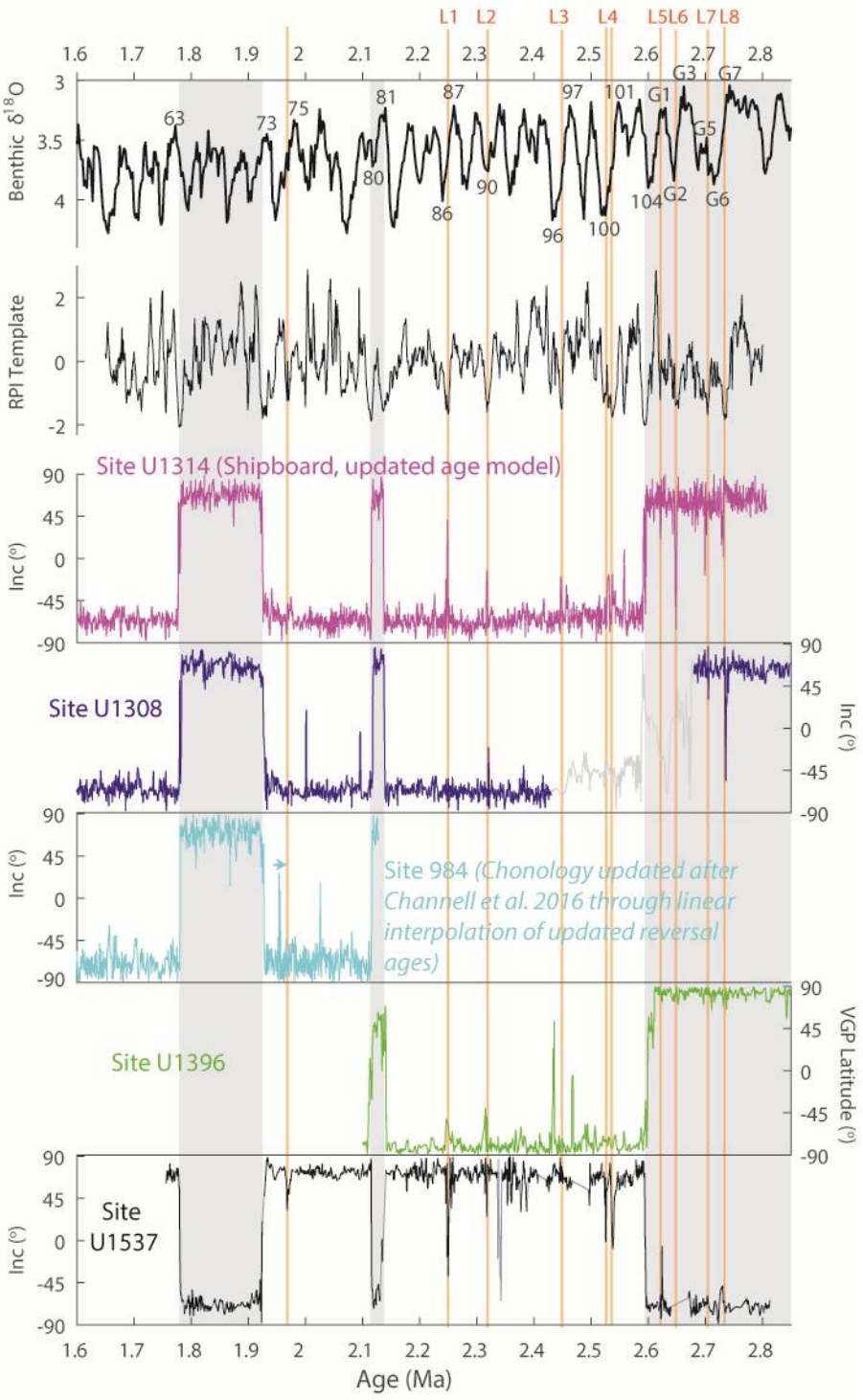

Figure S18. Comparison of directional data at Sites U1314 (Channell et al., 2006; Ohno et al., 2012), U1308 (Channell et al., 2016), 984 (Channell et al., 2002) with chronology modified after Channell et al. (2016), U1396 (Hatfield et al., 2021), and U1537. For reference, the RPI template developed for this study and LR04 benthic $\delta^{18}O$ with key MIS stage names (Lisiecki and Raymo, 2005) are plotted. Vertical

orange lines indicate the L-events of Ohno et al. (2012) and an additional excursion found at the top of the first interglacial interval below the base of the Olduvai Subchron.

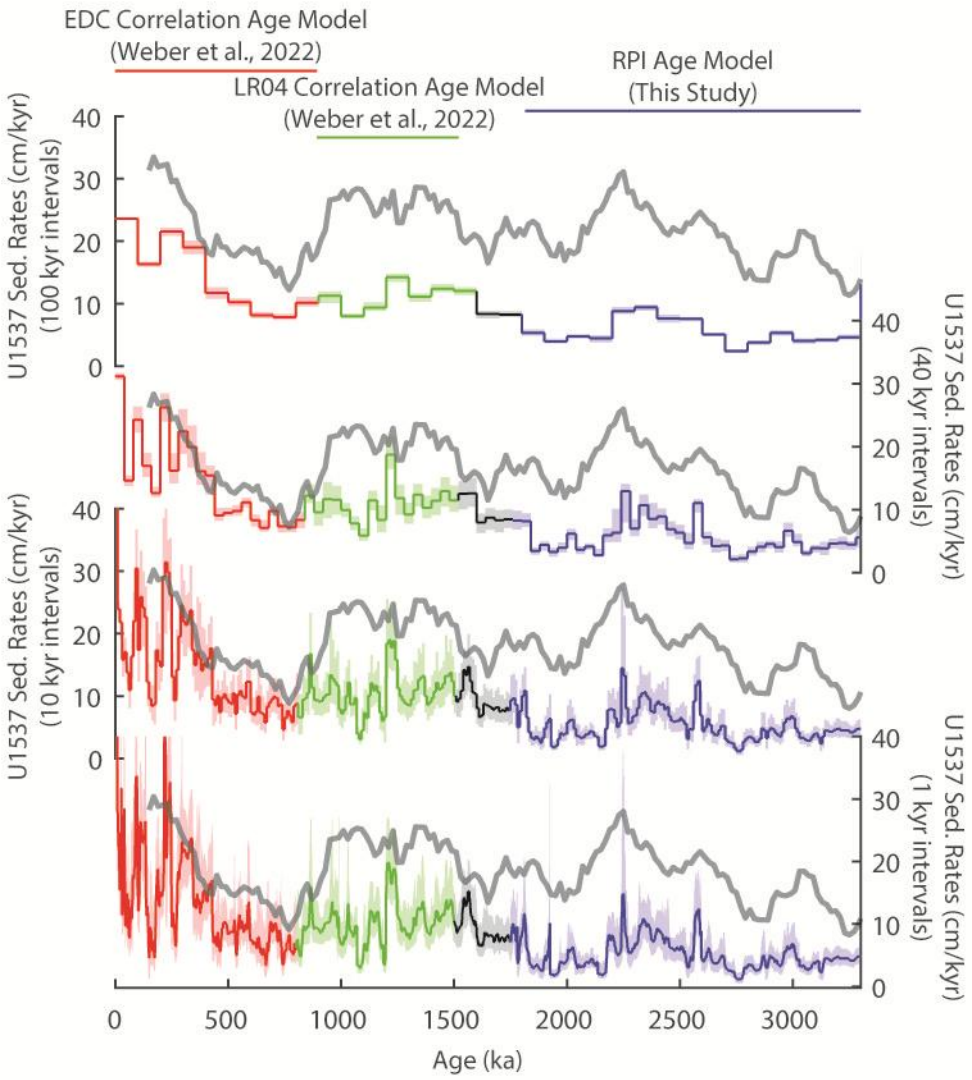

Figure S19. Sedimentation rates, after **Figure 8B**, calculating using four different interval widths. The normalized obliquity variance plus insolation variance, after **Figure 8H**, is plotted in each panel (thick gray line) to allow for more detailed comparison.

Table S1. Target Curves generated from Sites U1308, U1314, and U1396 for 1650-2800 ka with uncertainty.

Table S2. Revised age control points for Site U1314, following the approach described in the text.

Table S3. Summary of u-channel data.

Table S4. Dove Basin RPI proxy stack, using the natural remanent magnetization (NRM) after 15 mT peak AF demagnetization, normalized by magnetic susceptibility (k).

Table S5. Dove Basin Magnetic Susceptibility stack on depth.

Table S6. Age model constraints for Site U1537.

Table S7. Undatable age-depth model results.

Table S8. Physical Properties data on age.

Table S9. U1537 sedimentation rates calculated in 10 kyr bins.

References

Channell, J.E.T., Mazaud, A., Sullivan, P., Turner, S., Raymo, M.E., 2002. Geomagnetic excursions and paleointensities in the Matuyama Chron at Ocean Drilling Program Sites 983 and 984 (Iceland Basin). J.-Geophys.-Res. 107, EPM 1-1. https://doi.org/10.1029/2001JB000491

Channell, J.E.T., Kanamatsu, T., Sato, T., Stein, R., Alvarez Zarikian, C.A., Malone, M.J., and the Expedition 303/306 Scientists (Eds.), 2006. Proceedings of the IODP, 303/306, Proceedings of the IODP. Integrated Ocean Drilling Program.

Channell, J.E.T., Hodell, D.A., Curtis, J.H., 2016. Relative paleointensity (RPI) and oxygen isotope stratigraphy at IODP Site U1308: North Atlantic RPI stack for 1.2–2.2 Ma (NARPI-2200) and age of the Olduvai Subchron. Quaternary Science Reviews 131, 1–19. https://doi.org/10.1016/j.quascirev.2015.10.011

Hatfield, R.G., Stoner, J.S., Fraass, A.J., 2021. Relative Paleointensity Record of Integrated Ocean Drilling Program Site U1396 in the Caribbean Sea: Geomagnetic and Chronostratigraphic Observations in the Pliocene. Geochemistry, Geophysics, Geosystems 22, e2021GC009677. https://doi.org/10.1029/2021GC009677

Kok, Y.S., Tauxe, L., 1999. A relative geomagnetic paleointensity stack from Ontong-Java Plateau sediments for the Matuyama. Journal of Geophysical Research: Solid Earth 104, 25401–25413. https://doi.org/10.1029/1999JB900186

Lisiecki, L.E., Raymo, M.E., 2005. A Pliocene-Pleistocene stack of 57 globally distributed benthic δ 18 O records. Paleoceanography 20, PA1003. https://doi.org/10.1029/2004PA001071

Ohno, M., Hayashi, T., Komatsu, F., Murakami, F., Zhao, M., Guyodo, Y., Acton, G., Evans, H.F., Kanamatsu, T., 2012. A detailed paleomagnetic record between 2.1 and 2.75 Ma at IODP Site U1314 in the North Atlantic: Geomagnetic excursions and the Gauss-Matuyama transition. Geochemistry, Geophysics, Geosystems 13. https://doi.org/10.1029/2012GC004080

Reilly, B.T., Stoner, J.S., Wiest, J., 2017. SedCT: MATLAB™ tools for standardized and quantitative processing of sediment core computed tomography (CT) data collected using a medical CT scanner. Geochem. Geophys. Geosyst. 18, 3231–3240. https://doi.org/10.1002/2017GC006884

Reilly, B.T., Tauxe, L., Brachfeld, S., Raymo, M., Bailey, I., Hemming, S., Weber, M.E., Williams, T., Garcia, M., Guitard, M., Martos, Y.M., Pérez, L.F., Zheng, X., Armbrecht, L., Cardillo, F.G., Du, Z., Fauth, G., Glueder, A., Gutjahr, M., Hernández-Almeida, I., Hoem, F.S., Hwang, J.-H., Iizuka, M., Kato, Y., Kenlee, B., O'Connell, S., Peck, V., Ronge, T.A., Seki, O., Tripathi, S., Warnock, J., 2021. New Magnetostratigraphic Insights From Iceberg Alley on the Rhythms of Antarctic Climate During the Plio-Pleistocene. Paleoceanography and Paleoclimatology 36, e2020PA003994. https://doi.org/10.1029/2020PA003994

Reilly, B., Tauxe, L., Bailey, I., Brachfeld, S., Fenton-Samuels, K., Hatfield, R., Hemming, S., Jasper, C., O'Connell, S., Raymo, M., Stoner, J., Warnock, J., & Williams, T., 2026. Antarctic response to orbital forcing during the

intensification of extensive bipolar glaciation (1.75-3.30 Ma) from relative paleomagnetic intensity (RPI) stratigraphy of the Dove Basin, Scotia Sea [dataset]. Magnetics Information Consortium (MagIC). https://doi.org/10.7288/V4/MAGIC/20255

Reilly, B., Tauxe, L., Bailey, I., Brachfeld, S., Fenton-Samuels, K., Hatfield, R., Hemming, S., Jasper, C., O'Connell, S., Raymo, M., Stoner, J., Warnock, J., & Williams, T., 2025a. IODP Site U1537 1.7-3.3 Ma Rock Magnetic Data (FC, ZFC, LTC-RTSIRM, Hysteresis, DCD, FORCs) [Data set]. Zenodo. https://doi.org/10.5281/zenodo.14564186

Reilly, B., Tauxe, L., Bailey, I., Brachfeld, S., Fenton-Samuels, K., Hatfield, R., Hemming, S., Jasper, C., O'Connell, S., Raymo, M., Stoner, J., Warnock, J., & Williams, T., 2025b. Tables in support of "Antarctic response to orbital forcing during the intensification of extensive bipolar glaciation (1.75-3.30 Ma) from relative paleomagnetic intensity (RPI) stratigraphy of the Dove Basin, Scotia Sea" [Data set]. Zenodo. https://doi.org/10.5281/zenodo.14564253

Reilly, B.T., 2024. IODP Site U1537 U-Channel CT Scan DICOM Data, SedCT Output, and HU Values [Data set]. https://doi.org/10.5281/zenodo.14563999

Thomas, R.G., Guyodo, Y., Channell, J.E.T., 2003. U channel track for susceptibility measurements. Geochemistry, Geophysics, Geosystems 4. https://doi.org/10.1029/2002GC000454

Weber, M.E., Raymo, M.E., Peck, V.L., Williams, T., Armbrecht, L., Bailey, I., Brachfeld, S.A., Cardillo, F.G., Du, Z., Fauth, G., Garcia, M., Glueder, A., Guitard, M., Gutjahr, M., Hemming, S.R., Hernández-Almeida, I., Hoem, F.S., Hwang, J.-H., Iizuka, M., Kato, Y., Kenlee, B., Martos, Y.M., O'Connell, S., Perez, L., Reilly, B.T., Ronge, T.A., Seki, O., Tauxe, L., Tripathi, S., Warnock, J., Zheng, X., 2021e. Site U1537, in: Volume 382: Iceberg Alley and Subantarctic Ice and Ocean Dynamics, Proceedings of the International Ocean Discovery Program. International Ocean Discovery Program, College Station, TX.